



저작자표시-비영리-변경금지 2.0 대한민국

이용자는 아래의 조건을 따르는 경우에 한하여 자유롭게

- 이 저작물을 복제, 배포, 전송, 전시, 공연 및 방송할 수 있습니다.

다음과 같은 조건을 따라야 합니다:



저작자표시. 귀하는 원저작자를 표시하여야 합니다.



비영리. 귀하는 이 저작물을 영리 목적으로 이용할 수 없습니다.



변경금지. 귀하는 이 저작물을 개작, 변형 또는 가공할 수 없습니다.

- 귀하는, 이 저작물의 재이용이나 배포의 경우, 이 저작물에 적용된 이용허락조건을 명확하게 나타내어야 합니다.
- 저작권자로부터 별도의 허가를 받으면 이러한 조건들은 적용되지 않습니다.

저작권법에 따른 이용자의 권리는 위의 내용에 의하여 영향을 받지 않습니다.

이것은 [이용허락규약\(Legal Code\)](#)을 이해하기 쉽게 요약한 것입니다.

[Disclaimer](#)

이학박사 학위논문

Optimizing Electrical Properties of Graphene Film by Chemical Doping Methods

화학적 도핑을 이용한 그래핀의 전기적 특성
최적화 연구

2016 년 8 월

서울대학교 대학원

물리천문학부

김 영 수

Optimizing Electrical Properties of Graphene Film by Chemical Doping Methods

지도 교수 국 양

이 논문을 이학박사 학위논문으로 제출함
2016년 7월

서울대학교 대학원
물리천문학부
김 영 수

김영수의 이학박사 학위논문을 인준함
2016년 6월

위원장 박 제 근 (인)

부위원장 국 양 (인)

위원 홍 승 훈 (인)

위원 홍 병 희 (인)

위원 김 근 수 (인)

Optimizing Electrical Properties of Graphene Film by Chemical Doping Methods

by Youngsoo Kim

Supervised by Professor Young Kuk

Co-supervised by Professor Byung Hee Hong

A Dissertation Submitted to the Faculty of
Seoul National University
in Partial Fulfillment of the Requirements for
the Degree of Doctor of Philosophy

July 2016

Department of Physics and Astronomy,
Graduate School
Seoul National University

Abstract

Doping is an essential process to engineer the conductivity and work-function of graphene for higher performance optoelectronic devices, which includes substitutional atomic doping by reactive gases, electrical doping by gate bias, and chemical doping by acids or reducing/oxidizing agents. Among these, the chemical doping has been widely used due to its simple process and high doping strength.

For studying doping effect of graphene, we used APPE (aminophenyl propargyl ether) as a novel n-type dopant for graphene. From the result of Raman spectroscopy and electrical measurement, we suppose that the electron donating property of amine group ($-NH_2$) is the origin of such intense n-doping effect. Also we studied a simple method to tune the electrical properties of CVD graphene through n-doping by vaporized molecules at 70 °C, where the dopants in vapor phase are mildly adsorbed on graphene surface. To investigate the dependence on functional groups and molecular weights, we selected a series of ethylene amines as a model system, including ethylene diamine (EDA), diethylene triamine (DETA), and triethylene tetramine (TETA) with increasing number of amine groups showing different vapor pressures. We confirmed that the vapor-phase doping provides not only very high carrier concentration but also good long-term stability in air, which is particularly important for practical applications. Moreover, we studied strong modulation method for enhancement of the electrical conductivity of graphene by dual-side

molecular n-doping with diethylenetriamines (DETAs) on top and amine-functionalized self-assembled monolayers (SAMs) at bottom.

We constructed a self-assembled monolayers (SAMs) for modification of SiO₂ substrate resulting in enhancement of mobility and conductivity of graphene. Graphene p-n junction was constructed by e-beam lithographic technique with NH₂-SAMs and confirmed n-type and p-type simultaneously. Our approach would be a promising for modifying graphene surface at a desired region of electronic devices due to easy to make p-n junction. SAMs with different functional group show temperature dependence in electrical properties. For actual application of graphene, we studied the mass-productive graphene films synthesized by hydrogen-free rapid thermal chemical vapor deposition (RT-CVD), roll-to-roll etching, and transfer methods, which enabled faster and larger production of homogeneous graphene films by installing the RT-CVD films to resistive multi-touch devices.

Lastly, we studied a giant orbital diamagnetism in graphene films grown by chemical vapor deposition (CVD), where the diamagnetic susceptibility in perpendicular direction is measured to be ~100 times greater than the strongest diamagnetic materials such as bismuth.

Keywords : Graphene , Chemical doping, Graphene field effect transistor, Chemical vapor deposition, Graphene application, Graphene magnetism

Student Number : 2012-30101

Table of Contents

Abstract	i
List of Figures	vi
List of Tables	xv
Chapter 1. Introduction	1
1.1 Graphene Band Structure	
1.2 Chemical Doping of Graphene	
1.3 Transport Phenomena in Doped Graphene.	
1.4 Graphene Applications	
Chapter 2. Experimental	26
2.1 CVD Graphene Sample Preparation	
2.2 Chemical Doping Methods	
2.3 Optical Measurement: Raman Spectroscopy	
2.4 Graphene Field Effect Transistor	
2.4.1 Fabrication Process	
2.4.2 Electrical Measurement Technique	
Chapter 3. Efficient N-Doping of Graphene Films by APPE (Aminophenyl Propargyl Ether)	43
3.1 Introduction	

- 3.2 Experimental
- 3.3 Result and Discussion
- 3.4 Summary

Chapter 4. Vapor-Phase Molecular Doping of Graphene for High-Performance Transparent Electrodes55

- 4.1 Introduction
- 4.2 Experimental
- 4.3 Result and Discussion
- 4.4 Summary

Chapter 5. A Highly Conducting Graphene Film with Dual-Side Molecular n-Doping.....75

- 5.1 Introduction
- 5.2 Experimental
- 5.3 Result and Discussion
- 5.4 Summary

Chapter 6. Graphene Field Effect Transistors Modified by Self-Assembled Monolayers.....92

- 6.1 Introduction
- 6.2 Experimental

6.3 Result and Discussion

6.4 Summary

**Chapter 7. Fast Synthesis of High-Performance Graphene Films by
Hydrogen-Free Rapid Thermal Chemical Vapor Deposition·····108**

7.1 Introduction

7.2 Experimental

7.3 Result and Discussion

7.4 Summary

**Chapter 8. Giant Orbital Diamagnetism in Graphene at Room
Temperature ·····129**

8.1 Introduction

8.2 Experimental

8.3 Result and Discussion

8.4 Summary

Bibliography·····154

**Appendix A LabVIEW Programming for Electrical
Measurement·····169**

Abstract in Korean (국문초록)·····175

List of Figures

Chapter 1.

Figure 1.1. Honeycomb lattice and its Brillouin zone.

Figure 1.2. Electronic dispersion in the honeycomb lattice for finite values of $t = 2.8$ eV.

Figure 1.3. I_{ds} vs V_{ds} characteristics at various V_g for (a) the pristine graphene and (b) the N-doped graphene FET device, respectively. ^[32]

Figure 1.4. Transmittance and sheet resistance data for papers appearing in the literature.

Figure 1.5. Transfer curves (I_d vs. V_g) for SLG field-effect transistors before and after TPA doping (drain voltage, $V_D = 0.5$ V). ^[13]

Figure 1.6. The conductivity (σ) versus gate voltage (V_g) curves for the pristine sample and three different concentrations of potassium doped graphene taken at 20 K in ultrahigh vacuum (UHV).

Figure 1.7. Measurement scheme of graphene field effect transistor with 2-terminal method including gate.

Figure 1.8. The scheme of 2D electron gas at the Fermi surface.

Figure 1.9. The scheme of phonon effects in graphene transport.

Figure 1.10. The relation of random potential to I- V_g curves in intrinsic and extrinsic graphene.

Figure 1.11. The conductivity of n-doped and undoped graphene as a function of gate voltage in a logarithmic scale to estimate the random potential density of graphene.

Figure 1.12. A resistance vs gate voltage of pristine graphene and red line is fitted curve.

Figure 1.13. Sheet resistance vs doping concentration plot with considering remote interface phonon and longitudinal phonon effect together.

Figure 1.14. A photograph of 30-inch CVD graphene transferred on PET film. ^[22]

Figure 1.15. a) Temperature history, and b) temperature response of the SWCNT film surface on a PET substrate.

Figure 1.16. CVD graphene heater. ^[31]

Figure 1.17. Graphene-based multi-touch screen showing excellent flexibility (left) and possible applications in bendable or foldable mobile devices (right). ^[30]

Chapter 2.

Figure 2.1. 4 inch CVD growth system.

Figure 2.2. Schematic illustration of the synthesis and transfer processes of large-area CVD graphene films.

Figure 2.3. The optical image of CVD grown graphene.

Figure 2.4. The doping methods (a) dipping and spin-coating method, (b) vapor-phase doping method and (c) construction of self-assembled monolayers.

Figure 2.5. The renormalization of the phonon energy is allowed when the change in the Fermi energy E_F is smaller than half of the phonon energy $\hbar\omega_G/2$ (left figure) and it is suppressed for $E_F > \hbar\omega_G/2$ (right figure).

Figure 2.6. Linewidth and frequency of the Raman G band as a function of the electron concentration which is proportional to the square of the Fermi level energy. ^[51]

Figure 2.7. G band FWHM linewidth (upper figure) and energy (lower figure) of monolayer graphene, as a function of the Fermi level energy. ^[54]

Figure 2.8. Current vs gate voltage curve of pristine graphene field effect transistor (left) and electric induced doping scheme (right).

Figure 2.9. Optical image and picture of fabricated graphene devices.

Figure 2.10. Electron beam and thermal evaporator.

Figure 2.11. The fabrication process of graphene field effect transistor.

Figure 2.12. Reactive ion etching (RIE) system.

Figure 2.13. Wire-bonder (West bond Inc.).

Figure 2.14. Probe station with ambient condition.

Figure 2.15. Agilent B2912A source-meter.

Figure 2.16. Cryostats for transport measurement (a) Liquid Nitrogen cooling type (temperature down to 77 K) (b) Helium gas circulation type with superconducting magnet (temperature down to 4 K, magnetic field up to 9 Tesla).

Chapter 3.

Figure 3.1. Doping procedure of graphene with APPE.

Figure 3.2. Raman spectra of pristine and APPE doped graphene.

Figure 3.3. Graphenes device of APPE and NPPE doped graphene.

Figure 3.4. Sheet resistances (a) and charge carrier mobilities (b) of APPE doped graphene FETs.

Chapter 4.

Figure 4.1. Schematic of doping process and dopants.

Figure 4.2. Characterization of Raman spectra of pristine, EDA, DETA, and TETA doped graphene.

Figure 4.3. Electrical characteristic of the undoped and n-doped graphene FET devices.

Figure 4.4. Dirac voltage shift as a function of air exposure time for each molecular doped graphene devices.

Figure 4.5. Changes in the transmittance at 550nm wavelength (a), sheet resistance (b), and Dirac voltage (c) of EDA-, DETA-, and TETA-doped graphene with increasing annealing time at 70 °C.

Figure 4.6. Schematic illustration of the synthesis and transfer processes of large-area CVD graphene films.

Figure 4.7. (a) Dirac voltage shift before and after doping with EDA (green), DETA (red) and TETA (blue) molecules. (b) Sheet resistance of pristine, EDA, DETA, and TETA doped graphene corresponding to (a).

Figure 4.8. Optical images of graphene with various doping conditions.

Figure 4.9. Dirac voltage shift of graphene FET with various doping conditions.

Figure 4.10. Atomic force microscope (AFM) images of exfoliated graphene on a SiO₂ substrate before and after doping.

Figure 4.11. (a) Representative current vs. gate voltage curves for a pristine graphene device with respect to exposure time in air. (b) Dirac

voltages of the 10 pristine graphene devices as a function of exposure time.

Figure 4.12. (a) Representative transmittance curve of each molecule-doped graphene depending on wavelength. (b) Optimized transmittance of each molecule-doped graphene after 20 minutes heating (at 550 nm wavelength). (c) Representative transmittance curves of as-prepared and n-doped graphene as a function of wavelength.

Figure 4.13. Representative current vs. gate voltage curves for EDA (a), DETA (b), and TETA (c) doped graphene devices with respect to heating time.

Chapter 5.

Figure 5.1. Schematic views of three different types of n-doped graphene.

Figure 5.2. (a) The representative Raman spectra of graphene with different dopants (pristine, NH₂-SAMs, DETA and DETA/NH₂-SAMs). (b) Raman shift vs. I(2D)/I(G) ratio plot of pristine, NH₂-SAMs modified, DETA doped, and dual-side modified (DETA/NH₂-SAMs) graphene.

Figure 5.3. Schematic illustration of doping process and graphene FET characteristic of pristine and doped graphene.

Figure 5.4. Electrical properties of pristine graphene and doped by NH₂-SAMs, DETA and DETA/NH₂-SAMs.

Figure 5.5. The temperature profiles of pristine, bottom doped and dual-side doped graphene heaters.

Figure 5.6. (a) Representative UV-Vis spectra of top, bottom and dual-side doped graphene film (b) Transmittance of pristine, top-side doped, bottom-side doped and dual-side doped graphene.

Figure 5.7. (a) The Dirac voltage shift of dual-side doped graphene as a function of exposure time in the ambient condition at room temperature (b) Light stability of dual-side doped graphene with respect to exposure time (100 W light bulb was used as a light source). (c) Thermal stability of dual-side doped graphene with heating time under 70 °C (blue) and 100 °C (red).

Figure 5.8. FET characteristics of DETA-doped graphene with respect to doping time and temperature.

Figure 5.9. Statistical analysis of temperature distribution in the graphene-based heaters.

Chapter 6.

Figure 6.1. Schematic views of mono layer graphene FET on amine-SAMs.

Figure 6.2. Electrical properties of chemical modified graphene devices.

Figure 6.3. a) Dirac point and b) electron/hole mobility of amine modified graphene as a function of applied temperature c) Comparison of the impurity carrier concentration vs. conductivity for n-doped samples at 5 K (black line) and 300 K (red line). The arrows indicate that charged impurity concentration. d) Temperature dependence of charged impurity and its saturation Fermi energy.

Figure. 6.4. a) The ρ - V_g curves (inset shows Dirac voltage as a function of temperature). b) Temperature dependence with mobility of pristine graphene FET on SiO₂ substrate. c) Temperature dependence of resistivity of pristine graphene FET on SiO₂ as a function of gate voltage. d) charged impurity of graphene on SiO₂ as a function of temperature.

Figure. 6.5. a) The ρ - V_g curves (inset shows Dirac voltage as a function of temperature). b) Temperature dependence with mobility of pristine graphene FET on ODTS-SAMs substrate. c) Temperature dependence of resistivity of pristine graphene FET on ODTS-SAMs as a function of gate voltage. d) charged impurity of graphene on ODTS-SAMs as a function of temperature.

Figure. 6.6. A schematic view of fabrication process of graphene p-n junction device.

Figure. 6.7. Electrical transport measurements of graphene p-n junction devices.

Figure. 6.8. Raman spectra of the graphene p-n junction device.

Chapter 7.

Figure 7.1: Schematic of RT-CVD synthesis and graphene Growth condition.

Figure 7.2: Spectroscopic analyses of RT-CVD graphene films.

Figure 7.3: Electrical and optical analyses of RT-CVD graphene films.

Figure 7.4: Grain boundary analyses by TEM and OM.

Figure 7.5: Photographs of the fabrication processes of graphene-based resistive touch-screen devices.

Figure 7.6: Photographs of production-compatible RT-CVD, roll-to-roll etching, and lamination systems.

Figure 7.7: Grain size analyses of RT-CVD graphene films by H₂O₂-assisted oxidation and HR-TEM methods.

Figure 7.8: Schematic illustration of RT-CVD synthesis and subsequent production processes of graphene films and graphene-based capacitive touch screens.

Figure 7.9. Schematic illustration for the fabrication processes of graphene FETs.

Figure 7.10. Optical image of partially grown graphene and comparing WF Raman and micro Raman mapping images.

Figure 7.11. Sheet resistance of RT-CVD graphene.

Figure 7.12. Electrical properties of graphene field effect transistors.

Chapter 8.

Figure 8.1. Schematic illustration of the experimental setup for the levitating CVD graphene fiber at room temperature.

Figure 8.2. AFM images and line scans of an as-transfer PMMA/graphene.

Figure 8.3. Preparation of PMMA/graphene and PMMA samples for MPMS.

Figure 8.4. Schematic illustrations of a diamagnetic response in graphene with applied magnetic field.

Figure 8.5. Optical, electrical and magnetic properties of CVD graphene.

Figure 8.6. Magnetic susceptibility of CVD graphene.

Figure 8.7. Layer Dependence of Magnetic susceptibility of CVD graphene.

Figure 8.8. Raman analyses of graphene.

Figure 8.9. TEM analyses of the high quality CVD graphene.

Figure 8.10. XPS and Angle-Resolved XPS spectra of CVD graphene.

Figure 8.11. Raw magnetization of **a**, a bare PET and 1 layer of graphene on the bare PET, **b**, 5 layers of PMMA/graphene and PMMA on PET, **c**, 10 layers of PMMA/graphene and PMMA on PET. **d**, 1 layer of PMMA/graphene and PMMA, **e**, 5 layers of PMMA/graphene and PMMA, **f**, 10 layers of PMMA/graphene and PMMA samples suspended on sample holder.

Figure 8.12. Raw magnetization of 10 layers of PMMA/graphene and PMMA on PET.

List of Tables

Table 1.1. Graphene doping methods.

Table 1.2. Graphene synthesis methods.

Table 3.1. Comparison between Dirac voltage values after different n-doping treatments.

Table 7.1. Comparisons of T-CVD grown graphene and RT-CVD grown graphene sample.

Table 8.1. Room temperature magnetic susceptibility values for graphene, graphite, and other magnetic materials.

Table 8.2. Comparison of the mass of samples for MPMS measurements.

Chapter 1 Introduction

1.1 Graphene Band Structure

Graphene is single layer sheet of graphite, which electronic band structure was already studied by Wallace at 1947.^[2] Until 2004, graphene is dream material to experimental scientist because of its intrinsic properties predicted by many theoretical scientist. Moreover, the order parameter expectation value vanished in dimensions of two or less, resulting in absence of phase transition in 2D material by N. D. Mermin.^[190] Eventually, A.K. Geim and K.S. Novoselov obtained one layer graphene by very simple method (Scotch tape method)^[1] resulting in starting of tremendous research in graphene. After 2004, many researchers have reported outstanding properties of graphene, such as extremely high mobility, mechanical properties, heat conductivity, easily tunable energy band, and so on.

Graphene is consist of six carbon atoms with hexagonal structure (Figure 1.1), which constructing of sp^2 orbitals. The structure of graphene can be seen with a basis of two carbon atoms per unit cell, resulting in two equivalent atom sublattices: A and B. The lattice vectors can be written as follow

$$a_1 = \frac{a}{2}(3, \sqrt{3}), \quad a_2 = \frac{a}{2}(3, -\sqrt{3}) \quad (1)$$

where $a = 1.42 \text{ \AA}$ with the nearest neighboring atomic distance.

The reciprocal lattice vectors are given by

$$b_1 = \frac{2\pi}{3a}(1, \sqrt{3}), \quad b_2 = \frac{2\pi}{3a}(1, -\sqrt{3}) \quad (2)$$

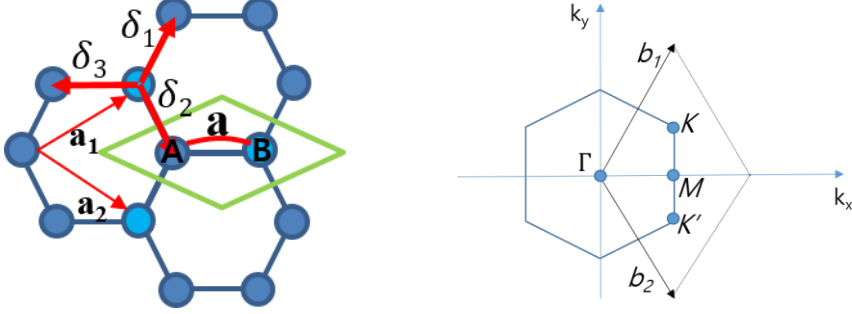


Figure. 1.1. Honeycomb lattice and its Brillouin zone. Left: lattice structure of graphene, made out of two interpenetrating triangular lattices (\mathbf{a}_1 and \mathbf{a}_2 are the lattice unitvectors, and $\delta_i, i=1,2,3$ are the nearest-neighbor vectors). Right: corresponding Brillouin zone. The Dirac cones are located at the K and K' points.

The structure of graphene can be expressed by k -space with the two points K and K' at the corner of the Brillouin zone (BZ), which is named Dirac points. The vectors of Dirac points in k -space are given by

$$K = \left(\frac{2\pi}{3a}, \frac{2\pi}{3\sqrt{3}a} \right), \quad K' = \left(\frac{2\pi}{3a}, -\frac{2\pi}{3\sqrt{3}a} \right) \quad (3)$$

If the system has translation invariance (which means that the system has periodicity), the model can be expressed using Bloch's theorem, which is a special case of a linear combination of atomic orbitals (LCAO) that depend on the position vector \mathbf{r} and wave vector k given as below

$$|\psi_A\rangle = \frac{1}{\sqrt{N}} \sum_{\vec{r}} \exp(i\vec{k}\vec{r}) |\vec{r}\rangle, \quad |\psi_B\rangle = \frac{1}{\sqrt{N}} \sum_{\vec{r}} \exp(i\vec{k}\vec{r}) |\vec{r} + \vec{\delta}_1\rangle$$

(4)

where the sum is over N different unit cells and δ_1 is one of the nearest-neighbor vectors. The simple tight-binding Hamiltonian for electrons in graphene considering hopping term “ t ” at the nearest neighbor atoms can be written as

$$H = -t \sum_r (|\vec{r}\rangle \langle \vec{r} + \vec{\delta}_1| + |\vec{r}\rangle \langle \vec{r} + \vec{\delta}_2| + |\vec{r}\rangle \langle \vec{r} + \vec{\delta}_3| + H. c.)$$

(5)

where δ_i ($i = 1, 2, 3$) are the nearest-neighbor vectors between carbon atoms with $\delta_1 = \frac{a}{2}(1, \sqrt{3})$, $\delta_2 = \frac{a}{2}(1, -\sqrt{3})$, $\delta_3 = a(-1, 0)$ and t (~ 2.8 eV) is the nearest-neighbor hopping energy (hopping between different sublattices).

The Hamiltonian with wavefunction for a and b carbon atoms can be rewritten as

$$\langle \psi | H | \psi \rangle = \begin{pmatrix} \langle \psi_A | H | \psi_A \rangle & \langle \psi_A | H | \psi_B \rangle \\ \langle \psi_B | H | \psi_A \rangle & \langle \psi_B | H | \psi_B \rangle \end{pmatrix} = \begin{pmatrix} H_{AA} & H_{AB} \\ H_{BA} & H_{BB} \end{pmatrix} \quad (6)$$

where the Dirac notation $\langle \psi_i | H | \psi_j \rangle = \int d^2r \psi_j^*(r) H \psi_i(r)$. The diagonal term $\langle \psi_A | H | \psi_A \rangle$ and $\langle \psi_B | H | \psi_B \rangle$ are the energies of the wavefunction by Schrodinger equation ($H\psi = E\psi$). Now, we apply an

approximation of tight-binding model near the Dirac cone ($k \sim 0$) with using Taylor's expansion (a_0 : carbon-carbon distance),

$$\begin{aligned}
H_{AB} &= -t[1 + \exp(i\vec{k}\vec{\delta}_2) + \exp(i\vec{k}\vec{\delta}_3)] \\
&\sim -t \left[1 + \exp\left(i\frac{2\pi}{3}\right)(1 + i\vec{k}\vec{\delta}_2) + \exp\left(-i\frac{2\pi}{3}\right)(1 + i\vec{k}\vec{\delta}_2) \right] \\
&= -t \left[1 + 2\cos\left(\frac{2\pi}{3}\right) + \exp\left(i\frac{2\pi}{3}\right) \left[-ia\left(\frac{k_x}{2} + \frac{\sqrt{3}k_y}{2}\right) \right] \right. \\
&\quad \left. + \exp\left(i\frac{2\pi}{3}\right) \left[-ia\left(-\frac{k_x}{2} + \frac{\sqrt{3}k_y}{2}\right) \right] \right] \\
&= -t \left[\frac{ik_x a}{2} \left[\exp\left(i\frac{2\pi}{3}\right) - \exp\left(-i\frac{2\pi}{3}\right) \right] \right. \\
&\quad \left. - \frac{i\sqrt{3}k_y a}{2} \left[\exp\left(i\frac{2\pi}{3}\right) + \exp\left(-i\frac{2\pi}{3}\right) \right] \right] \\
&= -t \left[\frac{ik_x a}{2} (2i\sin\left(\frac{2\pi}{3}\right)) - \frac{i\sqrt{3}k_y a}{2} (2\cos\left(\frac{2\pi}{3}\right)) \right] \\
&= -t \left[\frac{\sqrt{3}a}{2} [-k_x + ik_y] \right] = -\frac{3ta_0}{2} [-k_x + ik_y] \tag{7}
\end{aligned}$$

Similarly for H_{BA}

$$H_{BA} = -\frac{3ta_0}{2} [-k_x - ik_y] \tag{8}$$

and we assumed that onsite energy is negligible ($H_{AA}, H_{BB} \sim 0$).

Therefore, we can find the Dirac-like dispersion by plugging each component of matrices into equation (6),

$$\langle \psi | H | \psi \rangle = -\frac{3ta_0}{2} \begin{pmatrix} 0 & k_x - ik_y \\ k_x + ik_y & 0 \end{pmatrix} = -v_F \sigma \cdot p \quad (9)$$

where σ is pseudospin vectors and p is momentum vector.

We can expect the electrons in graphene behave relativistically from this Dirac equation of graphene and the energy bands derived from this Hamiltonian have the form and was first obtained by Wallace (1947).^[2]

$$E_{\pm}(k) \approx \pm v_F |q| \quad (10)$$

where v_F is the Fermi velocity given by $v_F = 3ta_0/2$, with a value $v_F \sim 1 \times 10^6$ m/s. The plus sign applies to the upper (π^*) and the minus sign the lower (π) band. The electronic band structure of graphene with first-nearest neighbor was shown in figure 1.2.

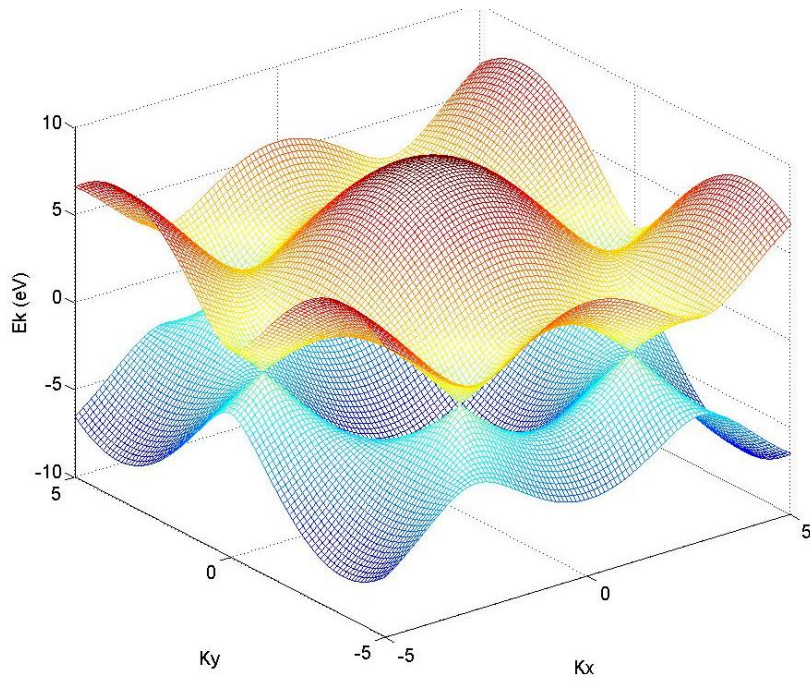


Figure 1.2. Electronic dispersion in the honeycomb lattice for finite values of $t = 2.8$ eV.

1.2 Chemical Doping of Graphene

The absence of band gap of graphene is main obstacle for using electronic transistor. Recently, many scientists have studied to widen the band gap in three ways: Large-area graphene in one dimension to form graphene nanoribbons, by biasing bilayer graphene and by applying strain to graphene, ^[4-6] but still lacking comparing to silicon based transistors. Herein, graphene can be used as transparent electrodes from changing the way of using as transistor. For using transparent electrodes, resistance of graphene is another problem to replace indium tin oxide (ITO). One of the solution is doping to tune the Fermi energy level of graphene. The mechanism of chemical doping in graphene would resemble that of carbon nanotubes, however the latter is still controversial. ^[7-9]

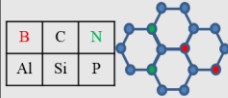
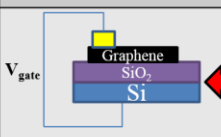
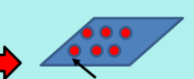
Carrier injection		Controlling the Fermi level	
Ad-atom doping	Chemisorption	Gate dielectric	Physisorption
Using B or N atoms to inject electrons or holes. 	 Break sp^2 bonding of graphene and make chemical bonding.	 Other studies: Gating (doping effect) is done by back & top electrodes.	 In this thesis: Fermi level shift from chemical doping

Table 1.1. Graphene doping methods.

The doping of graphene can be classified according to its doping method as follow (see also in Table 1.1).

1. Carrier injection
2. Controlling the Fermi level

The carrier injected doping can be divided into i) ad-atom doping, can be obtained by changing carbon atom to other species such as boron or nitrogen,^[17-19] and ii) by breaking the sp² bonding of graphene and make chemical bonding. Otherwise, doping can be obtained by controlling the Fermi level of graphene, which can be divided by i) using a gate dielectric with changing a gate voltage,^[1] and ii) physisorption of chemical dopants on top of the graphene surface.^[10-16] Comparing two doping method for using transparent electrode, carrier injection type doping method has an advantage in doping stability, but modified structure of graphene losses its intrinsic properties resulting in high resistance.^[19] While physisorption method can achieve low resistance due to its tunability, but it is insufficient in doping stability (Figure 1.3.).

Graphene, one layer graphite film, can be easily tuned by gases, chemicals or metals due to large exposed surface. The type of doping is generally introduced in p-type and n-type doping, decided by withdrawing or donating electrons. Figure 1.4 shows various carbon based materials to industrial limitation depending on resistance and transparency.^[29]

The conventional way to modify electronic properties of a materials is the electric field effect by using the gate dielectric such as silicon oxide, hafnium oxide or silicon nitride to obtain low sheet resistance of graphene. However, the gate voltage induced doping has a limitation in the size of doped graphene and its complexity in device fabrication process. In this thesis, we studied physisorption method

with various doping methods and doping molecules to obtain the lowest sheet resistance of graphene.

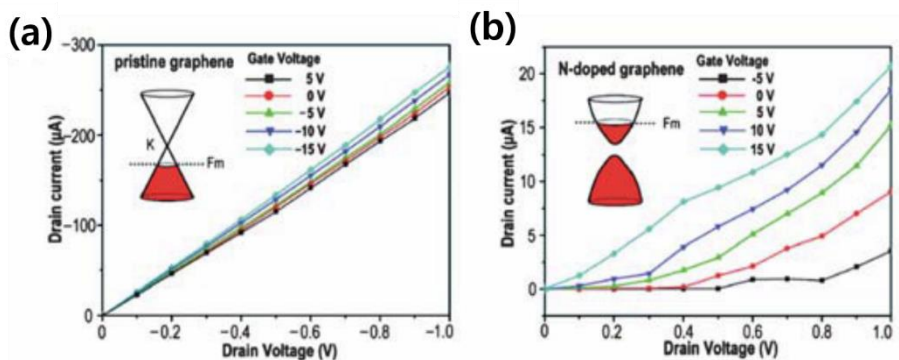


Figure 1.3. I_{ds} vs V_{ds} characteristics at various V_g for (a) the pristine graphene and (b) the N-doped graphene FET device, respectively. [Adapted from Ref.32]

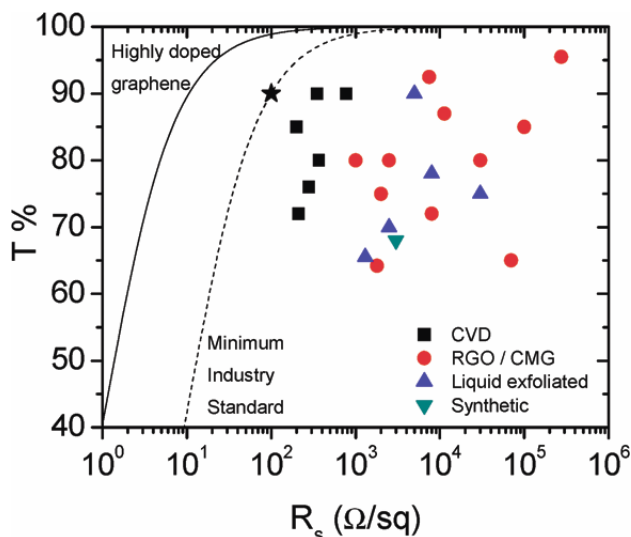


Figure 1.4. Transmittance and sheet resistance data for papers appearing in the literature. In all cases the data in the figure correspond to the best data reported. The star represents the minimum industry standard for transparent electrodes ($R_s=100\Omega/\text{sq}$, $T=90\%$) [Adapted from Ref. 29]

1.2.1 Physisorption doping: p-type

Recently, p-type doping has been studied by many groups^[9,11-13] and widely studied in application.^[25,28,31] The reported p-type dopants widely dispersed in gas (water vapor, oxygen gas, NO₂ gas), acid or polymers (nitric acid, sulfuric acid, F4-TCNQ, aromatic molecules and so on), and metals (Au, Al, and Pt).^[9, 11-13]

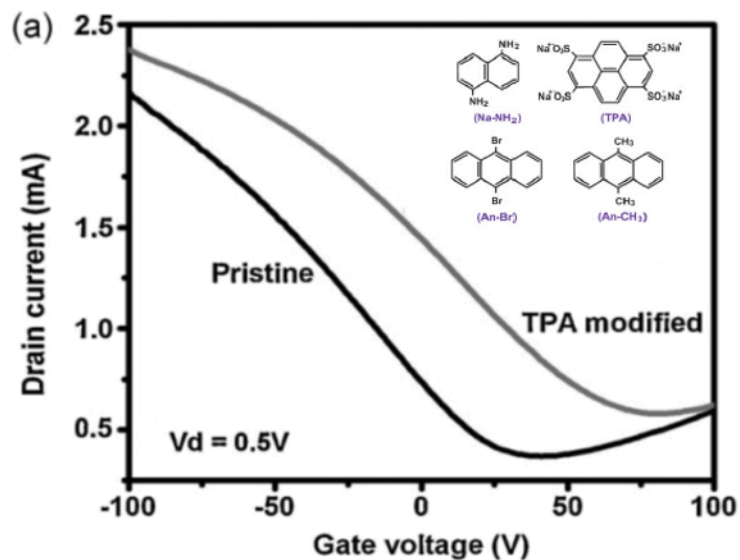


Figure 1.5. Transfer curves (I_d vs. V_g) for SLG field-effect transistors before and after TPA doping (drain voltage, $V_D=0.5V$).^[13]

1.2.2 Physisorption doping: n-type

The n-type doping is more difficult to maintain due to water vapor and oxygen in ambient condition p-type doping gases. The reported n-type dopants are ethanol and ammonia, hydrazine, poly(ethyleneimine) (PEI). Contrary to p-type doping, n-type doping is challenging due to lacking of its doping strength and stability. The representative n-type doping showed in figure 1.6 by using potassium as a function of doping time. ^[111]

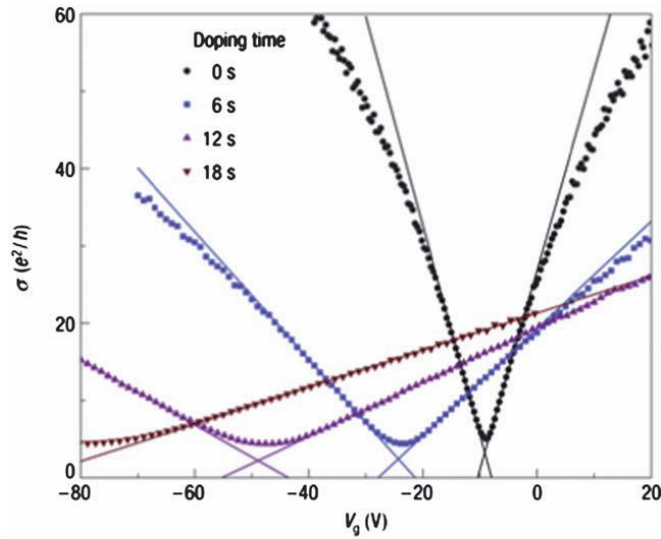


Figure 1.6. The conductivity (σ) versus gate voltage (V_g) curves for the pristine sample and three different concentrations of potassium doped graphene taken at 20 K in ultrahigh vacuum (UHV). ^[111]

1.3 Transport Phenomena in Doped Graphene

Field Effect Doping of Graphene

The electronic properties of graphene can be tuned by applying an external voltage (Gate voltage), one can vary the carrier density in the graphene resulting in its sheet resistance. The field effect transistor of graphene can be constructed with source, drain and gate electrodes as described in Figure 1.7.

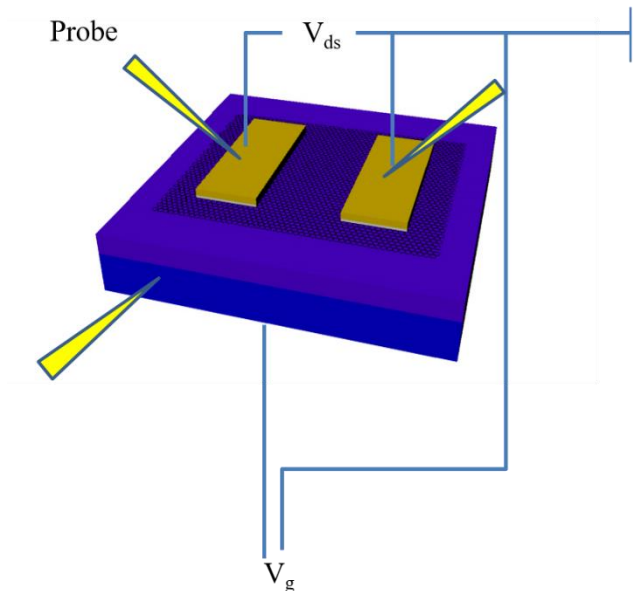


Figure 1.7. Measurement scheme of graphene field effect transistor with 2-terminal method including gate.

The carrier concentration by applying a gate voltage can be estimated by concerning its insulating thickness and permittivity as following equation

$$n = \alpha V_g, \quad \alpha = \frac{\epsilon_{SiO_2} \cdot \epsilon_0}{t_{SiO_2} \cdot e} \quad (11)$$

where $\alpha = 7.2 \cdot 10^{10} \text{ cm}^{-2} \text{ V}^{-1}$, t_{SiO_2} : SiO₂ thickness, ϵ_0 is the permittivity of free space ($\sim 8.854 \cdot 10^{-12} \text{ F/m}$), ϵ_{SiO_2} is the relative permittivity of SiO₂ (~ 3.9) and e is the electron charge ($\sim 1.6 \cdot 10^{-19} \text{ C}$).

The Dirac voltage V_{Dirac} is a gate voltage at minimum conductivity of source-drain current. The Dirac voltage of intrinsic graphene is $V_{Dirac} = 0 \text{ V}$, but synthesized graphene is normally doped due to humid, impurity and surrounding gases. Thus, the Dirac voltage V_{Dirac} is useful value to estimate the doping level of synthesized or doped graphene, which can be obtained from the below relation.

$$n = \alpha(V_g - V_{Dirac}) \quad (12)$$

To obtain the Fermi energy level for graphene, the electron gas in two dimension system need to consider. Each grid point can be occupied by two electrons with spin (g_s) and valley degeneracy (g_v) and all filled states correspond to grid-points which are inside the Fermi circle (Figure 1.8). The total number N of electrons in the Fermi circle can be expressed as below

$$N = g_s g_v \times \frac{A}{(2\pi)^2} \times \pi k_F^2 \quad (13)$$

where $g_s, g_v = 2$ and summing up the equation (13) and divide N by area

(A) to obtain electron density, we get

$$n = \frac{k_F^2}{\pi}, \quad k_F = (n\pi)^{\frac{1}{2}} \quad (14)$$

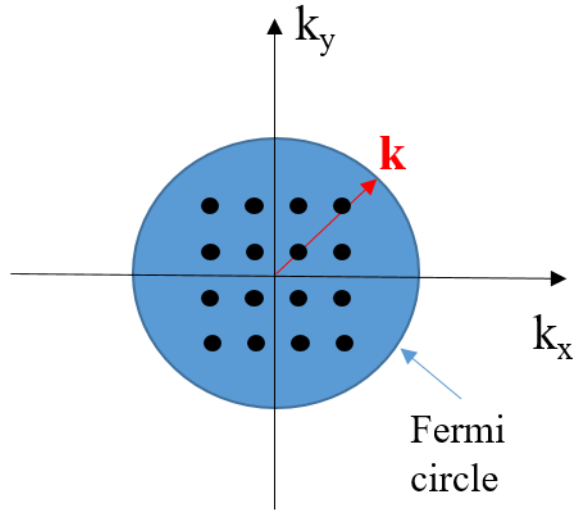


Figure 1.8. The scheme of 2D electron gas at the Fermi surface.

Thus, the Fermi level of graphene can be obtained by measuring the Dirac voltage as follow

$$E_F = \hbar v_F k_F = \hbar v_F \sqrt{n\pi} \quad (15)$$

where v_F is fermi velocity and n is carrier density.

Scattering Source of Doped Graphene

Graphene has extraordinary high mobility due to its unusual band structure. However, experimental results show three order of low mobility which coming from its surrounding and nature born. To overcome these obstacles, many scientists have been tried to reduce the scattering sources. The resistance of graphene can be estimated by charged impurity, defects, substrate induced optical phonon and lattice vibration.^[111] If we consider these short range and long range scatterers with the Drude model, we can convert total relaxation time to the total resistivity of graphene with scattering sources as follow.

$$\frac{1}{\tau_{tot}} = \frac{1}{\tau_{ci}} + \frac{1}{\tau_{sr}} + \frac{1}{\tau_{LA}} + \frac{1}{\tau_{PO}} \quad (16)$$

$$\sigma = ne\mu = \frac{ne^2\tau}{m} \sim \tau \sim \rho^{-1} \quad (17)$$

$$\rho_{tot} = \rho_{ci} + \rho_{sr} + \rho_{LA} + \rho_{PO} \quad (18)$$

The phonon effect is important to understand the transport in graphene, but it is still controversial at its origin. ^[111,146] Previous reports ^[111,192] has own picture to describe the phenomena of phonon scattering in graphene.

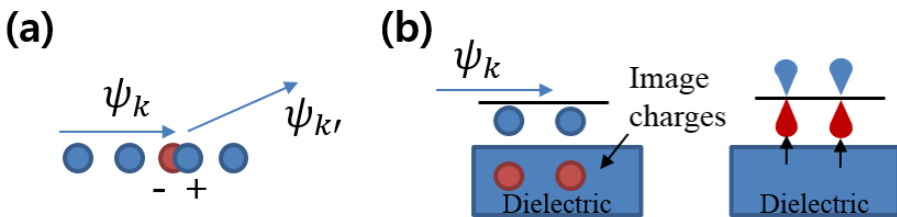


Figure 1.9. The scheme of phonon effects in graphene transport. (a) A Displacement of atoms results in the creation of a charge imbalance and electrons are scattered due to electric field. (b)The scheme of surface phonon scattering i) Polar optical phonons effect generated in terms of image charges

at the interface of dielectrics and 2D materials or ii) polar optical phonons induce the perturbation to anti-symmetric of C-C π -bonds.

The longitudinal acoustic phonon cause a displacement of carbon atoms resulting in the creation of a charge imbalance, thus electrons are scattered due to its electric field. While, the surface optical phonon scattering originated from the polar optical phonons in the dielectric surface (Figure 1.9)

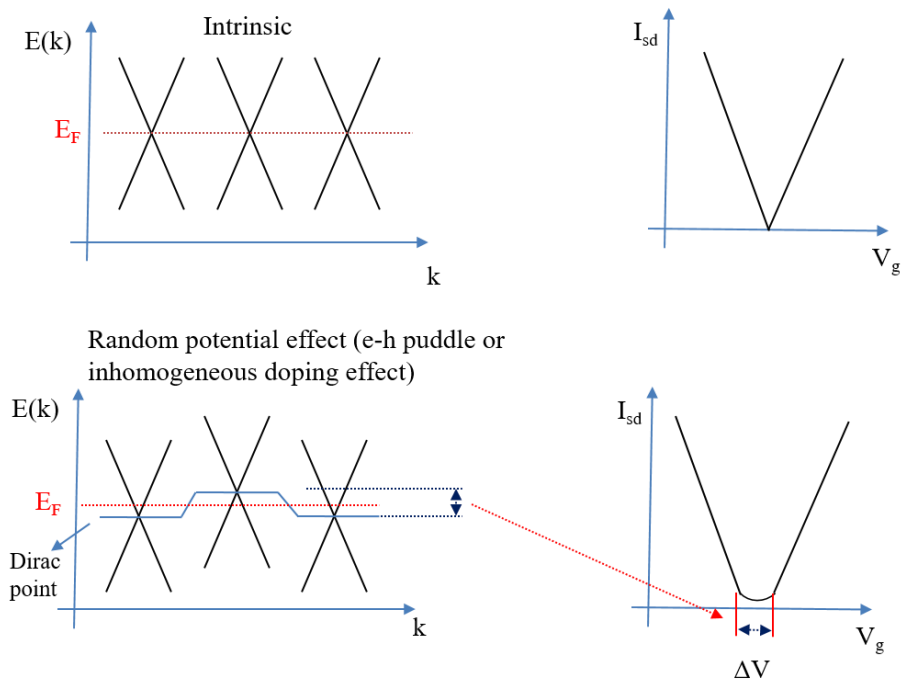


Figure. 1.10. The relation of random potential to I-V_g curves in intrinsic and extrinsic graphene.

The random potential from charged impurity can be estimated from the unchanged region of conductivity with gating. The unchanged region (ΔV) can be estimated by fitting the I-V_g curve, which is originated from charge traps at interface of graphene and substrate or dopants inhomogeneity (Figure 1.10). By finding cross point of the

horizontal line of minimum conductivity and straight line of linear dependent conductivity as a function of doping concentration (Figure 1.11), we can obtain the random potential density.

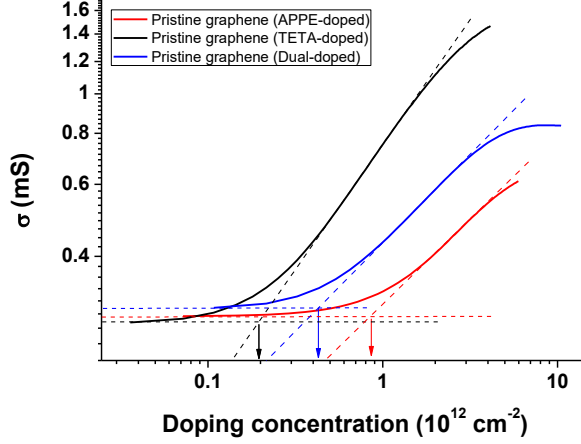


Figure 1.11. The conductivity of n-doped and undoped graphene as a function of gate voltage in a logarithmic scale to estimate the random potential density of graphene.

The $I-V_g$ curve of graphene devices can be fitted by flowing equation to obtain the mobility of graphene device.

$$\rho_{tot} = \rho_{residual} + \rho_n = \rho_{residual} + \frac{1}{n_{tot}e\mu} \quad (19)$$

$$n_{tot} = \sqrt{n_{imp}^2 + n^2} = 7.2 \cdot 10^{10} \cdot \sqrt{V_{imp}^2 + V_G^2} \quad (20)$$

Where $\rho_{residual}$ is residual resistance of graphene, n_{imp} =charged impurity concentration, n is doping concentration induced by gate electrodes and μ is mobility.

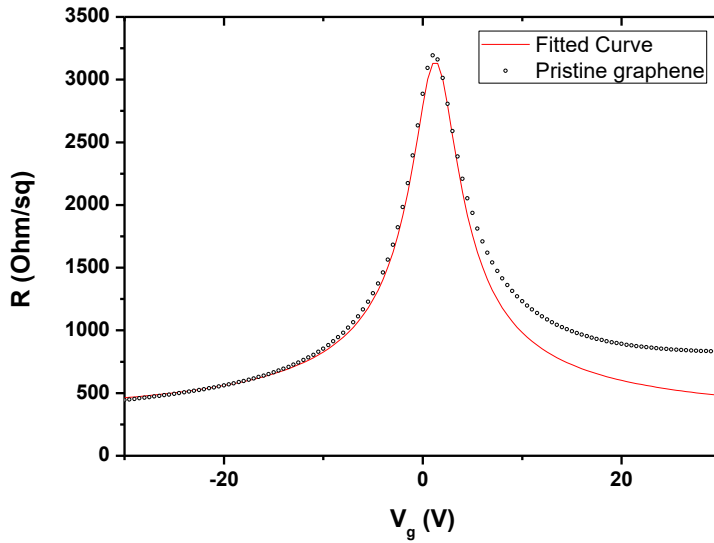


Figure 1.12. A resistance vs gate voltage of pristine graphene and red line is fitted curve using equation (19).

In fabrication and doping process of graphene device, representative factors should be considered as below to obtain low sheet resistance.

1. Quality of synthesized Graphene : mobility of graphene (μ), defects
2. Doping quality : homogeneous doping (Δn_{imp}), doping density (n), substrate effects (e-h puddles)
3. Temperature (T)

From equation (18), charge impurity concentration can be controlled by increasing graphene quality and polar optical phonon scattering can be changed by changing the substrate. The electron-phonon scattering issue was studied by experimentally and theoretically, but still it was in debate. The surface phonon modes in dielectric is crucial effects in graphene transport phenomena, which largely degraded mobility of graphene. Thus, surface phonon of SiO₂ is

considered as a scatterer which is act as a charged impurity at interface between graphene and SiO₂. By considering gate dependent resistance (ρ_0), remote interface phonon effect (ρ_{RIP}) and longitudinal acoustic phonon effect (ρ_{LA}), the sheet resistance can be expected to certain values as following equations (see Figure 1.13.)

$$\rho_{RIP}(V_g, T) \sim A \cdot n_{gate}^{-a} \left(\frac{B}{eEA/k_B T - 1} \right), \quad (21)$$

$$\rho_{LA}(T) = \left(\frac{h}{e^2} \right) \frac{\pi^2 D_A^2 k_B T}{2h^2 \rho_s v_s v_F^2} \sim 0.1 \cdot T \left(\frac{Ohm}{sq} \right) \quad (22)$$

Therefore, the high quality and high doping concentration of graphene sample are main keys to obtain the low sheet resistance, thus all these scattering sources need to concern.

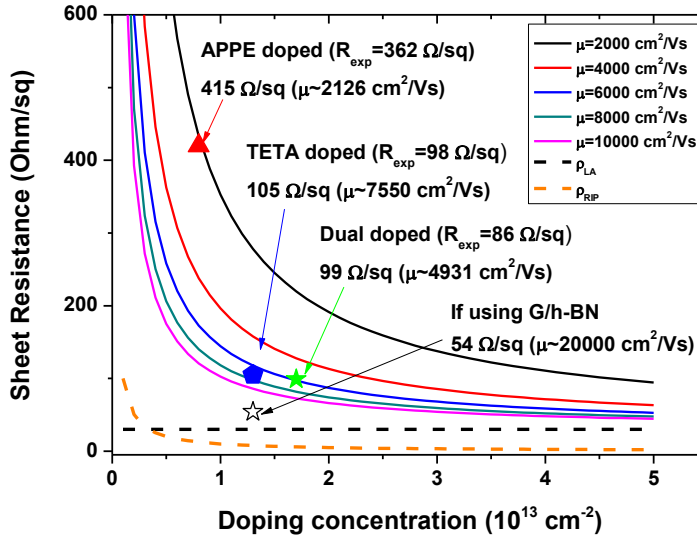


Figure. 1.13. Sheet resistance vs doping concentration plot with considering remote interface phonon and longitudinal phonon effect together.

1.4 Graphene Applications

Synthesis of graphene film

The synthesis of graphene film has been studied by various way, which can be classified by two ways: bottom-up and top-down approaches. Each synthesis method has advantages and disadvantages in its quality and size of graphene sample (as described in Table 1.2)

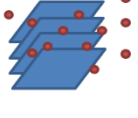
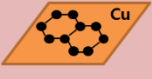
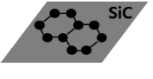
	Top-Down		Bottom-Up	
	Mechanical exfoliation	Chemical exfoliation	Chemical vapor deposition (CVD)	Epitaxial growth
Synthesis method	Exfoliated from graphite using scotch tape. 	Exfoliate graphite using acid. 	Using carrier gases with heating on catalysts (metal film). 	Growth of a graphene on top of a crystalline with heating (SiC). 
Quality (mobility)	High	Low	Relatively high	Relatively high
Size of sample	Small	Small but large amount	Depending on a substrate (up to ~10 inch)	Depending on a substrate (~4 inch)
Problems	Randomly obtained	Large amount of impurities and chemicals	Polycrystalline sample	High vacuum condition and crystalline substrates are needed

Table 1.2. Graphene synthesis methods and its advantages and disadvantages.

The exfoliated graphene is still popular for laboratory use but it is not suited to the electronics industry, whereas the other two options both have the potential for producing wafer-scale graphene. Graphene growth using chemical vapor deposition was achieved synthesizing monolayer graphene at 2008/2009. ^[20, 21] The research of CVD graphene is accelerated to scale up the size of graphene sample. There are many factors to concern applying industrial needs: size of graphene

sample, high quality, safety of catalyst gases and synthesis time and temperature. The CVD graphene of 30-inch scale (Figure 1.7) first reported by S.Bae et al. [22] was starting point for application of graphene. Recently, many scientists focused on its synthesis time and temperature by using liquid carbon source, halogen ramp assisted CVD and plasma supported CVD. [23-25]

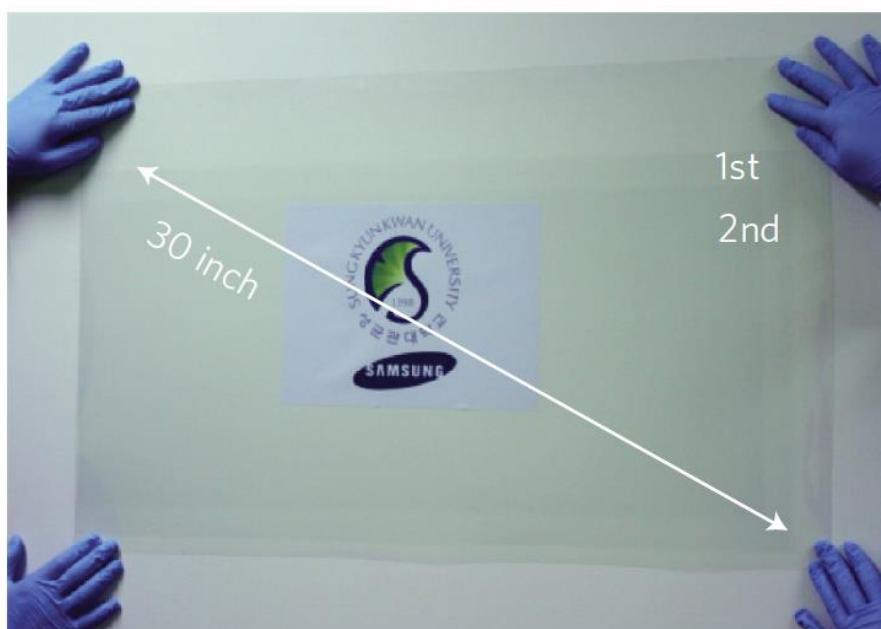


Figure 1.14. A photograph of 30-inch CVD graphene transferred on PET film

[Adapted from Ref.22]

Graphene heater

Transparent smart windows generally require transparency (T) to be 60–90% or higher and R_s to be 100–1,000 Ω/sq , depending on production cost, application and manufacturer. [28] An ITO film has been widely used as a transparent heater, but it exhibits a slow thermal response and requires complicated fabrication processes. For this reason, there have been many efforts to replace ITO films with a new type of transparent conducting film. The performance of single-walled carbon nanotube (SWCNT) sheets based heater shown in Figure 1.15. as demonstrated by Yoon et al. [26]

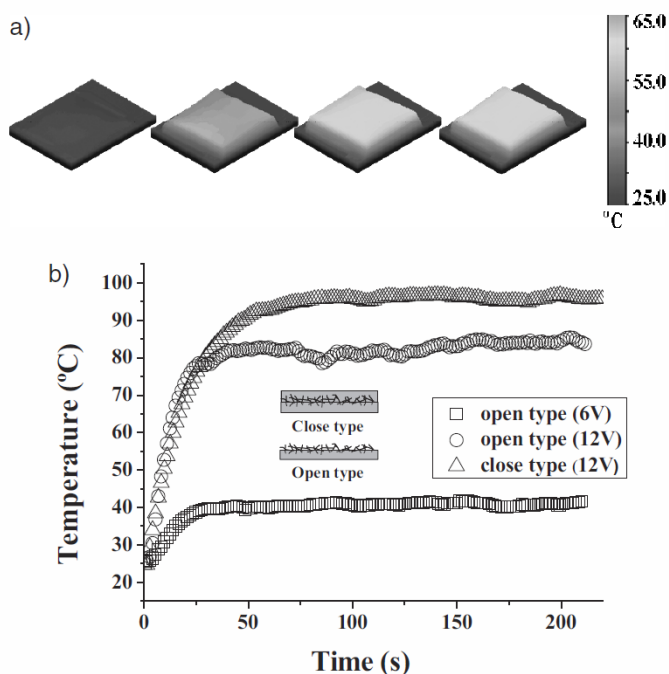


Figure 1.15. a) Temperature history, and b) temperature response of the SWCNT film surface on a PET substrate. The area of the SWCNT film was $4 \times 4 \text{ cm}^2$. The film thickness of the open configuration was $188 \mu\text{m}$, while the thickness was $250 \mu\text{m}$ in the closed configuration. [26]

While transparent SWNT films show a rapid thermal response and have a better heating performance than ITO films, but their fabrication process requires strong acid treatments, which limit the conductivity of SWNT-based conducting films. Moreover, the difficulty of selecting metallic SWNTs is main obstacle to achieve the enhancement of their optical transmittance (T_r) at a given sheet resistance ($R_s = \sim 180 \text{ Ohm/sq}$ at $T_r = 90\%$).^[27] Thus, using a scale-up chemical vapor deposition (CVD) graphene films is one of possible solution for transparent heaters to replace other materials. Recently, Graphene demonstrates exceptional optoelectronic properties that are superior to those of previously used transparent conducting materials ($R_s = \sim 43 \text{ Ohm/sq}$ at $T_r = 89\%$).^[28]

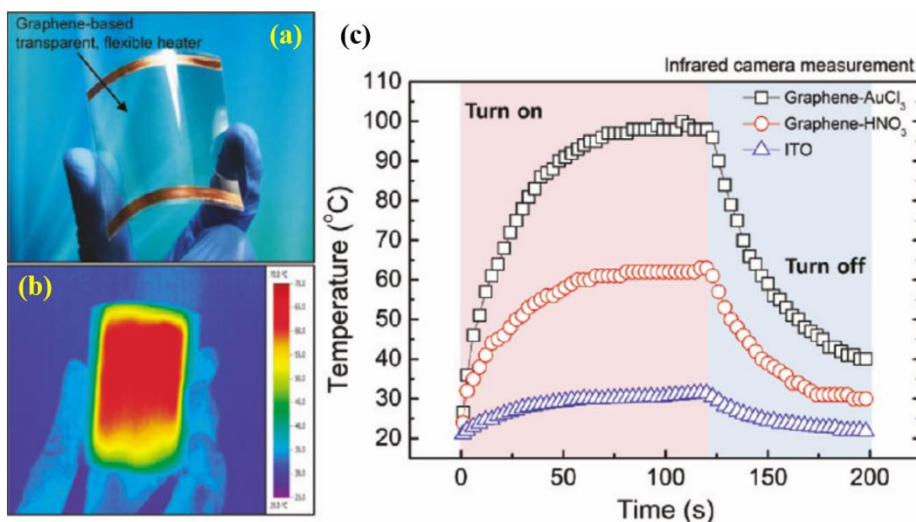


Figure 1.16. CVD graphene heater [Adapted from Ref.31]

Bendable display

Touch screens are visual outputs that can detect the presence and location of a touch within the display area, permitting physical interaction with what is shown on the display itself. ^[33] Touch panels are currently used in a wide range of applications such as cellular phones and digital cameras. Resistive and capacitive touch panels are the most common. A resistive touch panel comprises a conductive substrate, a liquid-crystal device front panel and a TCF. ^[33] When pressed, the front-panel film comes into contact with the bottom TCF, and the coordinates of the contact point are calculated on the basis of their resistance values. There are two categories of resistive touch screens: matrix and analogue. ^[113] The matrix has striped electrodes, whereas the analogue has a non-patterned transparent conductive electrode with lower production costs. The TCF requirements for resistive screens are $R_s \approx 500\text{--}2,000 \text{ } \Omega/\text{sq}$ and $T > 90\%$ at 550 nm. ^[33] Favourable mechanical properties, including brittleness and wear resistance, high chemical durability, no toxicity and low production costs, are also important. Cost, brittleness, wear resistance and chemical durability are the main limitations of ITO ^[34, 35], which cannot withstand the repeated flexing and poking involved with this type of application. Thus, for resistive touch screens there is an effort to find an alternative transparent conductor. Recently, graphene based resistive touch screen was reported. ^[30]



Figure 1.17. Graphene-based multi-touch screen showing excellent flexibility (left) and possible applications in bendable or foldable mobile devices (right) [Ref. 30].

Chapter 2 Experimental

2.1. CVD Graphene Sample Preparation

Graphene film was synthesized on a 25 μm thick copper foil through chemical vapor deposition (CVD) method (Figure 2.1 showed CVD system), using methane (50 sccm) and hydrogen (5 sccm) gas with vacuum pumping at 1000 $^{\circ}\text{C}$. Graphene transfer step was completed according to the conventional processes (Figure 2.2): PMMA was spin-coated on top of graphene and copper foil was etched in ammonium persulfate solution (20 mM with distilled water). A highly P-doped Si substrate covered with a 300 nm thick SiO_2 was used for the electrical measurement of graphene field effect devices. Free-standing graphene on distilled water was carefully transferred to SiO_2/Si substrate and PMMA was removed in acetone. A fully grown CVD graphene was checked by optical microscope (Figure 2.3).

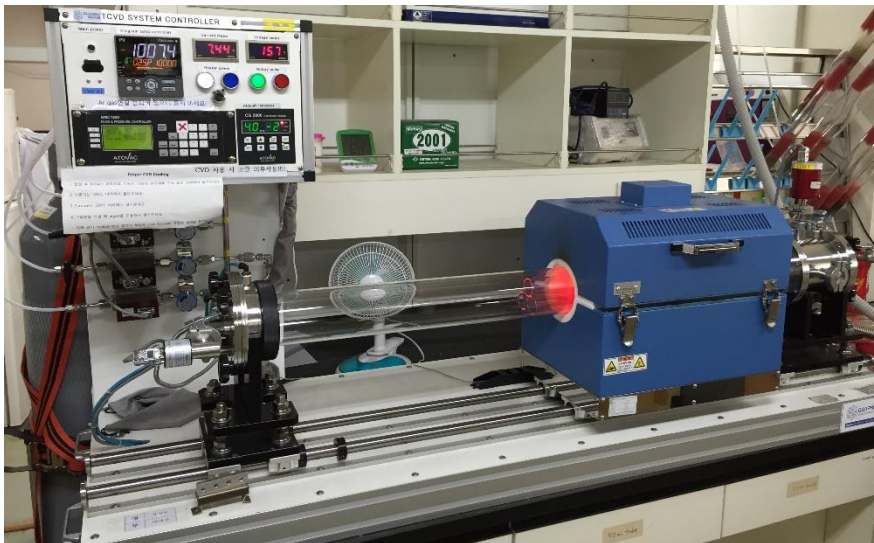


Figure 2.1. 4 inch CVD growth system

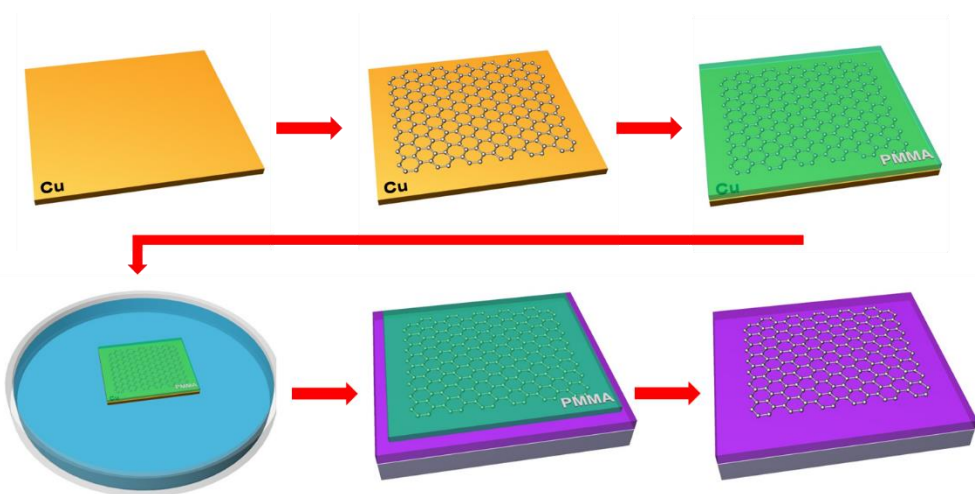


Figure 2.2. Schematic illustration of the synthesis and transfer processes of large-area CVD graphene films.



Figure 2.3 The optical image of CVD grown graphene (scale bar = 10 μm).

2.2 Chemical Doping Methods

The dipping method and the spin-coating method are conventionally used in the chemical doping of graphene studies and has advantages of controlling the chemical density. However, each dopants has its structure difference. For example, benzene ring contained dopants are easy to stick the graphene surface due to π - π interaction, while ethylene amines are aggregated due to the grain boundary of polycrystalline graphene. Thus, proper doping method is needed to dope the surface of graphene effectively. The chemical doping methods of graphene used in this study informed as below and depicted in Figure 2.4, and each four different methods were used as below

1. Dipping method
2. Spin coating method
3. Vapor-phase doping method
4. Construction of Self-assembled monolayers(SAMs)

The dipping method and the spin-coating method doping is carried out using the proper concentration of doping solution and time and then N_2 gas is blown to remove additional dopant solution on top of graphene surface. The vapor-phase doping method is using thermally evaporated dopants to effectively cover graphene surface which is similar to metal deposition on target material. Lastly, to construct the self-assembled monolayers (SAMs) on SiO_2 substrate, a SiO_2 substrate washed in Piranha solution ($H_2SO_4:H_2O_2=1:3$) for 30 mins with $120\text{ }^\circ\text{C}$ heating and the rinsed with distilled water. The cleaned SiO_2 substrate dipped in an amine-SAMs solution (3-aminopropyltriethoxysilane (99%, Aldrich) $40\text{ }\mu\text{l}$ in distilled water 20 ml) for 30 mins and heated ($120\text{ }^\circ\text{C}$) for 20 mins for silanization. In case of methyl-SAMs we used

Octadecyltrichlorosilane (90%, Aldrich) in Toluene (10 mM) and dipped for 15 hrs, and then same silanization method was used.

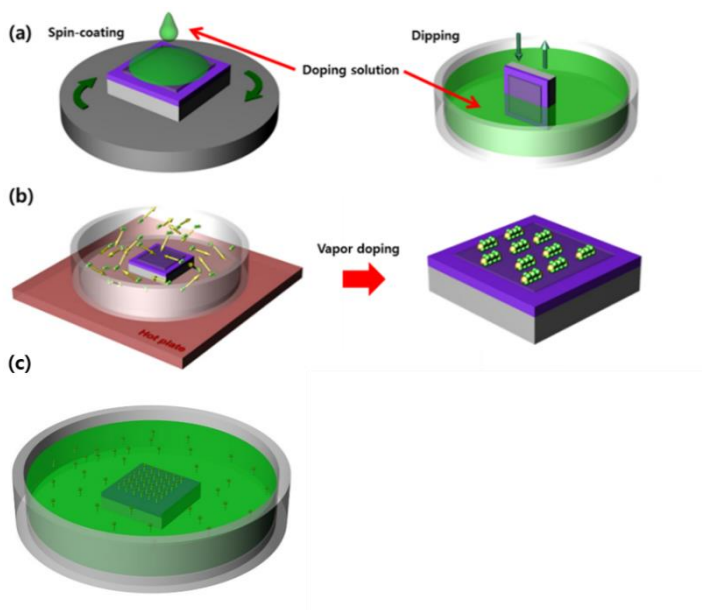


Figure. 2.4. The doping methods (a) dipping and spin-coating method, (b) vapor-phase doping method and (c) construction of self-assembled monolayers.

2.3 Optical Measurement: Raman Spectroscopy

Raman Spectra of doped graphene

Raman spectroscopy has played an important role in the characterization of 2D materials [6-7,19], and has also become a useful tool for understanding the behavior of electrons and phonons in graphene and also for characterizing the doped graphene [20-25]. The renormalization of the phonon energy is also strongly dependent on the Fermi level position, so that it can be tuned by doping graphene with electrons or holes. In fact, if one changes the Fermi energy of the system, there is a reduction in the interaction between phonons and interband electron-hole pairs, thus changing the effective force constant of these atomic vibrations.

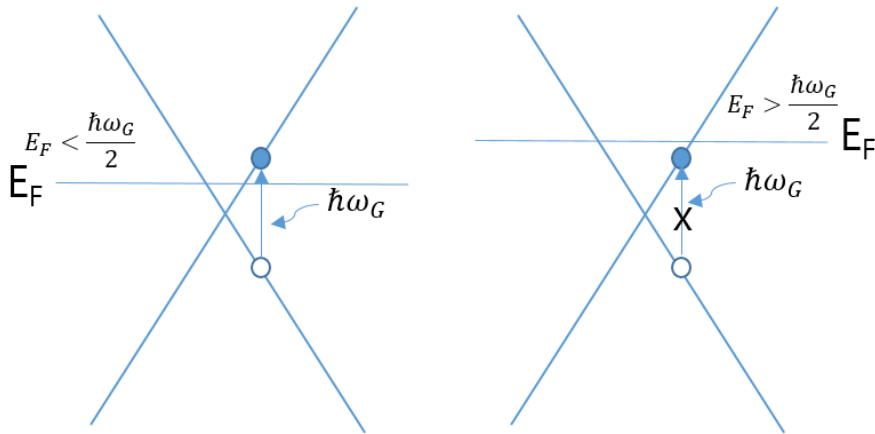


Figure 2.5. The renormalization of the phonon energy is allowed due to Pauli exclusion principle when the change in the Fermi energy E_F is smaller than half of the phonon energy $\hbar\omega_G/2$ (left figure) and it is suppressed for $E_F > \hbar\omega_G/2$ (right figure).

This renormalization, which is very effective when chemical potential is smaller than half of the incident phonon energy ($E_F < \hbar\omega_G/2$), while it is forbidden due to Pauli exclusion principle when the change in the Fermi level is larger than half of the G-band phonon energy since, as shown in Figure 2.5. [49, 50]

Figure 2.6 shows a theoretical calculation of both the phonon energy and linewidth as a function of the electron density, studied by Lazzeri and Mauri [51] at three different temperatures. The phonon linewidth dependence, which exhibits a barrier-like behavior at low temperature, is also smoothed out at room temperature.

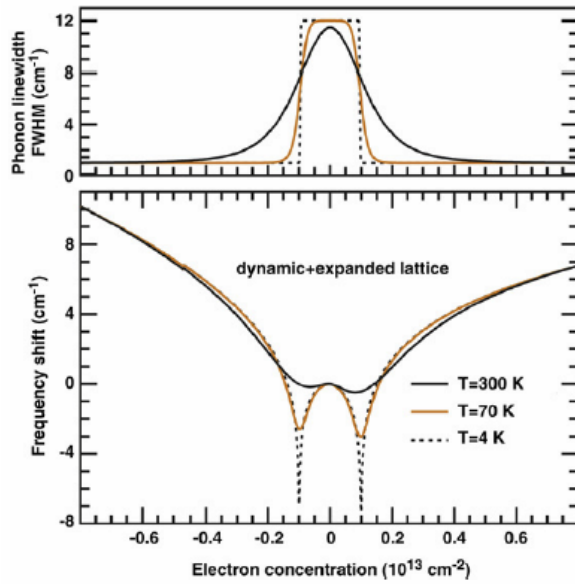


Figure 2.6. Linewidth and Frequency of the Raman G band as a function of the electron concentration which is proportional to the square of the Fermi level energy. Adapted from Ref. [51].

So, by moving the Fermi level from the Dirac (neutrality) point, we expect mostly a hardening of the phonon energy and a narrowing of the phonon linewidth, which is related on the full-width half maximum of G peak.

The coupling between phonons and electron-hole pairs renormalizes the phonon energy of graphene, and the renormalization depends on the electron and hole concentrations. The effect is strong near the Γ and K points in the Brillouin zone considering phonon energy conservation. Thus phonons that are important for this process are those with $q=0$ and for $q=K$, where K denotes the Brillouin zone corner of graphene. The zone center E_{2g} phonon mode of graphene, which gives rise to the Raman G-band, is known to exhibit a very strong coupling with electron-hole pairs. This effect can be measured directly by Raman spectroscopy, as it probes the G band frequency as a function of Fermi energy. The modification of the Fermi level of graphenes can be done by electrochemical methods^[52] or by an electric field effect when a gate voltage is applied between the Si substrate and the graphene, deposited on the top of a Si/SiO₂ substrate^[53, 54]. Recent experimental Raman studies of monolayer graphene with the modification by gate voltage shown that the Fermi level induces changes in the frequency and width of the G-band, appearing in Raman spectra around 1580 cm⁻¹. Figure 2.8 shows the Fermi energy dependence of the frequency and width of the Raman G-band in monolayer graphene.^[54] A similar result was reported by Pisana et al.^[53]. The G-band frequency of monolayer graphene increases and the G-band linewidth decreases when the Fermi level is moved away from the

Dirac point, due to doping by either electrons or holes (positive or negative changes in the Fermi level).

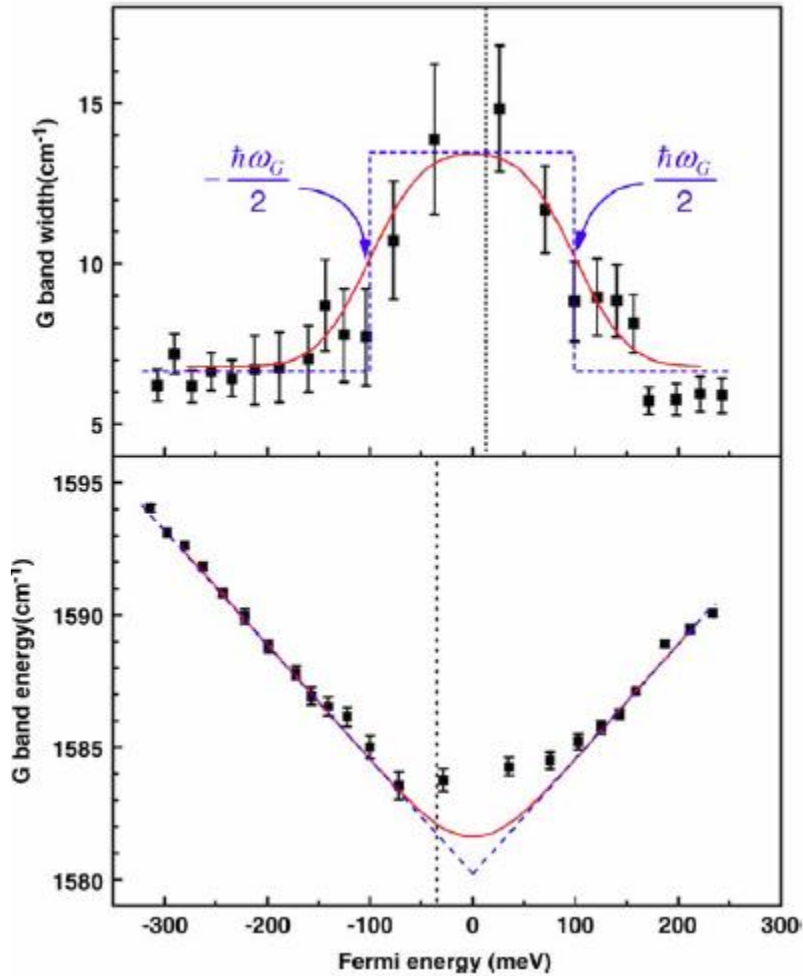


Figure 2.7. G band FWHM linewidth (upper figure) and energy (lower figure) of monolayer graphene, as a function of the Fermi level energy. Adapted from Ref. [54].

2.4 Graphene Field Effect Transistor

Generally, field effect transistor (FET) is a three-electrodes system with majority carriers during conduction (For Si n-MOSFETs, the electrons that conduct the current are actually the minority carriers in the p-doped substrate. Besides the dual-gated FET has four electrodes). It has the advantages of high off-state resistance, low noise, low power, large dynamic range, easy integration and a wide safe operating range, making it to be a strong contender for many transistor applications. The gate, drain and source electrodes in FETs are roughly equivalent to the base, collector and emitter electrodes in bipolar junction transistors (BJT), respectively. Except for the junction FET (JFET), other FETs have a fourth terminal which is said to be the body, base, bulk or substrate. Recently, many different FETs have been developed to cater to the requirements of modern electronics technology, such as Si-based field effect transistors (Si-based FETs), carbon nanotube field effect transistors (CNT-FETs), organic field effect transistors (O-FETs), and so on. The quantum interference effect transistor has been proposed theoretically and is based on a single molecule^[55, 56] to cater to the further miniaturization. It is another requisite feature in modern electronic technology. Nevertheless, owing to its small size, it is difficult to fabricate the various leads for the single molecule.

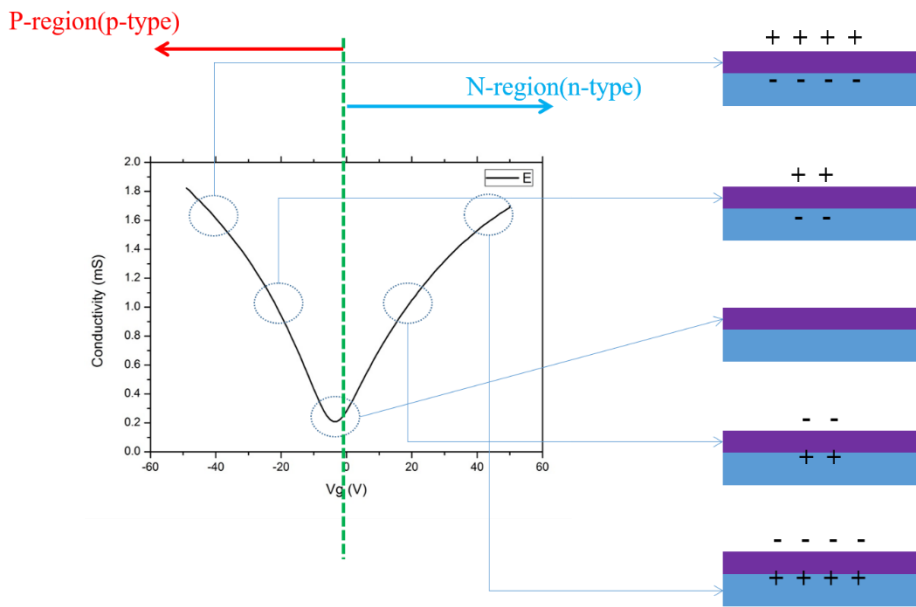


Figure 2.8. Current vs gate voltage curve of pristine graphene field effect transistor (left) and electric induced doping scheme (right)

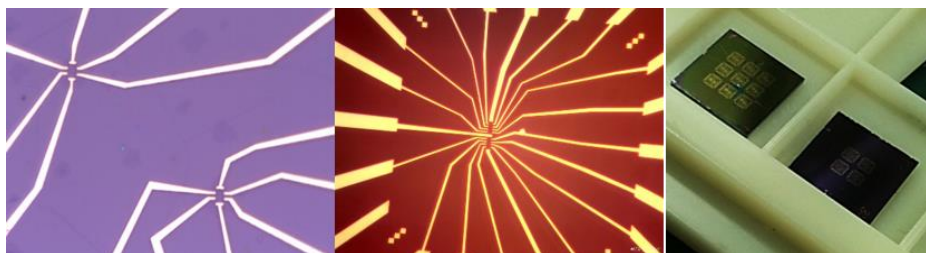


Figure 2.9. Optical image and picture of fabricated graphene devices

2.4.1 Fabrication Process

Sub-milimeter scale device

Chrome (5 nm) and gold (30 nm) layers were deposited thermally for metal contact of 3-terminal graphene device with pre-patterned stensile mask. Graphene channels were isolated through electron beam lithography. To avoid inconsistent growth condition, we used graphene samples grown from a single batch. Each device was fabricated with 200 μm width and 50-250 μm length. Before doping the graphene film, thermal annealing was carried out at 300 $^{\circ}\text{C}$ for 1 hour under argon and hydrogen gas environment to remove PMMA residues and trapped water after device fabrication.



Figure 2.10. Electron beam and thermal evaporator

Micrometer scale device

The conventional electron beam lithography technique was used for micrometer size graphene field effect transistor (Figure 2.11). Firstly, CVD graphene was carefully transfer onto target substrate (highly p-doped Si with 300nm SiO₂) and then rinsed by acetone around 3hours. To spin coat the e-beam resist, PMMA 950K A5 (Microchem Inc.) was used with spinning speed of 4000 rpm for 2 minutes and then polymerized 2 minutes at 180 °C. JEOL SEM-2010J and lithography system was used for micro lithography. After e-beam lithography, patterned substrate was dipped into MIBK:IPA (1:3) solution to develop the desired pattern. Patterned electrodes were thermally deposited by metal source (Cr 5nm/Au 30nm). To remove the useless graphene, another E-beam lithography pattern for isolating graphene the channel with same procedure. The exposed part of graphene was removed by reactive ion etching (RIE) method with 10 sccm flow of oxygen gas and 50 mW plasma power. For measurement in low temperature, 44 pins chip was used. Silver paste is used to attach the graphene device to the chip and wire bonder (Figure 2.13) with Al or Au wire was used to connect the graphene device to LCC chip.

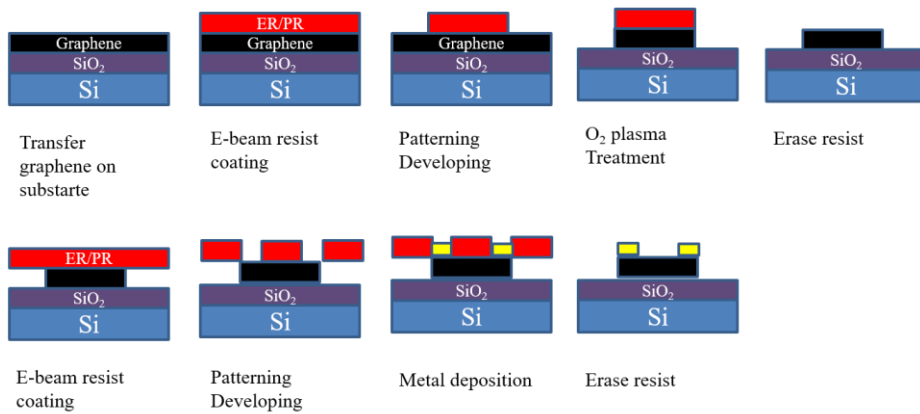


Figure 2.11. The fabrication process of graphene field effect transistor



Figure 2.12. Reactive ion etching (RIE) system



Figure 2.13. Wire-bonder (West bond Inc.)

2.4.2 Electrical Measurement Technique

Electrical conductivity or resistance of n-type and/or p-type doped graphene can be measured by field effect devices. The conductivity or resistivity of graphene shows linear dependence as a function of gate voltage without near the Dirac point. The minimum conductivity (or maximum resistivity) point or the Dirac point of intrinsic graphene can be found at the zero gate voltage, and the point shifts toward positive (negative) gate voltage as a consequence of p-type (n-type) doping of graphene.

In electrical measurements of graphene field effect transistors, Agilent B2912A (Figure 2.15) were used on 3-terminal geometry with source, drain and gate in air, sharp tungsten tips were used to contact the graphene device to measure using probestation (Figure 2.14) . Constant 10 mV voltage was applied from source to drain during the measurement. The sheet resistance of the graphene (50 μm \times 50 μm square geometry) was measured using a four-point probe with a nanovoltmeter (Keithley 6221, 2182A) and the Van der Pauw method was applied. The sheet resistance of graphene was obtained using the following equation:

$$R_s = \frac{\pi V}{\ln 2 I}$$

Liquid nitrogen type and Helium gas circulation type cryostat were used for graphene transport measurement at low temperature (shown in Figure 2.16).

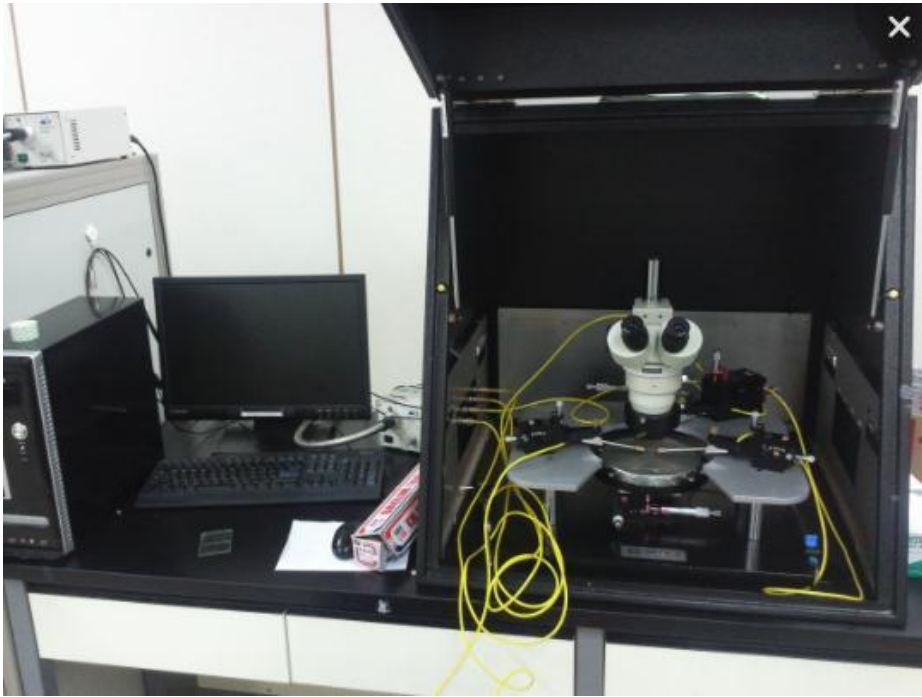


Figure 2.14. Probe station with ambient condition



Figure 2.15. Agilent B2912A source-meter

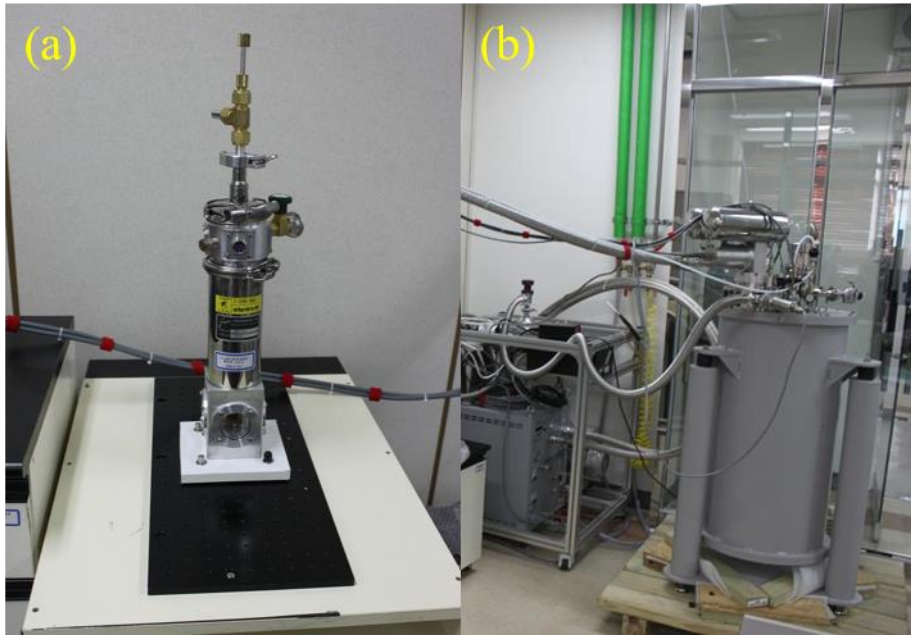


Figure 2.16. Cryostats for transport measurement (a) Liquid Nitrogen cooling type (temperature down to 77 K) (b) Helium gas circulation type with superconducting magnet (temperature down to 4 K, magnetic field up to 9 Tesla)

Chapter 3 Efficient N-Doping of Graphene Films by APPE (Aminophenyl Propargyl Ether): A Substituent Effect

3.1 Introduction

Graphene has received much attention since it came to the real world in 2004 owing to its outstanding electrical, mechanical, and chemical properties.^[73] Recent advances in graphene synthesis by chemical vapor deposition (CVD) method have enabled various practical applications such as transparent electrodes for display and energy devices.^[74] Nevertheless, the electrical properties of graphene such as work-function and conductivity need to be further engineered to enhance the performance of the graphene-based devices by controlling the interface with other materials.^[19,79-84] In this regard, the chemical doping of graphene is very crucial as proper doping can finely tune the electrical properties of graphene. The chemical doping of graphene is efficient due to the fact that the atoms on graphene are fully exposed and very sensitive to adsorbed molecules. Although both p/n-doping methods are essential for optimizing the performance of graphene-based electronic devices, the molecular n-doping of graphene has been relatively less investigated compared to p-doping as graphene is more readily p-doped by adsorbates.

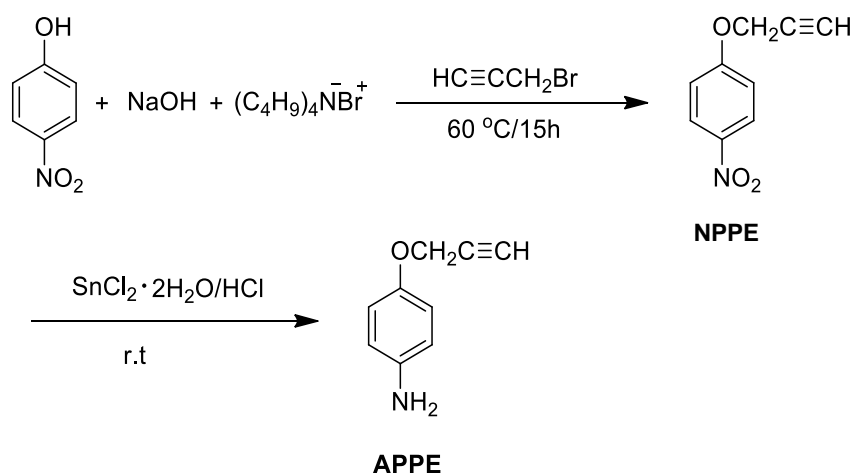
Here, we devised a facile and effective n-doping method for graphene, utilizing the electron-donating nature of amine functional groups attached to phenyl propargyl ether. Although several works on graphene n-doping have already been reported in the past few years,

most of their doping methods resulted in insignificant n-doping effect and/or inevitably degraded graphene quality. ^[19,79-84] In 2009, Xiaochen Dong, M. S. Dresselhaus and co-workers explored n-doping of single layered graphene with various aromatic molecules exhibiting respectable n-doping efficiency. ^[19,87] However, to the best of our knowledge, there is no report controlling an aromatic molecule's substituents to induce both p/n-doping as needed.

3.2 Experimental

P-nitrophenyl propargyl ether (NPPE) was prepared by the reaction between 5.65 g of p-nitrophenol dissolved in 50 ml of 0.8 N aqueous NaOH and 1.28 g of propargyl bromide in the presence of a phase transfer catalyst. NPPE was reduced with 28.8 g of stannous chloride in 70ml of concentrated HCl. The crude product was purified by distillation (bp 95 °C at 10 mmHg) and characterized by the comparison of ^1H NMR data with that of known product.

Graphene field effect transistors were constructed from monolayer graphene grown with chemical vapor deposition (CVD).^[13] Electrodes consisting of a 5 nm chrome (Cr) sticking layer and a 30 nm gold (Au) layer were thermally deposited on top of the graphene with patterned stencil mask. In addition to this, we constructed a graphene channel using the conventional e-beam lithography method.



Scheme 3.1. Preparation procedures of nitrophenyl propargyl ether (NPPE) and aminophenyl propargyl ether (APPE).

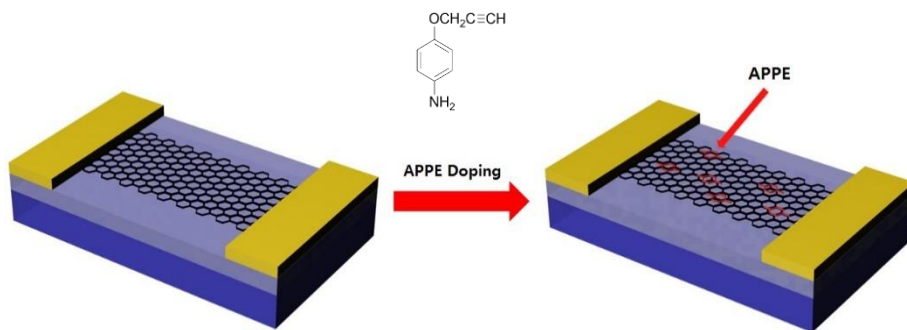


Figure 3.1. Doping procedure of graphene with APPE.

3.3 Results and Discussion

We suggested aminophenyl propargyl ether (APPE, Scheme 3.1)^[78] to be an n-type dopant based on its capability of interacting with graphene through π - π interaction and the amino group's strong electron-donating property. Furthermore, the acetyl group of APPE can be utilized for further reaction with other organic functionalities using click chemistry.^[22] APPE was synthesized according to the known procedure which is described in Scheme 1.^[78]

We had successfully doped graphene with APPE by dipping graphene FET into a solution of APPE and Tetrahydrofuran (THF) (Figure 3.1). The SEM image of FET device is shown in Figure 3a. In order to examine the type of doping APPE induces, we took the Raman spectrum of APPE doped graphene FET from which we observed two conspicuous characteristics (Figure 3.2a).

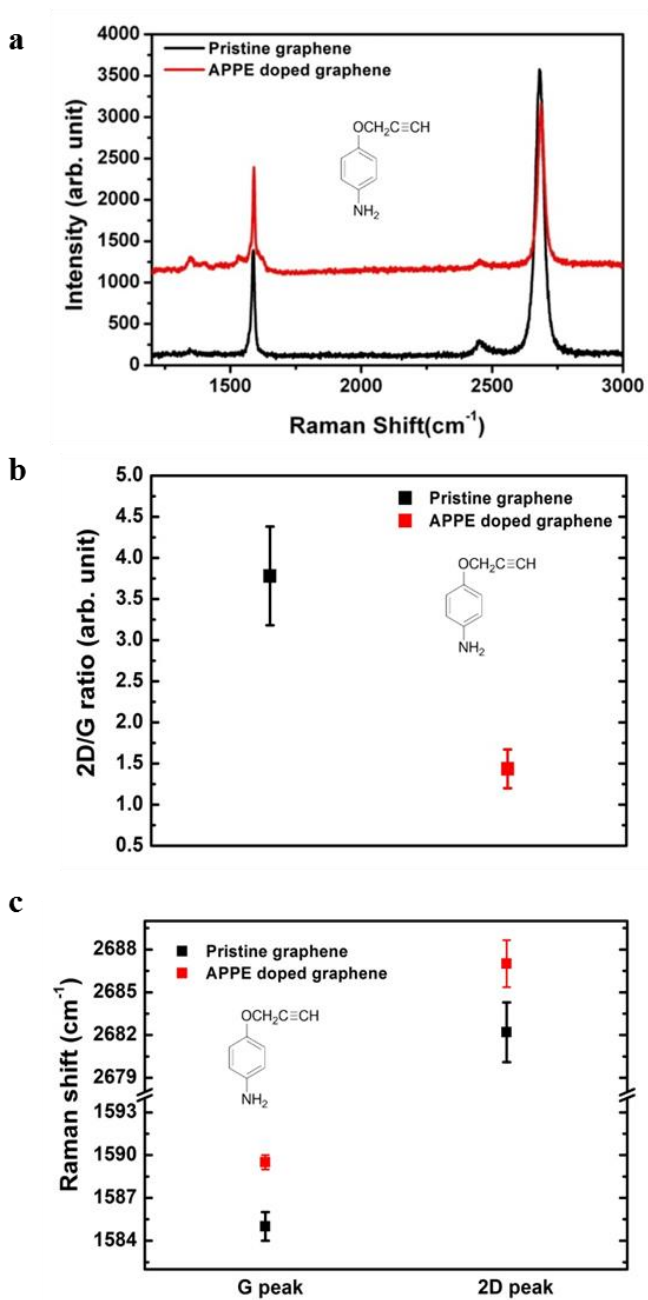


Figure 3.2. Raman spectra of pristine and APPE doped graphene. **a**, Raman spectra obtained from pristine graphene (black, bottom) and APPE doped graphene (red, top). **b**, Statistical intensity ratio 2D/G for pristine graphene (black) and APPE doped graphene (red). **c**, Peak shift of 2D/G for pristine graphene (black, bottom) and APPE doped graphene (red, top).

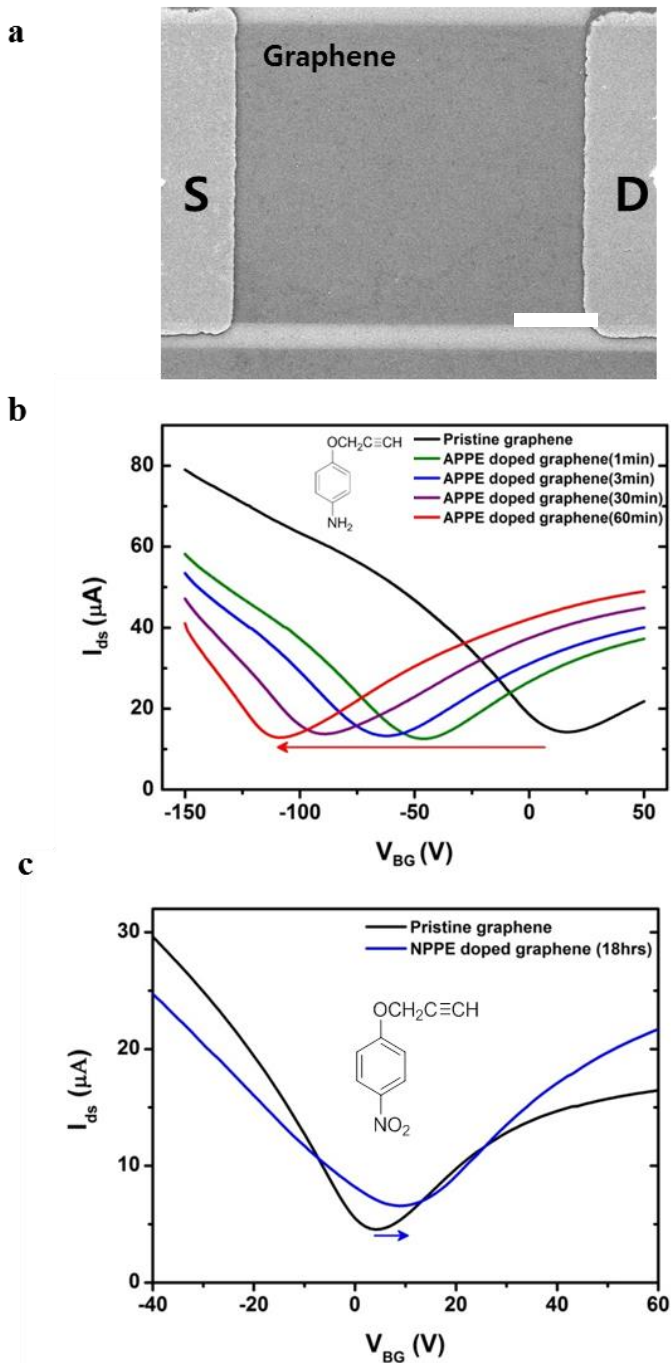


Figure 3.3. Graphene devices of APPE and NPPE doped graphene. (a) SEM image of the FET device (scale bar: 50 μ m). Conductivity-gate voltage curves of the graphene and APPE (b) and NPPE (c) doped graphene FETs measured at $V_{sd}=0.01$ V.

First, as known in other n-doped graphene examples,^[19,87] the statistical intensity ratio 2D/G of the APPE doped graphene was reduced by 40% compared to pristine graphene, indicating that the graphene FET was doped (Figure 2b).^[19,87] But to our surprise, both of the 2D and G peaks in the spectrum were upshifted, which has been unprecedented in the previous studies on n-doped graphene; the Raman spectrum in the preceding reports have exhibited down shifted G peak as opposed to the 2D peak.

In addition to these Raman spectrum data, as shown in figure 3.2a, small D band peak appeared at 1350cm^{-1} , indicating increasing disorder of the graphene basal plane. The appearance of a D band through π - π interaction between aromatic molecules and graphene is explained clearly in the reports of Xiaochen Dong, M. S. Dresselhaus.^[19,87] To identify which type of dopant APPE is, we examined transport measurements of APPE doped graphene FET in ambient conditions, where the Dirac voltage (the gate dependence of minimum conductivity) shift depends on the levels of electron or hole doping.^[85] In this experiment, as shown in Figure 3.3a, graphene FET doped with APPE showed a sharp negative shift of Dirac voltage when pristine graphene was taken as a control. This result clearly indicates that APPE is an n-type dopant in graphene FET.

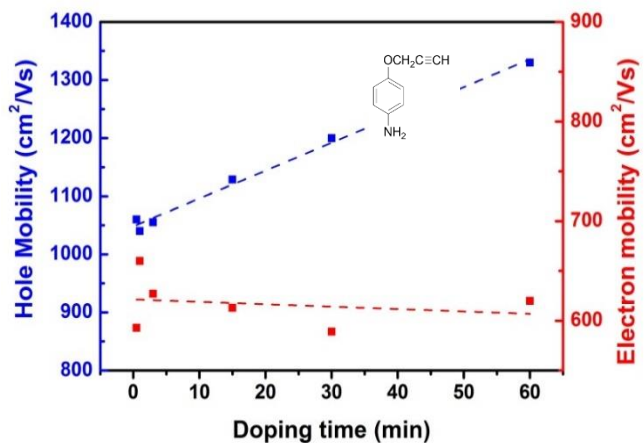
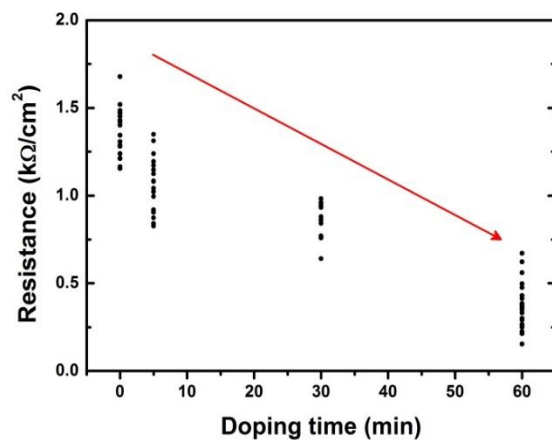


Figure 3.4. Sheet resistances (a) and charge carrier mobilities (b) of APPE doped graphene FETs.

We also compared the n-doping efficiency of our method to those of other known procedures (Table 3.1). The results show that our n-doping method induced more potent n-doping effect than these reported methods.^[79,80]

Table 3.1. Comparison between Dirac voltage values after different n-doping treatments (V)

<i>N-Doping by</i>	<i>Dirac Voltage Shift (V)</i>
Au Nanoparticles (Ref.79)	53.1
SAM-NH ₂ (Ref.80)	110
APPE	133

In order to employ n-doped graphene FET in electronic applications, it is important to examine its electrical properties. To that end, we measured the sheet resistance as a function of doping time (Figure 3.4a). Notably, after the graphene was n-doped with APPE, the sheet resistance of graphene was reduced to three-fold less than that of pristine graphene.

To confirm the assumption that the doping effect depends on a molecule's functional substituent, we measured the transport property of nitrophenyl propargyl ether (NPPE) doped graphene FET as a comparison. As opposed to APPE's electron-donating amine group, NPPE's electron-withdrawing group was assumed to make p-doped

graphene. As it is shown in Figure 3.3b, Dirac point of NPPE doped graphene was slightly shifted to the positive direction, showing that it actually induces p-doping.

In organic chemistry, the Hammett equation has been widely used to evaluate organic reactions and their mechanisms (equation 1).^[86] The same equation can also be utilized as an empirical reference to determine the substituent effect.

$$\rho_X = \log K_X - \log K_H \quad (1)$$

While K_H is the ionization constants of benzoic acid in water at 25 °C, K_X refers to the corresponding constant for para-substituted benzoic acid. These ρ values also represent the electrical property of a substituent. For APPE, the substituent values of amine and acetylene groups are -0.66 and 0.23, respectively. As a reference, the substituent value of nitro group in the Hammett equation is 0.778. These values indicate that acetylene and nitro groups' electron withdrawing properties, which might explain the unconventional G peak upshift in Raman spectrum unlike other n-doped graphene examples. Finally, we predict that the presence of acetylene group could enhance the hole mobility of APPE doped graphene FET only, making the electron mobility almost a constant (Figure 3.4b) might be originating from the screening effect of APPE on graphene.^[94]

3.4 Summary

In conclusion, we found APPE as a new graphene n-dopant without degrading the quality of intrinsic graphene. We proved APPE's intense n-doping effect by examining the Raman spectrum and measuring the transport property. We also examined the sheet resistance of APPE doped graphene FET for its applications in electronics. In addition, we suggest the n-doping mechanism by using the Hammett equation. We also confirmed that the doping effect of a molecular framework strongly depends on the functional substituents as changing APPE's substituent to electron withdrawing nitro group (NPPE) resulted in slight p-doping effect. Since APPE has acetylene group as a substituent, it might be able to carry out click chemistry^[22] as well, making it a more versatile dopant. As a matter of fact, the usage of APPE as a tool for functionalization of CNT through click coupling has been previously reported.^[88] This might suggest that APPE and NPPE doped graphene can be further applied to electrochemical biosensors with n-type and p-type graphene in the near future.^[89-93]

Chapter 4 Vapor-Phase Molecular Doping of Graphene for High-Performance Transparent Electrodes

4.1 Introduction

Graphene has been reported as one of the most fascinating two-dimensional materials¹ owing to its outstanding properties including flexibility,^[95] high mobility,^[96] transparency,^[97] heat dissipation ability,^[98] and so further. Recently, graphene has also shown potential to be adopted in optoelectronics^[99] or flexible electronics,^[22] especially in conducting electrodes due to its unusual band structure¹ and electrical tunability. To employ graphene in practical electronic devices, however, it is necessary to enhance its conductivity and control the work function appropriately, which can be performed by various doping methods including atomic substitution,^[17,100] molecular adsorption,^[13,101-103] covalent functionalization,^[19,82,83,104-106] substrate induced doping,^[80,107] polymerization on graphene,^[108,109] and the use of metallic thin films or nanoparticles.^[79,110,111] The substitution of carbon atoms with B or N as well as the covalent functionalization are advantageous in terms of long-term stability, which is, however, unfavorable due to significant decrease in carrier mobility and conductivity.

In this regard, the non-destructive and non-covalent doping by chemical species is favored, but it also has an instability problem that the molecular dopants tend to gradually evaporate from the surface of graphene. This instability issue is more important for n-dopants as it

easily reacts with oxygen or water molecules in air. Thus, several groups have suggested stable n-doping methods based on encapsulation by spin-coated polymers^[108] and nanoparticles.^[112] However, the doping strength of these methods is not strong enough to control the conductivity and work-function of graphene, efficiently. In addition, the doping by spin-coating or dipping (Figure 4.1a) using highly concentrated and reactive solution often results in contamination or damage by undesirable reactions. For such reasons, developing a highly stable, uniform and non-destructive yet intense n-doping method has been strongly demanded.

Thus, we report a simple method to tune the electrical properties of CVD graphene through n-doping by molecular vapors, where the dopants in vapor phase are mildly adsorbed on graphene surface without direct contact with solution (Figure 4.1b). To investigate the dependence on functional groups and molecular weights, we selected a series of ethylene amines as a model system, including ethylene diamine (EDA), diethylene triamine (DETA), and triethylene tetramine (TETA) with increasing number of amine groups and different vapor pressures (Table 4.1 and Figure 4.1c). The amine group is widely used as a good electron donor for various chemical reactions, which has been utilized as an n-dopant for graphene.^[13,80,83,103] Therefore, it is expected that the amount of electrons injection per covered area increases with the number of amine groups. On the other hand, the vapor pressure of DETA and TETA is very low at ambient condition, so the temperature needs to be elevated for efficient vaporization. Thus, we treated graphene with EDA, DETA, and TETA at 70 °C, and found

that the doped graphene exhibits strong and stable n-doping characteristics increasing with number of amine groups. In particular, the sheet resistance of graphene is measured to be $98 \pm 12 \Omega/\text{sq}$ after doping by TETA, which is believed to be the best conductivity for n-doped monolayer graphene. The doping and stability dependence on number of amine groups and molecular weights were carefully studied through atomic force microscopy (AFM), Raman, UV/Vis spectroscopy and various electrical measurements at different temperatures as discussed below.

Table 4.1. Comparing of three types of ethylene amines molecules

	<i>No.</i> <i>Amines</i>	<i>Molecular</i> <i>Weight (g mol⁻¹)</i>	<i>Boiling</i> <i>Point</i> <i>(°C)</i>	<i>Vapor</i> <i>Pressure</i> <i>at 20 °C</i> <i>(Pa)</i>	<i>Vapor</i> <i>Pressure</i> <i>at 70 °C</i> <i>(Pa)^[113,114]</i>
EDA	2	60.1	116	1,300	~ 20,000
DETA	3	103.17	204	10	~ 460
TETA	4	146.23	267	<1	~ 13.5

4.2 Experimental Methods

Doping method.

In the vapor-phase doping method, EDA, DETA, and TETA molecules were commercially purchased at Sigma-Aldrich. Vapor doping was carried out in petri-dish at 70 °C, baking on a hot plate with molecule droplet on tissue for 30 minutes in air (Figure 4.1b). Finally, EDA, DETA and TETA molecules were deposited on graphene surface as depicted in Figure 1c. Spin-coating performed under 3000 rpm speed for 1 minute by commercial spin-coater, and graphene on SiO₂ were mildly soaking into doping solution with 30 minutes. The concentration of ethylene amines is 0.1 mole/L in ethanol, was used in spin-coating and dipping doping method.

Characterization method.

The Raman spectra were measured using Renishaw inVia Raman Microscope with 1 mW 514 nm Ar laser with the spot size of 2 μm. Topological characterization was measured by using Park System XE-100 atomic force microscope with non-contact mode (to obtain precise morphology, exfoliated graphene was used). UV-Vis absorption spectra were recorded on a Varian Cary 5000 spectrophotometer with varying wavelengths from 200 nm to 800 nm. For UV-Vis absorption and sheet resistance measurement, Graphene was transferred on PET and SiO₂/Si substrates, and the same doping method was followed.

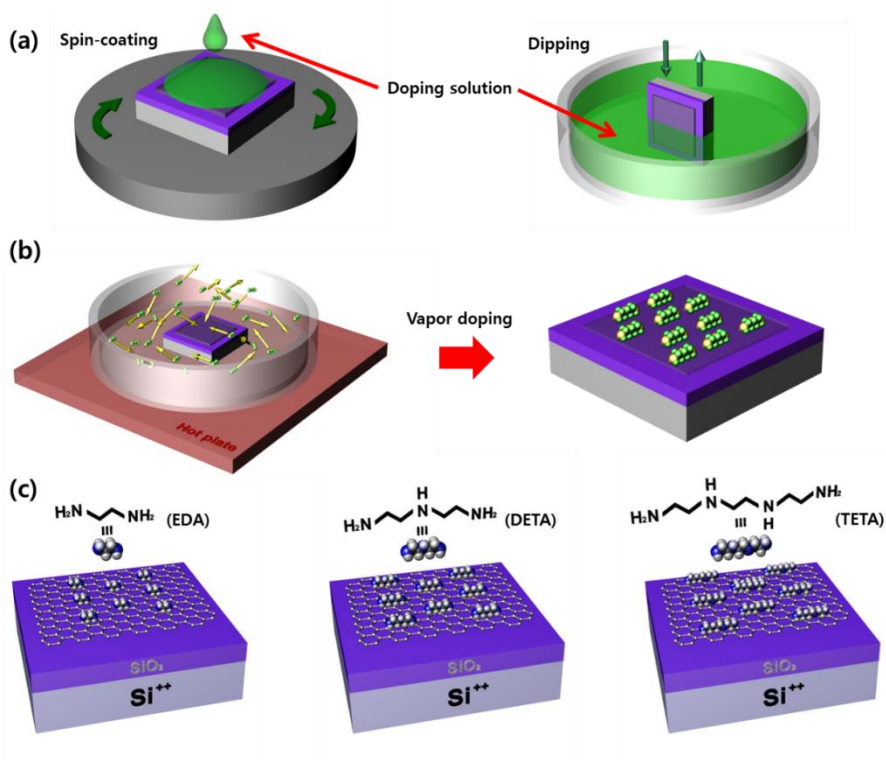


Figure 4.1. Schematic of doping process and dopants (a) Schematic process of spin-coating process (left) and dipping process (right) (b) Schematic process of evaporation doping. The molecules were evaporated by thermal heating using hot plate (left), then vapor doped graphene was obtained (right). (c) Schematic illustration of ethylene amines doped graphene field effect devices and molecular structure of EDA, DETA, and TETA.

4.3 Results and Discussion

The characteristics of n-doped graphene were studied by Raman spectroscopy at room temperature with 1mW 514nm-laser to minimize possible damage on graphene. Noticeable Raman peaks in graphene are the G band ($\sim 1584\text{ cm}^{-1}$) and the 2D band ($\sim 2700\text{ cm}^{-1}$) involving phonon frequencies near the Γ and K points in the Brillouine Zone.^[39] We characterized a pristine graphene and ethylene amine doped graphene samples to compare their Raman features. Figure 4.2a shows the representative Raman spectra of pristine graphene and doped graphene with EDA, DETA, and TETA.

The G band of graphene was upshifted from 1585.4 cm^{-1} (pristine) to 1590.4 cm^{-1} (EDA), 1593.5 cm^{-1} (DETA) and 1596.5 cm^{-1} (TETA), due to the effect of the Fermi level shift on the phonon frequencies induced by electron doping.^[53,115] In addition, the quality of graphene sample can be maintained after vapor doping process as confirmed by the low D peak (Figure 4.2a, inset) intensity related to defect density. As the number of amine groups in ethylene amine vapors increased (2, 3, and 4 for EDA, DETA, and TETA, respectively), the G peak positions were accordingly upshifted because the graphene became more intensely n-doped. On the contrary, the positions of the 2D peak were consistent regardless of doping (shown in Figure 4.2b). The different phenomena observed from the G peak and the 2D peak are mentioned in electrochemically gated graphene: The electron density can modify the 2D phonon (adiabatic effect), while the G phonon is affected by electron-phonon coupling (non-adiabatic effect).^[52] In other words, the position of the 2D peak is

predicted to decrease for an increasing electron concentration, whereas, the blue-shift of the G peak is observed due to electron-phonon coupling. Thus, the blue-shift of the 2D peak is expected for the strongly n-doped graphene, but it was not actually observed in the ethylene amine doped graphene. We suppose that the intermolecular interaction between adsorbed ethylene amine molecules and CVD graphene results in the abnormal shift of 2D peaks.

The intensity ratio of 2D to G peak is another important parameter to estimate the doping intensity.^[116] It was shown to decrease when the graphene was doped as shown in Figure 4.2c. Dozens of random points were measured to yield an average value, and the ratio of $I(2D)/I(G)$ decreased from 4.0 to 1.2 as a function of the G peak position from 1584 cm^{-1} to 1597 cm^{-1} . In Figure 4.2d, the full width at half-maximum (FWHM) values of the G band for pristine and doped graphene are shown. As the degree of doping intensified, the FWHM decreased due to the forbidden electron-hole pair arose from the Pauli exclusion principle.^[52,116] Based on these Raman features, we were able to confirm that graphene can be n-doped by ethylene amine vapors and the data showed a tendency that matches to the number of amine groups in the vapor dopants. In addition, the Raman features of doped graphene samples showed similar trends to the electric field induced tuning of the Dirac point of graphene – upshift of G band peak with decreasing $I(2D)/I(G)$ ratio as a function of doping concentration.^[39,52,53,115,116]

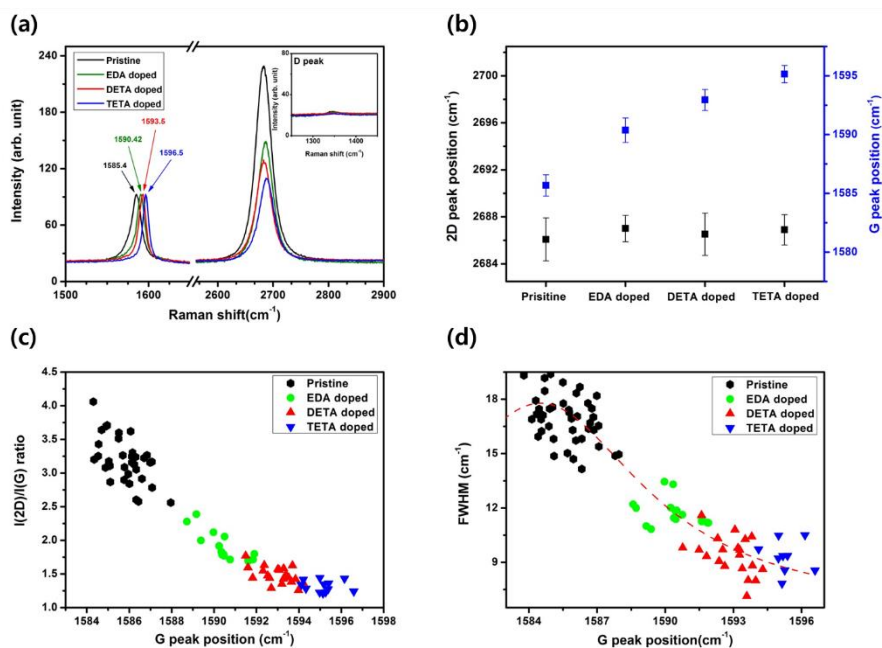


Figure 4.2. Characterization of Raman spectra of pristine, EDA, DETA, and TETA doped graphene (a) Representative Raman spectra of pristine, EDA, DETA, and TETA doped graphene (inset shows D peaks of Representative Raman spectra). (b) G and 2D peak position with pristine and various ethylene amines doped graphene. (c) Intensity ratio of 2D/G as a function of G peak position for each molecule doping. (d) FWHM of G peak as a function of G peak position with pristine and ethylene amines doped graphene (red line is fitted by Lorentzian curve).

To investigate and compare n-doping effects of ethylene amine vapors, the electrical properties of pristine and n-doped graphene transistors were measured. In Figure 4.3a, representative results of graphene field effect transistors for each molecule (EDA, DETA, and TETA) are displayed with different charge neutral points with respect to the vapors. The Dirac voltage of the pristine graphene transistor was initially measured, which was observed at 1.4 ± 2.3 V. The Dirac

voltages were shifted to -126.6 ± 5.8 V, -166.4 ± 1.8 V and -192.3 ± 5.8 V respectively for EDA, DETA, and TETA doped graphene (Figure 4.7).

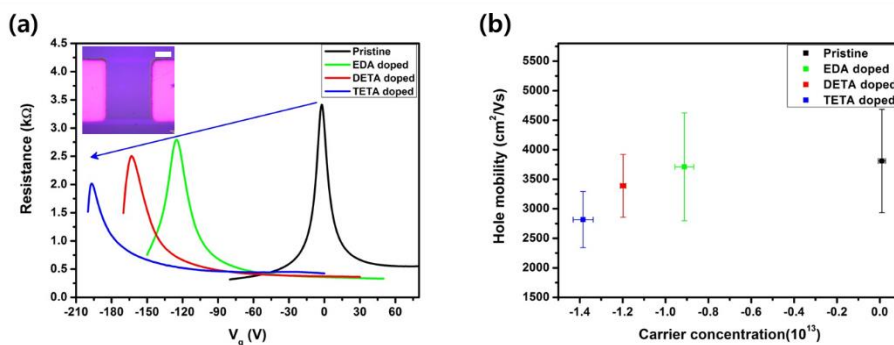


Figure 4.3. Electrical characteristic of the undoped and n-doped graphene FET devices. (a) Electrical characteristic of the FET devices of pristine (black), EDA-doped (green), DETA-doped (red), and TETA-doped (blue) graphene. The inset shows an optical image of the graphene FET. Scale bar, 50 μm . (b) The mobility of pristine, EDA-, DETA-, and TETA-doped graphene as a function of carrier concentration.

Graphene field effect devices showed relatively high mobility for their scales (approximately 200 μm scale, optical image provided in the inset of Figure 4.3a), which can be partially contained grain boundaries, ripples and small cracks in CVD graphene.^[117-119] More than 45 pristine graphene devices were measured, yielding 6219 ± 1288 $\text{cm}^2 \text{V}^{-1}\text{s}^{-1}$ (hole region) and 3809 ± 876 $\text{cm}^2 \text{V}^{-1}\text{s}^{-1}$ (electron region) without doping. For the doped graphene devices, we only compared the electron mobility due to the lack of hole-region points. After vapor doping, graphene devices showed decreasing electron mobility of 3711

$\pm 913 \text{ cm}^2 \text{ V}^{-1}\text{s}^{-1}$, $3388 \pm 531 \text{ cm}^2 \text{ V}^{-1}\text{s}^{-1}$ and $2817 \pm 475 \text{ cm}^2 \text{ V}^{-1}\text{s}^{-1}$ respectively for EDA, DETA, and TETA doped transistors. Such trend can be attributed to the potential difference between ethylene amines and pristine graphene; ethylene amines act as impurity charge sources on graphene channel.^[109] As shown in figure 4.3b, the results were plotted as a function of the carrier concentration, and the carrier concentration can be estimated according to the equation: $n = -\alpha(V_g - V_{CNP})$, with $\alpha = 7.2 \times 10^{10} \text{ cm}^{-2} \text{ V}^{-1}$,^{1,34} giving approximately $9 \times 10^{12}/\text{cm}^2$, $1.2 \times 10^{13}/\text{cm}^2$, and $1.4 \times 10^{13}/\text{cm}^2$ for respective dopants.

For comparison, the graphene films doped by dipping and spin-coating methods (Figure 4.1a) were characterized by FET measurements and optical imaging. The result shows that the graphene surface is irregularly covered with dopant molecules (Figure. 4.8). Therefore, the n-doping effect by dipping and spin-coating is much weaker or inhomogeneous (Figure. 4.9) compared to the vapor-phase doping that shows relatively uniform coverage of dopant molecules on graphene surface as shown in the AFM images (Figure. 4.10).

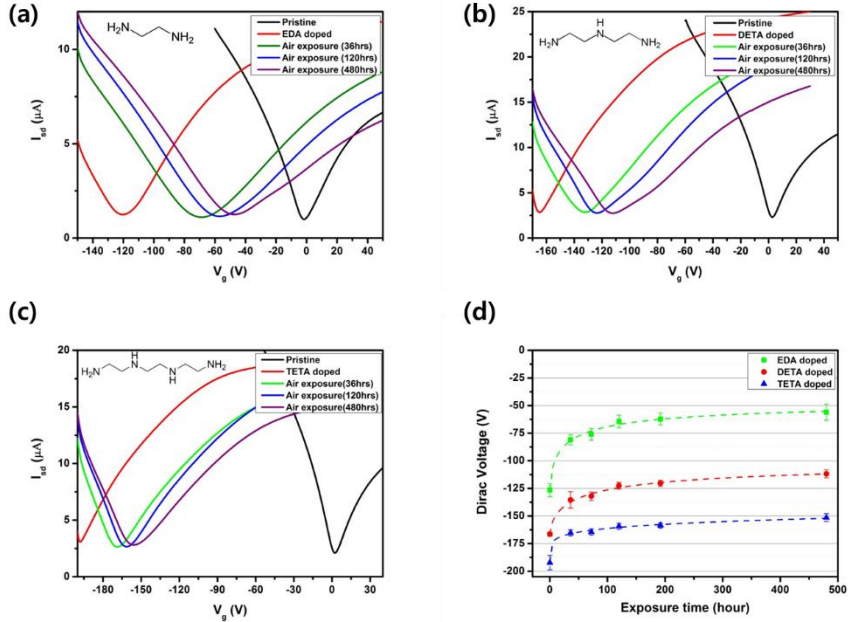


Figure 4.4. Dirac voltage shift as a function of air exposure time for each molecular doped graphene devices (a) EDA, (b) DETA, and (c) TETA. (d) Statistics of measured n-doped graphene devices.

Doping stability is another critical issue in fabricating n-doped graphene devices. Ethylene amine doped graphene transistors were studied by measuring the Dirac voltage as a function of the exposure time in the ambient condition for at least two weeks. For this study, CVD graphene films grown from a single batch were used to avoid inconsistencies in graphene devices and doping processes. As shown in Figure 4a-c, the charge neutral points of modified graphene devices doped with EDA, DETA, and TETA abruptly degraded after 36 hours of exposure to air. To compare the stability of doping for each vapor, graphene devices with EDA, DETA, and TETA vapors were all measured (shown in Figure 4.4d). The results of n-doping stability

based on the charge neutral points showed similar tendency in three types of devices (EDA, DETA, and TETA doped case) and charge neutral points were observed to start saturating after 36 hours of exposure in the ambient condition. After 20 days of exposure in the air, the charge neutral point of EDA doped graphene field effect transistors were changed from -126.6 ± 5.8 V to -56 ± 7.3 V, from -166.4 ± 1.8 V to -111.8 ± 3.6 V for DETA doped graphene and from -192.3 ± 5.8 V to -151.4 ± 3.5 V for TETA doped graphene compare to initially doped graphene. The major culprits for such dramatic doping reduction are inevitable evaporation of adsorbed molecules and the absorption of unwanted p-dopant gases on graphene in the ambient air. To check the influence by oxygen or water molecules in air, a pristine graphene FET was measured over 10 days in an ambient condition. We found that the p-doping effect of pristine graphene was saturated after 3 days, and the Dirac voltage was shifted by +30 V compared to as-prepared graphene (Figure. 4.11). In the case of the vapor-doped graphene, the p-doping by ambient air can be minimized as long as the graphene surface is covered with ethylene amine molecule, which would be advantageous for the long term stability of the strong n-doping effect.

The transmittance of n-doped graphene by ethylene amine vapors is slightly lower than the pristine graphene, because vapor-deposited ethylene amines initially form a lot of light-scattering aggregates on graphene surface.

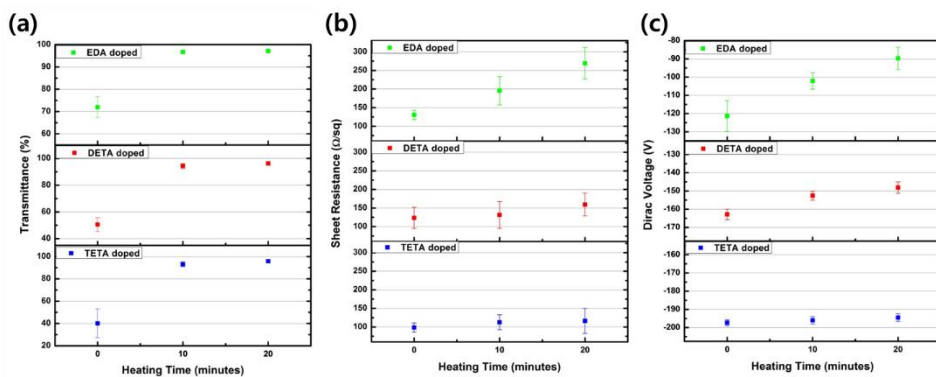


Figure 4.5. Changes in the transmittance at 550nm wavelength (a), sheet resistance (b), and Dirac voltage (c) of EDA-, DETA-, and TETA-doped graphene with increasing annealing time at 70 °C.

These ethylene amine aggregates can be easily removed by mild thermal heating for longer than 10mins at 70°C, which eliminates the haze problem and increases the optical transmittance. In addition, unlike EDA and DETA, TETA still has low vapor pressure at 70°C (Table 4.1) and interacts with graphene strongly enough to prevent evaporation, so we can obtain relatively stable sheet resistance and enhanced transmittance for the TETA doped graphene after thermal treatment (Figure 4.5 and Figure 4.12). This indicates that the stability of n-doping greatly depends on molecular weight and vapor pressure at given temperature, which needs to be carefully considered in the molecular doping of graphene. It should be also noted that the Dirac voltage change of the n-doped graphene well correlates with the sheet resistance change (Figure 4.5 and Figure 4.13), which can be utilized as a simple parameter to optimize the conductivity of graphene.

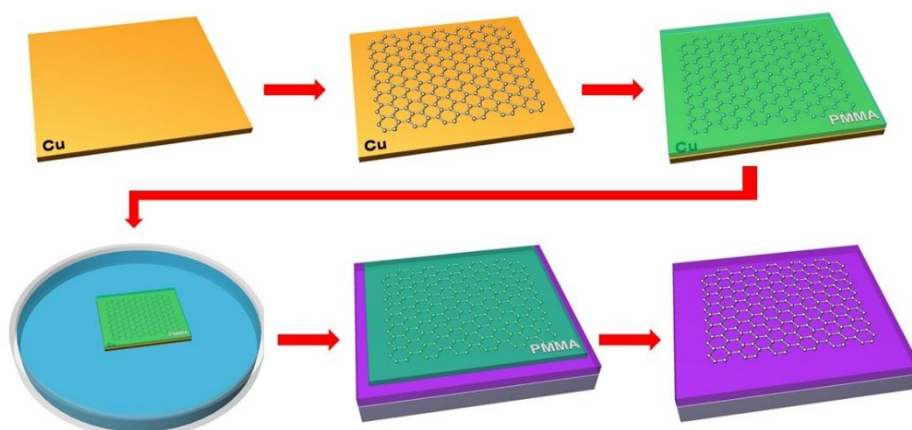


Figure 4.6. Schematic illustration of CVD graphene synthesis and transfer process.

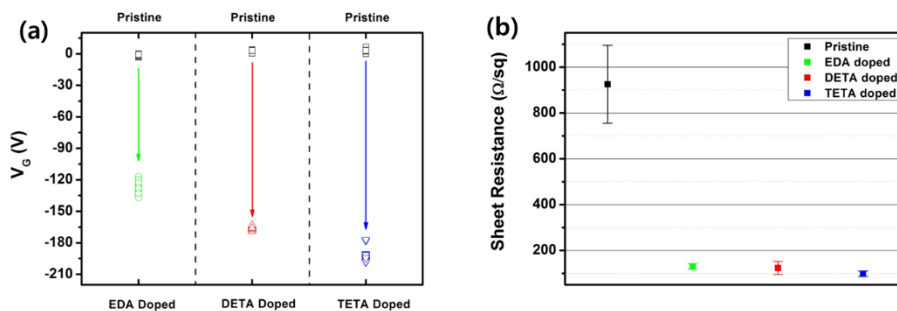


Figure 4.7. (a) Dirac voltage shift before and after doping with EDA (green), DETA (red) and TETA (blue) molecules. (b) Sheet resistance of pristine, EDA, DETA, and TETA doped graphene corresponding to (a).

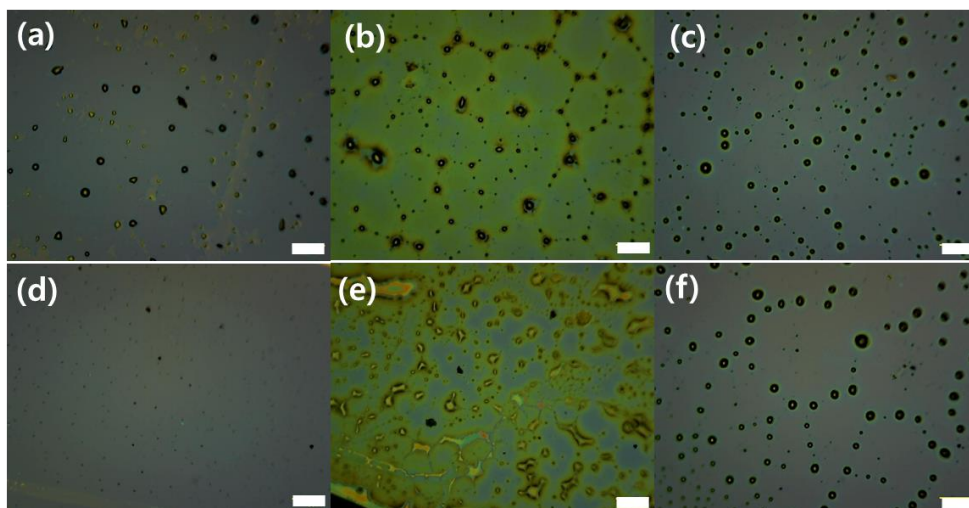


Figure 4.8. Optical images of graphene with various doping conditions. **(a-c)** Optical microscope images of graphene doped by dipping in 0.1 M solutions of EDA, DETA, and TETA, respectively. **(d-f)** Optical microscope images of graphene doped by spin-coating (3000 rpm) of EDA, DETA, and TETA solutions (0.1M), respectively. Scale bars, 100mm.

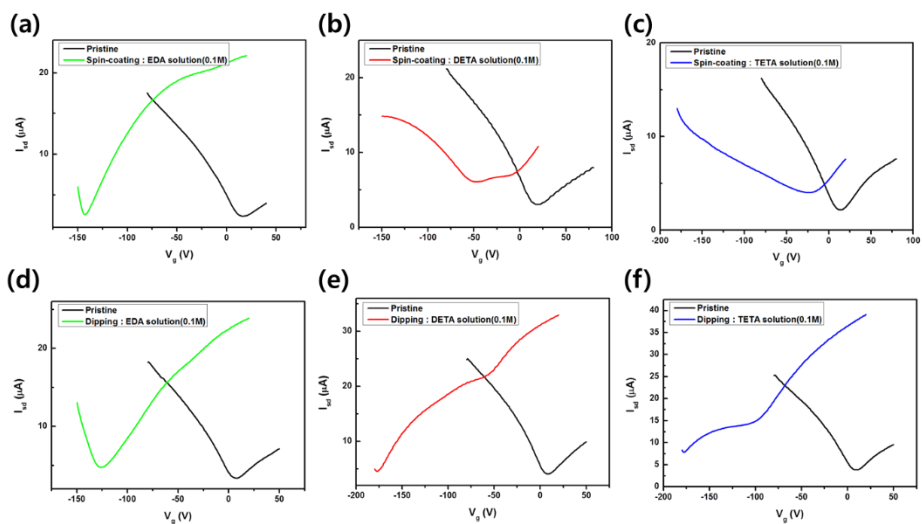


Figure 4.9. Dirac voltage shift of graphene FET with various doping conditions (**a-c**) Current vs gate voltage curves of graphene doped by dipping in 0.1 M solutions of EDA, DETA, and TETA, respectively. (**d-f**) Current vs gate voltage curves of graphene doped by spin-coating (3000 rpm) of EDA, DETA, and TETA solutions (0.1M), respectively.

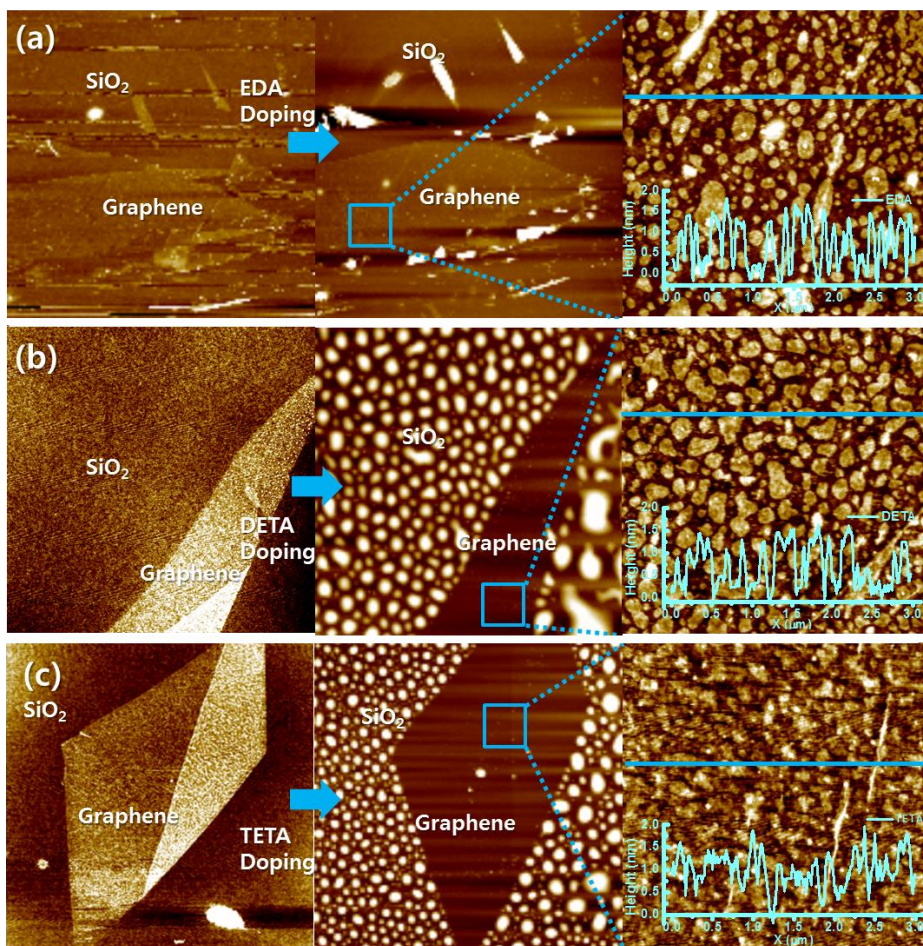


Figure 4.10. Atomic force microscope (AFM) images of exfoliated graphene on a SiO₂ substrate before and after doping for EDA (a), DETA (b), and TETA (c). Scan areas for the left 2 images, 20 μm × 20 μm, and for the right image, 3 μm × 3 μm.

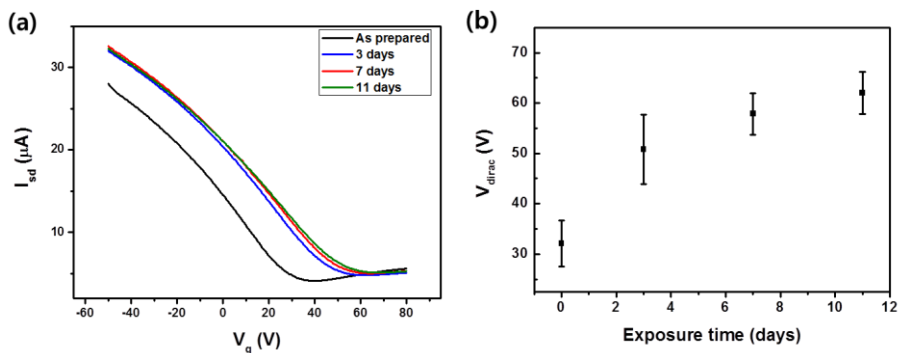


Figure 4.11. (a) Representative current vs. gate voltage curves for a pristine graphene device with respect to exposure time in air. (b) Dirac voltages of the 10 pristine graphene devices as a function of exposure time.

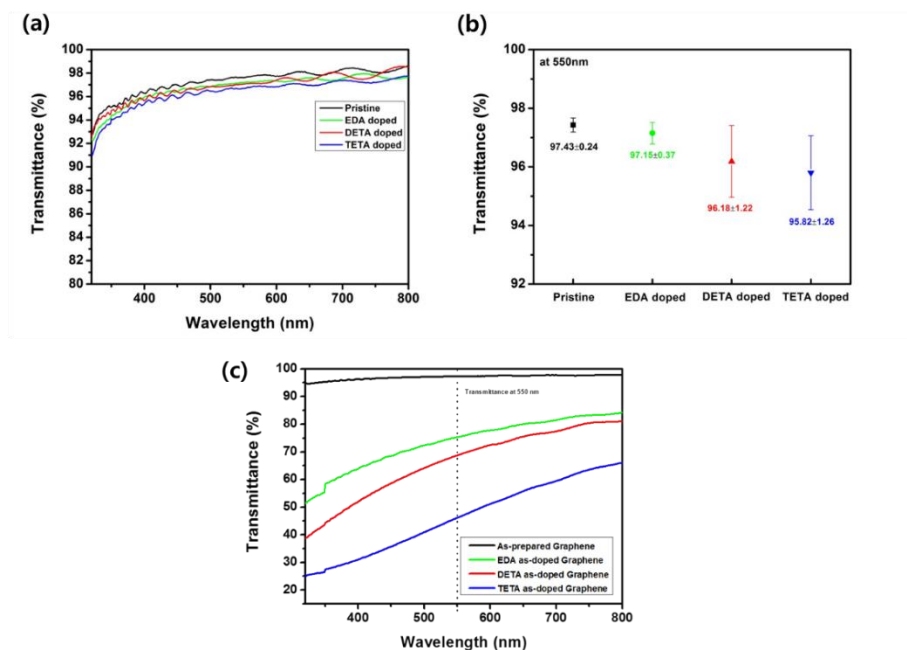


Figure 4.12. (a) Representative transmittance curve of each molecule-doped graphene depending on wavelength. (b) Optimized transmittance of each molecule-doped graphene after 20 minutes heating (at 550 nm wavelength). (c) Representative transmittance curves of as-prepared and n-doped graphene as a function of wavelength.

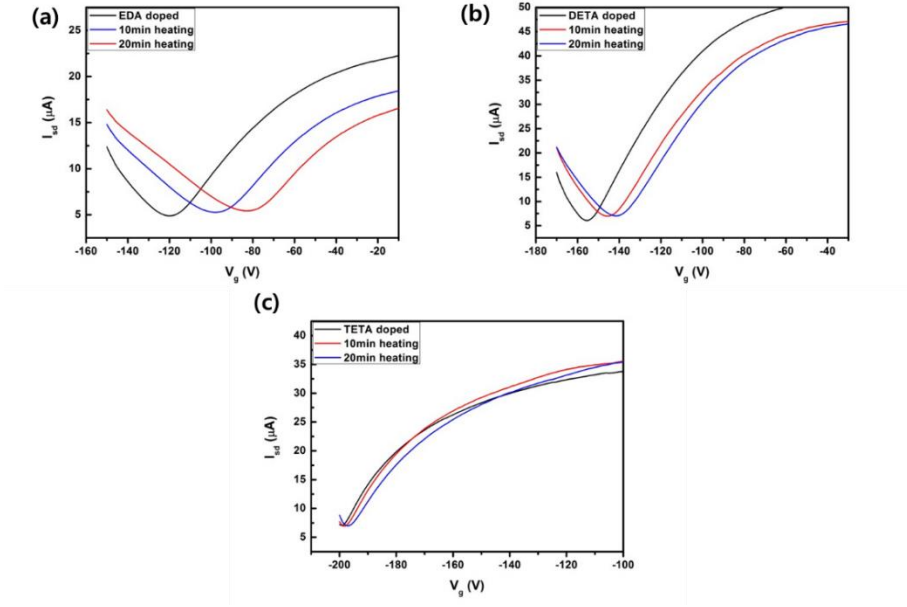


Figure 4.13. Representative current vs. gate voltage curves for EDA (a), DETA (b), and TETA (c) doped graphene devices with respect to heating time.

4.4 Summary

In summary, we demonstrated that graphene can be efficiently n-doped by ethylene amine vapors. The doping strength and stability depends on the number of electron-donating functional groups (-NH₂), molecular weight, and vapor pressure of the adsorbed molecules. In particular, the TETA-doped graphene shows very high carrier concentration ($1.4 \times 10^{13} \text{ cm}^{-2}$) as well as the lowest monolayer sheet resistance ($98 \pm 12 \text{ } \Omega/\text{sq}$) with excellent stability. We expect that the vapor-phase doping of molecular n-dopants will be able to solve the practical problems associated with the limited conductivity, durability, and safety issues of graphene films grown by CVD for further electronic applications.^[120-123]

Chapter 5 A Highly Conducting Graphene Film with Dual-Side Molecular n-Doping

5.1 Introduction

Graphene is an atom-thick material with honeycomb lattice structures consisting of sp^2 bonded carbons,^[1] which has been intensively studied owing to its fascinating 2-dimensional properties including flexibility,^[95] ultrahigh mobility,^[96] high transparency^[97] and outstanding heat dissipating ability^[98] useful for various electronic and optoelectronic applications.^[99] Among these properties, the electrical tunability based on its unusual band structure^[1] enables the optimization of the electrical conductivity and the work-function of graphene, which is important for various conducting electrode applications.^[22] Doping is one of the efficient methods to control the electrical properties of graphene, and several doping strategies have been devised, including substitutional doping,^[17,100] molecular adsorption,^[101,102,124,125] covalent functionalization,^[82,105,106,126] substrate surface modification^[80,100,107,126,127] and the use of metallic thin films or nanoparticles.^[110-112,128,133]

However, the doping strength of these doping method is limited by insufficient charge-transfer from dopants and by electron scattering from substituted atoms leading to low carrier mobility and conductivity. Previously, the chemical doping of graphene has been mainly carried out by coating graphene with dopants or transferring graphene on dopant layers. For example, self-

assembled monolayers (SAMs) have been utilized as ultrathin and uniform graphene-doping layers functionalized on an oxide surface,^[111,127] which is advantageous because of its simple fabrication process applicable to various surface and interface engineering.^[79,127,129,130] However, the SAM doping on a single-side of graphene did not provide enough doping strength to improve the electrical conductivity of graphene. As the amount of transferred charge is proportional to the surface area of graphene in contact with dopants, simultaneous doping on the dual-side of graphene would be more efficient to enhance the electrical properties of graphene. Here, we demonstrate a simple method to tune the electrical properties of graphene synthesized by chemical vapor deposition (CVD) with dual-side chemical doping – the bottom-side doping via substrate modification with NH₂-SAMs and the top-side doping with diethylenetriamine (DETA) molecules.

5.2 Experimental

Sample preparation

Highly P-doped Si substrate covered with 100 nm thickness of SiO₂ is used for electrical measurement of graphene field effect devices. Free-standing graphene on distilled water is carefully transferred on bare SiO₂/Si and NH₂-SAMs modified SiO₂/Si substrate respectively and PMMA is removed by using acetone. Cr (5 nm) and Au (30 nm) are deposited thermally for metal contact of 3-terminal graphene device with using pre-patterned stencil mask. Graphene channels are isolated with electron beam lithography technique. To avoid deviation in growth condition, we use same graphene sample grown in same bath. Each device has as large scales as 250 μm width and 50-250 μm length. Before doping the graphene film, thermal annealing is carried out at 300 °C for 1h with Ar and H₂ gas environment to remove PMMA residues and trapped water after graphene device fabrication process. For UV-Vis measurement and graphene heater, the same n-doping method was applied to a transparent substrate (glass). In case of graphene heater, 2 layer of graphene was used to obtain uniform heating.

Characterization

The n-type doping characteristics of graphene are defined by micro-Raman spectra using a 1mW, 514 nm Ar laser with a spot size of 2 μm (Renishaw inVia Raman microscope). The

transmittance was measured by Scinco s-3100 UV-Vis spectrometer. Four types of graphene-based field effect transistors are fabricated to measure the difference of the electrical performances. Agilent 2602 was used on 3-terminal geometry with source, drain and gate. Constant 10 mV voltage applied source to drain during the measurement and sweep range of gate voltage was -80 V to +70 V. The sheet resistance of graphene (0.2 mm × 0.2 mm square geometry) was measured using a four-point probe with a nanovoltmeter (Keithley 6221, 2182A) based on van der Pauw method considering

$$R_s = \frac{\pi V}{\ln 2 I}$$

where R_s is sheet resistance, V is applied voltage and I is current. The temperature responses of the heaters were measured by an infrared camera.⁴³

5.3 Results and Discussion

To investigate the electrical properties of the doped graphene, we prepared four different types of graphene field effect transistor samples – top-side, bottom-side and dual-side n-doped graphene and the pristine graphene. Figure 1 shows the schematic views of three types of n-doped graphene devices. To obtain the bottom-side n-doped graphene, NH₂-SAMs was constructed on the surface of SiO₂ (100 nm)/Si substrate by dipping in the aqueous solution of 3-aminopropyltriethoxysilane (volume ratio of 500:1) for 30 minutes. The NH₂-SAMs modified substrate was dried by blowing with nitrogen gun, followed by the careful transfer of graphene onto the substrate. Diethylenetriamine (DETA) was used as the top-side n-doping molecule, which exhibits strong n-doping effect.^[124] Vapor-phase DETA doping was carried out in the sealed petri-dish from the droplet on tissue under 70 °C baking on a hot plate for 30 minutes. Thus, the dual-side doping with DETA/NH₂-SAMs were completed as shown in Figure 1b, where the two types of dopants including the lone pair electrons of amine functional groups are efficiently positioned to maximize the electron doping effect on both sides of graphene.

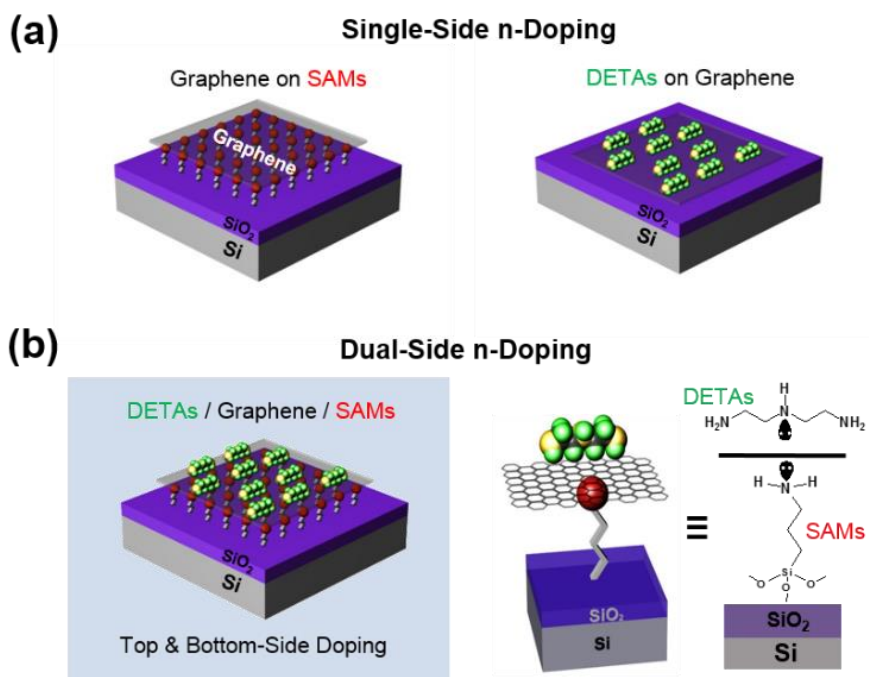


Figure 5.1. Schematic views of three different types of n-doped graphene. (a) Single-side doped graphene: Top-side n-doping (left) with evaporated DETA molecules and bottom-side n-doping (right) with amine-functionalized SAMs. (b) Dual-side doped graphene (left) and graphical representation of the molecular structure of the dopants on the both sides of graphene (right).

Figure 5.2a shows the Raman spectra of the pristine, single-side, and dual-side doped graphene with NH_2 -SAMs and DETA. The G band of graphene were up-shifted from 1585 cm^{-1} (pristine) to 1588 cm^{-1} (NH_2 -SAMs modified) and 1590 cm^{-1} (DETA doped) and 1600 cm^{-1} (DETA/ NH_2 -SAMs modified) due to the effect of the Fermi level shift on the phonon frequencies as a result of electron doping.^[52]

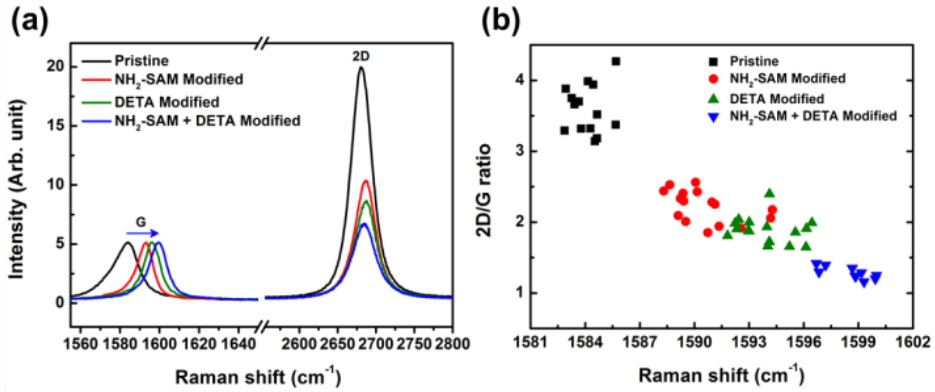


Figure 5.2. (a) The representative Raman spectra of graphene with different dopants (pristine, NH₂-SAMs, DETA and DETA/NH₂-SAMs). (b) Raman shift vs. I(2D)/I(G) ratio plot of pristine, NH₂-SAMs modified, DETA doped, and dual-side modified (DETA/NH₂-SAMs) graphene

Noticeably, the intensity ratio of I(2D)/I(G) was also decreased from 3.6 ± 0.3 to 2.2 ± 0.2 for the DETA doped graphene, 1.9 ± 0.2 for the NH₂-SAMs doped graphene, and 1.3 ± 0.1 for dual-side modified graphene (Figure 5.2b) with the up-shift of G band when chemical doping was applied. This blue shift of G band and the decreased ratio of I(2D)/I(G) exhibit characteristics of typical electron doping of graphene, which has been shown in previous reports.^[52,116,131] Therefore, we confirmed that our doping process successfully induced strong n-doping of graphene.

In Figure 5.3b, the graphene field effect transistors show different charge neutral points with respect to different doping conditions (schematic shown in Figure 5.3a). Initially, the charge neutral point (V_{CNP}) of pristine graphene transistors starting at 2 V was negatively changed to -40 V in the bottom-side doped

graphene device with NH₂-SAMs. The point was shifted more down to -68 V in the dual-side doped graphene devices modified with DETA/NH₂-SAMs on the both sides of graphene films. The charge neutral point of graphene devices was also shifted to -48 V after top-side doping with DETA (Figure 5.3c). The mobility of graphene devices can be extracted from the following equation:

$$\mu = \frac{1}{C_i} \frac{d\sigma}{dV_G}$$

where C_i is capacitance of 100 nm SiO₂ ($3.24 \times 10^{-8} \text{ F}\cdot\text{cm}^{-2}$), σ is conductivity of graphene, and V_G is applied gate voltage.

Graphene field effect devices show relatively high mobility considering its scales (length: 50-250 μm , width: 250 μm) although the graphene channels possibly include some defects such as grain boundaries, ripples and small cracks.^[117,118] While the pristine graphene device shows 2791 $\text{cm}^2\text{V}^{-1}\text{s}^{-1}$ for hole region and 2125 $\text{cm}^2\text{V}^{-1}\text{s}^{-1}$ for electron region, the NH₂-SAM modified graphene devices show 1660 $\text{cm}^2\text{V}^{-1}\text{s}^{-1}$ for electron region and 751 $\text{cm}^2\text{V}^{-1}\text{s}^{-1}$ for hole region. Such discordant tendency between the electron and hole mobility of the NH₂-SAM device was mainly caused by misalignment between electrodes and graphene channels in terms of work-function.^[85] It is supposed that the suppression in mobility is originated from inhomogeneous coverage of NH₂-SAMs, leading to charge impurities on graphene channels.^[101]

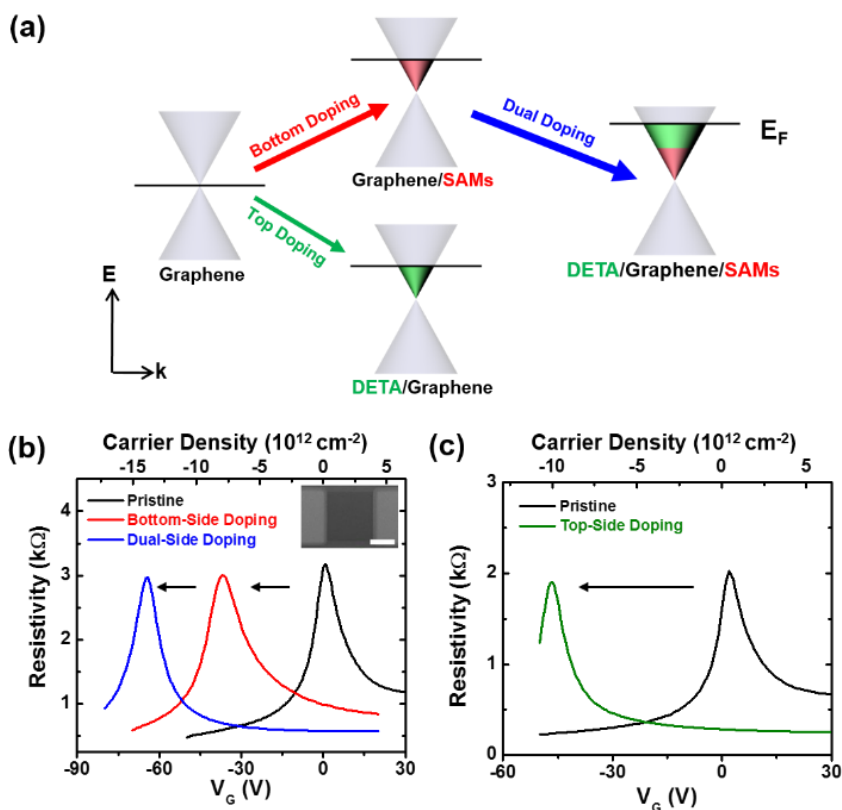


Figure 5.3. Schematic illustration of doping process and graphene FET characteristic of pristine and doped graphene (a) Schematic illustration of Fermi energy level (E_f) diagram of different types of n-doped graphene. All the doping processes (bottom-side, top-side and dual-side n-doping) induce significant up-shift of E_f , in particular, dual-side n-doped graphene has much stronger n-type behavior from the molecular n-doping of bottom-side and top-side. (b) Current – gate voltage transfer characteristic of the graphene FETs on pristine, bottom-side, and dual-side doped graphene. The inset shows the SEM image of graphene FETs with 100 μ m scale bar. (c) Current – gate voltage transfer characteristic of the graphene FETs with pristine and DETA doped graphene.

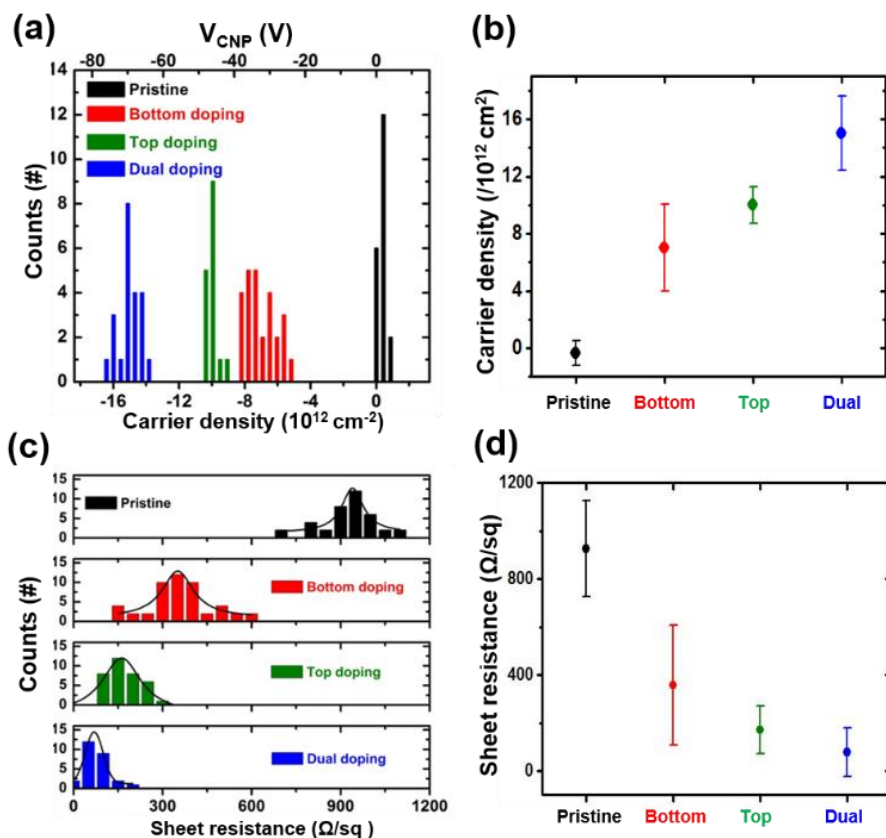


Figure 5.4. Electrical properties of pristine graphene and doped by NH_2 -SAMs, DETA and DETA/ NH_2 -SAMs (dual-side doped) (a) Histogram of charge neutral points of graphene FETs doped by NH_2 -SAMs, DETA and DETA/ NH_2 -SAMs (dual-side doped). (b) Averages and distributions of carrier density plot of four different types of graphene FETs. (c) Histogram of sheet resistance of graphene doped by NH_2 -SAMs, DETA and DETA/ NH_2 -SAMs (dual-side doped). (d) Averages and distributions of sheet resistance plot of four different types of graphene FETs.

However, after applying DETA on the top-side of NH₂-modified graphene device, its hole and electron mobility changed to 1775 cm²V⁻¹s⁻¹ and 1808 cm²V⁻¹s⁻¹, respectively. These increased mobility can be explained by the screening effect of charged impurities.^[94,132] The top-side doped device with DETA showed 2598 cm²V⁻¹s⁻¹ and 2426 cm²V⁻¹s⁻¹ for hole and electron regions, respectively. In Figure 3c, the schematic diagram represents the tuning of the Fermi level by the chemical doping process. Both bottom-side doping with NH₂-SAM and top-side doping with DETA induced the up-shift of the Fermi level in the case of intrinsic graphene. Interestingly, the dual-side doping resulted in further increased Fermi level, showing much stronger n-doping effect than single-side doping.

To confirm the average molecular doping effect at room temperature, dozens of graphene field effect transistors were measured. The results are plotted as a function of carrier density and charge neutral point in figure 5.4a-b. Carrier density is estimated by a typical equation, $n = -\alpha(V_G - V_{CNP})$, with $\alpha = 2.16 \times 10^{11} \text{cm}^{-2}\text{V}^{-1}$. We found that the carrier density of graphene was tunable up to $-1.7 \times 10^{13} \text{cm}^{-2}$ by using dual-side doping, which is the highest value among the recent reports on n-doping of graphene.^[79,80,112] To further examine the doping characteristics induced by each dopant, we also measured the sheet resistance of pristine and doped graphene on SiO₂ (100 nm)/Si substrates. The results from more than 30 different positions of graphene are shown in figure 5.4c-d. The sheet resistance of graphene

gradually decreased from $923 \pm 148 \text{ } \Omega/\text{sq}$, $385 \pm 140 \text{ } \Omega/\text{sq}$, $150 \pm 77 \text{ } \Omega/\text{sq}$ and to $86 \pm 39 \text{ } \Omega/\text{sq}$, respectively for pristine, NH_2 -SAMs, DETA, and dual-side doped graphene. These results well correspond to the shifts of charge neutral points in the graphene field effect devices, implying that the charge transfer between molecules and graphene can be maximized by increasing the surface area of graphene in contact with n-dopants. The transmittance of dual-side doped graphene measured at 550 nm wavelength is $\sim 96\%$ (Figure 5.6).

To demonstrate the doping stability, we measured the sheet resistance of the dual-side n-doped graphene after air exposure, thermal heating, and light exposure. The results show that the average sheet resistance was increased by $\sim 20\%$ after 60 min air exposure. After 15 min heating at $70 \text{ } ^\circ\text{C}$ and $100 \text{ } ^\circ\text{C}$, the sheet resistance was increased to 150 and 350 Ohm/sq, respectively (see details in figure 5.7). In addition, the FET characteristics of DETA-doped graphene with respect to doping time and temperature was also examined (Figure 5.8).

Finally, we fabricated transparent heaters based on the n-doped graphene. Figure 5 depicts the time-dependent temperature profiles of the graphene-based heaters treated with different dopants. As previously reported, the steady state temperature of the heater depends on the sheet resistance of graphene films.^[31] As a result, the dual-side doped graphene heater exhibits the heating temperature as high as $54 \text{ } ^\circ\text{C}$, while single-side doped and pristine

graphene heater show $\sim 51^\circ\text{C}$ and $\sim 40^\circ\text{C}$, respectively (Figure 5.9).

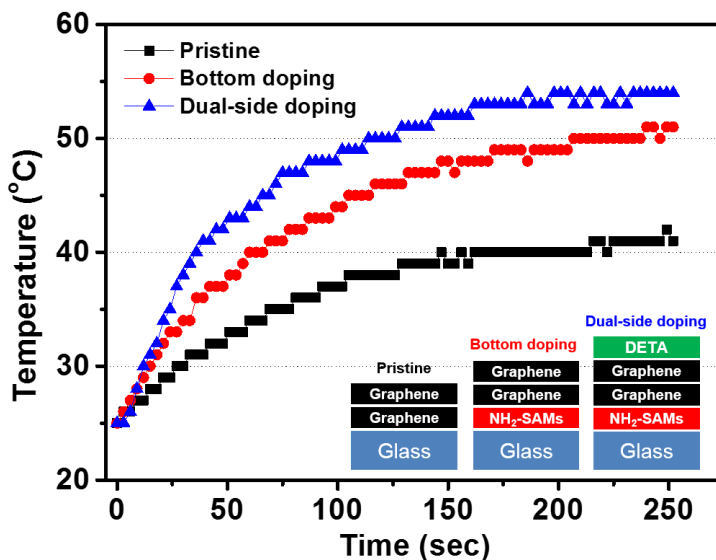


Figure 5.5. The temperature profiles of pristine, bottom doped and dual-side doped graphene heaters. The size of the heaters was $1.8 \times 1.8 \text{ cm}^2$. The temperature responses of the heaters were monitored every three seconds by an infrared camera. The 20 V of input voltage was supplied to the heaters through two-terminal side copper electrodes.

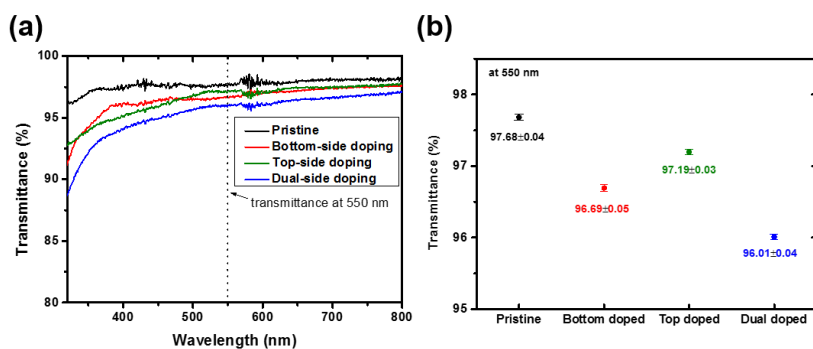


Figure 5.6. (a) Representative UV-Vis spectra of top, bottom and dual-side doped graphene film (b) Transmittance of pristine, top-side doped, bottom-side doped and dual-side doped graphene.

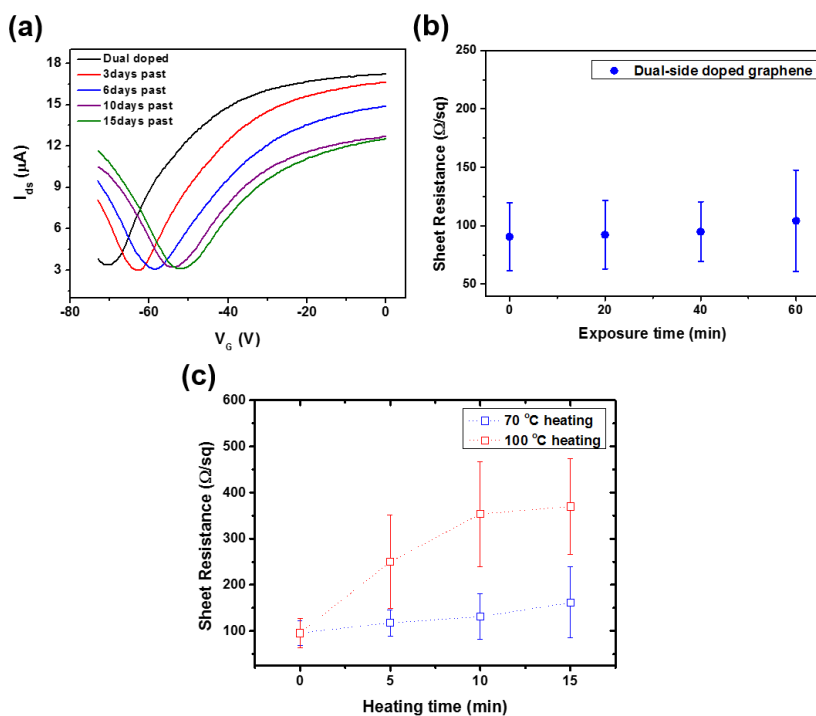


Figure 5.7. (a) The Dirac voltage shift of dual-side doped graphene as a function of exposure time in the ambient condition at room temperature (b) Light stability of dual-side doped graphene with respect to exposure time (100

W light bulb was used as a light source). (c) Thermal stability of dual-side doped graphene with heating time under 70 °C (blue) and 100 °C (red).

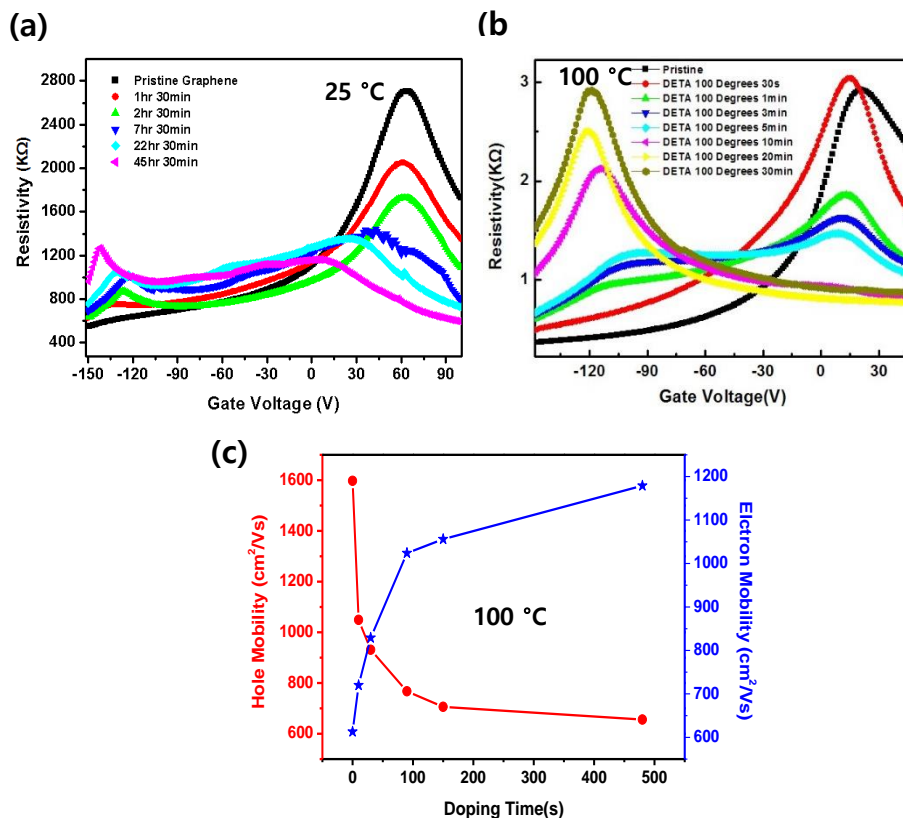


Figure 5.8. FET characteristics of DETA-doped graphene with respect to doping time and temperature. (a, b) Change in Dirac curves with respect to doping time at 25 °C and 100 °C, respectively. (c) Change in electron and hole mobility with respect to doping time at 100 °C.

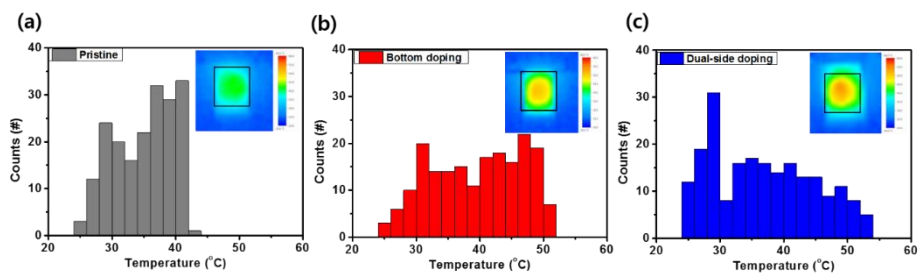


Figure 5.9. Statistical analysis of temperature distribution in the graphene-based heaters. **(a)** a pristine graphene-based heater, **(b)** a bottom doped graphene-based heater, and **(c)** a dual-side doped graphene heater. The insets show the corresponding infrared images at the steady state temperature at 20V.

5.4 Summary

In conclusion, we have developed a simple and efficient dual-side molecular doping method for graphene, demonstrating effective work function modulation, high carrier density ($-1.7 \times 10^{13} \text{ cm}^{-2}$) and significant reduction of sheet resistance ($86 \pm 39 \text{ } \Omega/\text{sq}$), which is believed to be the best conductivity for large-area CVD graphene so far. The actual performance of the dual-side doped graphene film was confirmed by fabricating a transparent heater that exhibits higher heating temperature compared to single-side doped or undoped graphene films. We expect that further efforts to optimize the dual-side doping method would enable wide variety of practical application of graphene films that require low sheet resistance comparable to indium tin oxide (ITO) as well as high transparency and flexibility useful for flexible electronics in the future.^[21,31,99,124,127,133]

Chapter 6 Graphene Field Effect Transistors Modified by Self-Assembled Monolayers

6.1 Introduction

Graphene has been a main subject of many researches in recent years due to high carrier mobility and tunability of transport characteristics for device applications. ^[70,71,73] Up to date, various approaches for the development of graphene based electronics have been applied to control the carrier type and density in graphene by means of electrical doping using gate voltage, ^[134-136] chemical doping, ^[137,138] and metal deposition. ^[139,140]

In particular, controlling the intrinsic doping and the local carrier density is one of subjects that require attention. So far it has been achieved with reactive molecular adsorbates ^[10,101] and top gates have been used to control the carrier density in selected area. However, molecules in the atmosphere also dope graphene, ^[101,137] which makes implementation in device technology be difficult, as well as the tuning capability of a top-gate p-n junction leads to reduce the sample quality due to the top-gate oxide. Thus, a new technique to solve the problem is required to improve the electrical properties of the graphene-based electronic devices.

A Self-assembled monolayers (SAMs) have been focused as a useful mean to make an ultrathin layer uniformly constructed on an oxide surface because SAMs are easily formed by the chemisorptions of hydrophilic head groups on a substrate packed closely to each other by van der Waals interactions ^[129,141] (Figure 6.1 b). In addition, the

fabrication process of SAMs is very simple, which makes SAMs technologically attractive for surface and interface engineering.

[80,130,142]

In this study, we fabricated n-doped graphene FET. Graphene was modified by solution-based chemical doping with amine-SAMs method which has effects on the surface energy, dipole moment, and chemical reactivity of ultrathin layer at designated area easily tuned by functional groups.^[143,145] In addition, the relative value of the Fermi energy to the local charge neutrality point is defined as saturated Fermi energy depending on temperature.^[144] The doping effect and the temperature dependence by SAMs was measured by the current vs. gate voltage curves. Additionally, in order to study our doping effect on applications, graphene p-n junction devices were also fabricated with locally tuned through amine-SAMs, which caused similar results from graphene p-n junction devices.

6.2 Experimental

Fabrication of p-n junction graphene devices.

In order to investigate the electronic properties, we fabricated a back-gate graphene transistor, as shown in Figure 1. Cr/Au metal used as drain and source is thermally deposited on the selected area on highly B-doped Si with 300 nm thickness of SiO₂. We employed NH₂-SAMs (diaminosilane:DI water = 1:1000) on the FET by the solution method. Then, wet etched monolayer CVD graphene was transferred on the NH₂-SAMs adsorbed on the FET substrate.

For a graphene p-n junction, e-beam resist was spin-coated on SiO₂/Si substrate whereas the uncovered parts can be exposed to dopant-NH₂ for n-doping via dipping into the solution of NH₂-SAMs (diaminosilane:DI water = 1:1000). PMMA remained on uncovered doping region was erased in acetone and subsequently, the device was sonicated in ethanol for 30 min to remove additional unbound NH₂ molecules. Wet etched monolayer CVD graphene was transferred on SiO₂/Si substrate and source, drain, and probes electrodes were also deposited for a metal contact. The size of each device is 18 x 6 μm².

Measurements.

Raman spectroscopic imaging technique was employed to characterize the graphene p-n junction. The excitation source is 514 nm laser with a laser power below 0.1 mW on the sample to avoid laser induced heating. A objective lens with NA = 2 μm was used in the Raman experiments. The spot size of the laser was estimated to be 2 μm

as an excitation source. The laser beam was focused by a 500 × objective on the sample keeping the output power 100 mW.

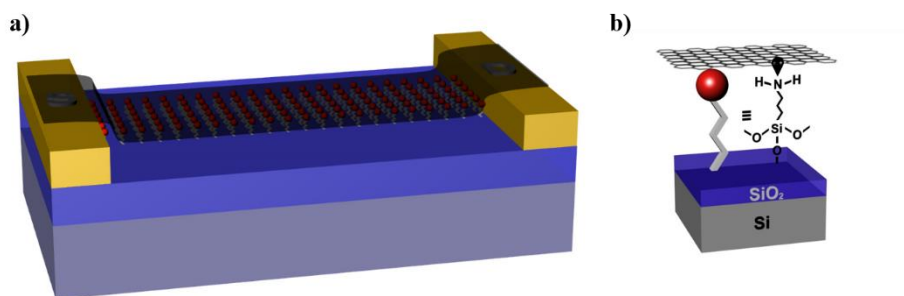


Figure 6.1 Schematic of a) NH₂-SAMs modified graphene FET and b) chemical structure of NH₂-SAMs

6.3 Results and Discussion

The electrical measurements were performed in Helium closed loop cryostats capable of $T = 5-310$ K. Figure 6.2 shows the resistivity (ρ) as a function of V_{BG} and T of the graphene FETs. The graphene FET displays intrinsic n-type behavior from the charged neutral point at the -54 V at room temperature, indicating n-doping in graphene. It implies that graphene on SAMs-modified SiO₂ substrate can be doped by the charge transfer process from lone pair electrons of NH₂- or built-in electric field due to molecular dipoles from the functional group (NH₂-) in SAMs, which leads to graphene to be n-doped in contact with the functional group.^[145] In fact, a remarkable feature in the range from room temperature to 200 K is the strong T -dependence of the charged neutral point. The Dirac points were shifted to positive voltage direction until 200 K. The similar tendency is also observed in mobility (Figure 6.3b). Not only is the mobility of n-doped graphene gradually increased with decreasing T and it comes to 9,000 cm²V⁻¹s⁻¹ at 200 K, but also the V_{CNP} is also diminishing until ~ 22 V (Figure 6.3a, 6.2a), sheet resistance also extracted from graphene FET data shows similar tendency (Figure 6.2b). This implies that charged impurities between graphene and NH₂- SAMs interface are decreased proportional to temperature up to 200 K. We attribute this phenomenon to the substrate-induced random potential fluctuations introducing electron-hole puddles^[146-148] close to the Dirac point that causes spatial fluctuations in doping levels. The effect of random potential can be estimated from a saturation density n^{sat} used to estimate an energy bandwidth, E_F^{SAT} . Figure 6.3c indicates the comparison of carrier

density dependence of conductivity at T ; 5 K and 300 K. The arrows present the carrier density below which transport properties are dominated by potential fluctuations. From high T to 200 K, the slope of E_F^{SAT} curve approach 50 meV whereas at below 200 K, the curve saturated. The amount of charged impurities can be extracted from the slope of impurity carrier concentration with conductivity which is reduced with decreasing T as shown in Figure 6.3d. The distribution of V_{CNP} for a dozen of samples we fabricated exhibits the charge neutral points between -55 V and -15 V as a result of the high levels of doping on the surface as shown in Figure 6.2c. The SAMs doped graphene device can be further manifested by the following Quantum Hall effect at 5K and under 8T magnetic field. With the use of a Hall-bar-type electrode configuration, the magnetoresistance R_{xx} and Hall resistance, σ_{xy} are measured. From Figure 6.2d, Quantized plateaus are well quantized in parallel and vertical direction in a hole region. However, plateaus of electron region do not well quantize. From the results, we believe that the electron region can be affected by the SAMs not uniformly constructed on SiO_2/Si substrate. For comparison of surface induced temperature dependence of SAMs modified graphene, we used SiO_2 and Octadecyltrichlorosilane (ODTS) as a substrate. The result of SiO_2 and ODTS shows different temperature dependence, which is different from NH_2 modified SAMs. We assumed that ODTS-SAMs can be rotated or folded ^[191] during changing the temperature from 175 K to 250 K, which caused the changing the random potential density in graphene. While, amine functional groups in NH_2 -SAMs donate electrons to graphene at room temperature due to thermal

energy whereas the effect of NH₂-SAMs is frozen out below ~ 200 K. The mobility and the Dirac point are strongly dependent on temperature and charged impurities originated from NH₂-SAMs. We believe that doping effect of NH₂-SAMs is affected by both charged impurities and dipoles, whereas below 200 K, molecular dipole can mainly play a role in doping. Here, further studies are needed to determine the precise cause of the saturated mobility and charge neutral point at < 200 K.

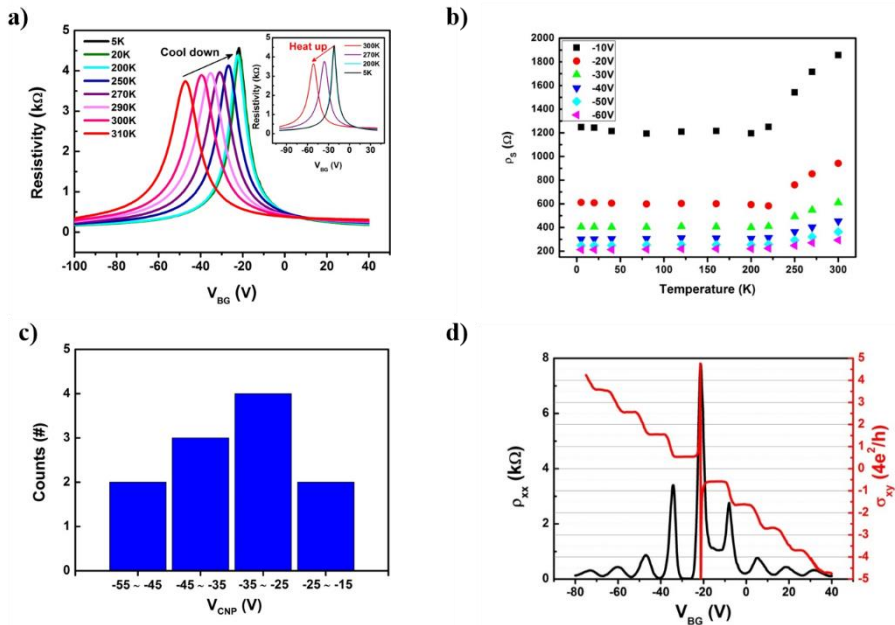


Figure. 6.2. Electrical properties of chemical modified graphene devices. (a) The ρ - V_g curves (inset shows same device was measured from 5K to 300K) (b) Sheet Resistance as a function of temperature (c) Distribution of V_{CNP} for all the samples at room temperature (d) Longitudinal resistivity (red) and Hall conductivity (black) as a function of gate voltage at fixed magnetic field $B = 8.9$ T, measured at 4 K.

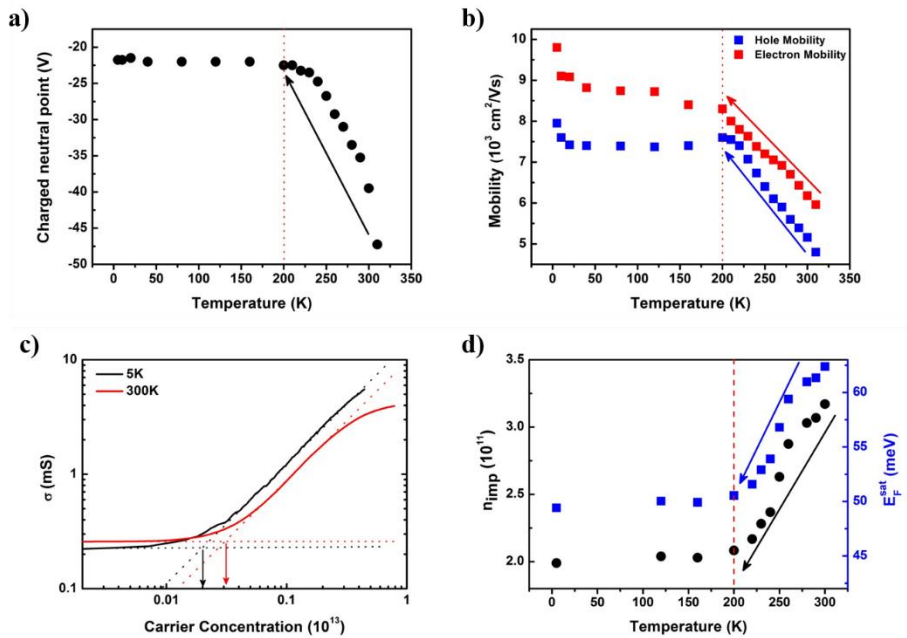


Figure 6.3 a) Dirac point and b) electron/hole mobility of amine modified graphene as a function of applied temperature c) Comparison of the impurity carrier concentration vs. conductivity for n-doped samples at 5 K (black line) and 300 K (red line). The arrows indicate that charged impurity concentration. d) Temperature dependence of charged impurity and its saturation Fermi energy.

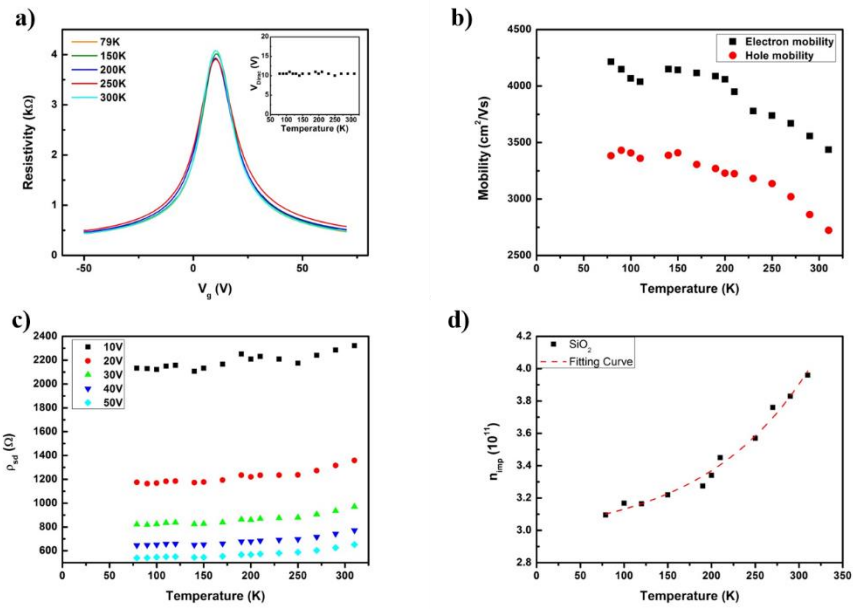


Figure. 6.4 a) The ρ - V_g curves (inset shows Dirac voltage as a function of temperature). b) Temperature dependence with mobility of pristine graphene FET on SiO_2 substrate. c) Temperature dependence of resistivity of pristine graphene FET on SiO_2 as a function of gate voltage. d) charged impurity of graphene on SiO_2 as a function of temperature

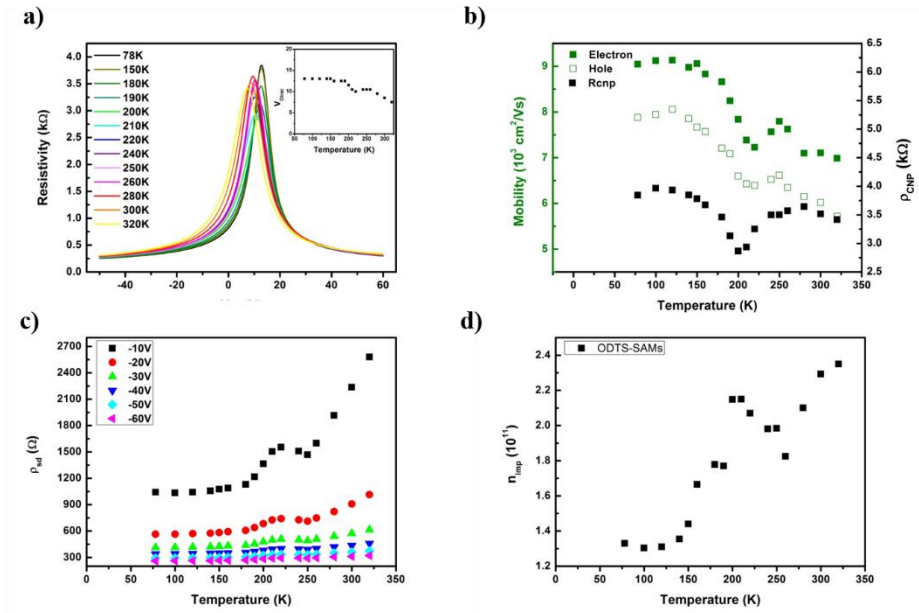


Figure. 6.5 a) The ρ - V_g curves (inset shows Dirac voltage as a function of temperature). b) Temperature dependence with mobility of pristine graphene FET on ODTS-SAMs substrate. c) Temperature dependence of resistivity of pristine graphene FET on ODTS-SAMs as a function of gate voltage. d) charged impurity of graphene on ODTS-SAMs as a function of temperature

Next, the electrical transport in the p-n junction device is prepared to further investigate on the application of n-doping graphene *via* amine-SAMs. The process of p-n junction graphene device is described in Figure. 6.6. Shown in Figure 6.7a is an optical image of a partially modified p-n device. The selective region marked with red of the inset is patterned by e-beam lithography and NH_2 -SAMs are constructed by dipping into the solution. In four-terminal measurement, lock-in amplifier (STS SR830) was used with 10 nA current flow in p-n junction device and both p type and n type graphene region were measured, respectively. In Figure 6.7b, red dot line presents n-region

from measurement between electrode 1 and 2, whereas blue dot line presents p-region from electrode 3 and 4. For a p-n junction, electrode 1 through 4 was connected, indicating the charged neutral points of each region can be detected at -37 V (n-region) and +23 V (p-region) respectively. The mobility of graphene devices is derived from using the equation

$$\mu = \frac{L}{WC_i V_{sd}} (\Delta I_{sd} / \Delta V_G) \quad (1)$$

where $C_i = 1.08 \times 10^{-8} \text{ F cm}^{-2}$, $L = 9 \mu\text{m}$, $W = 1 \mu\text{m}$, and $V_{sd} = 1 \text{ V}$. CVD-grown graphene shows as high mobility as $5000 \text{ cm}^2\text{V}^{-1}\text{s}^{-1}$ (n-type) and $4000 \text{ cm}^2\text{V}^{-1}\text{s}^{-1}$ (p-type) at room temperature. Charged neutral points observed at -40 V (n-type) and +25 V (p-type), respectively (Figure 6.7b), indicating the two peak positions are well matched to the transport curve of charged neutral points in both p, n-type region though p-n junction graphene devices. The high carrier mobility of CVD graphene demonstrates a well-controlled surface condition as a consequence of the doping treatment with NH_2 -SAMs.

To further study T -dependent transport of the p-n junction device, the electrical measurements were performed in the same T -conditions for n-doping device. The n-type peaks shifted to positive voltage with decreasing T are confirmed in the resistivity as a function of gate voltage curves, whereas p-type peaks are rarely moved, as shown in Figure 6.4(c). Moreover, the charged neutral point of n-type region is shifted to positive region with decreasing T , but the point saturates below $\sim 200 \text{ K}$, which matches with the curve of charged neutral point

by NH₂-SAMs (Figure 6.7d). This result reminds us to consider the previous experiment, n-doping FET, due to the similar consequence. Measured p-n junction graphene device is also confirmed by Raman spectroscopy. Raman maps of G and 2D bands were obtained to analyze the selective area doping behavior of the graphene p-n junction device. An optical image of p-n junction device for four probe measurement is shown in Figure 6.8a and B region of the red spot is doped with NH₂-SAMs. From the Figure 6.8b, the G-band of NH₂-SAMs modified area exhibits a bright color and a blue shift from 1584 to 1592 cm⁻¹, whereas the intensity of 2D-band is substantially decreased as shown in Figure 6.8d. The Raman spectra show main features in the range from 1000 to 3000. The changes of peak positions and the decreased ratio between the peaks intensity, I(2D)/I(G) ratio indicate the selected area of p-n junction device is effectively doped by NH₂-SAMs, as shown in Figure 6.8c.

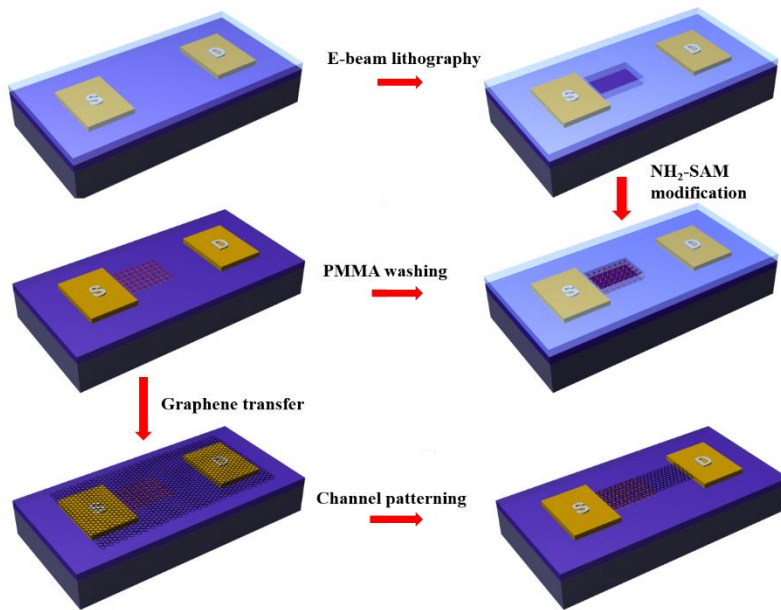


Figure. 6.6. A schematic view of fabrication process of graphene p-n junction device.

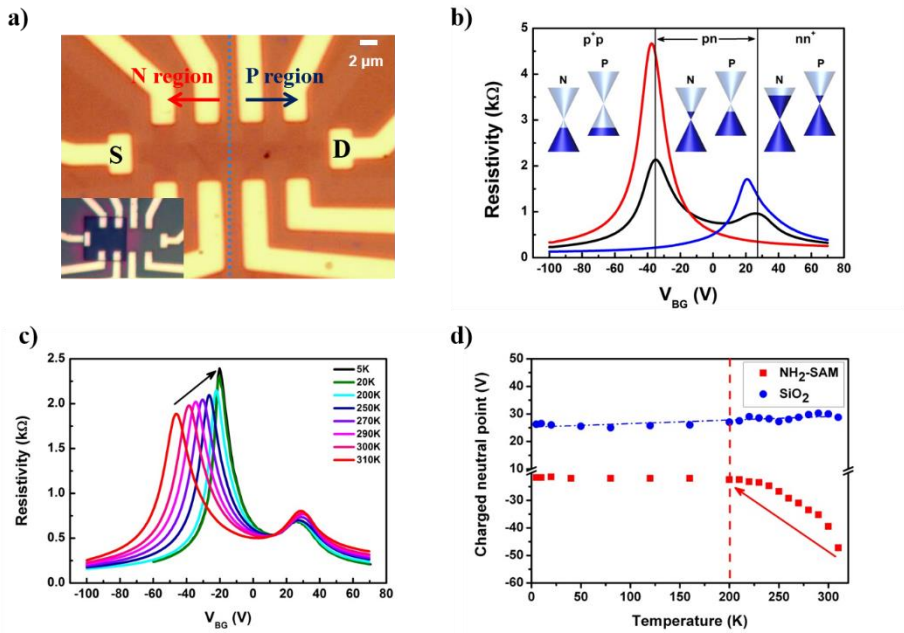


Figure. 6.7. Electrical transport measurements of graphene p-n junction devices. (a) An optical microscope image of graphene p-n junction device (scale bar: 2 μm). The left of inset shows the selectively n-doped area. (b) Resistivity versus gate voltage curves of the n-doped graphene and the inset shows the relationship between the Fermi energy and p-n doping levels of graphene. Straight line (black) was measured by 4-probe system and dotted lines (red, blue) by 2-probe. (c) Resistivity-gate voltage curves of the p-n junction depending on different temperature. (d) Charged neutral point dependence of temperature shift of amine modified and pristine graphene device.

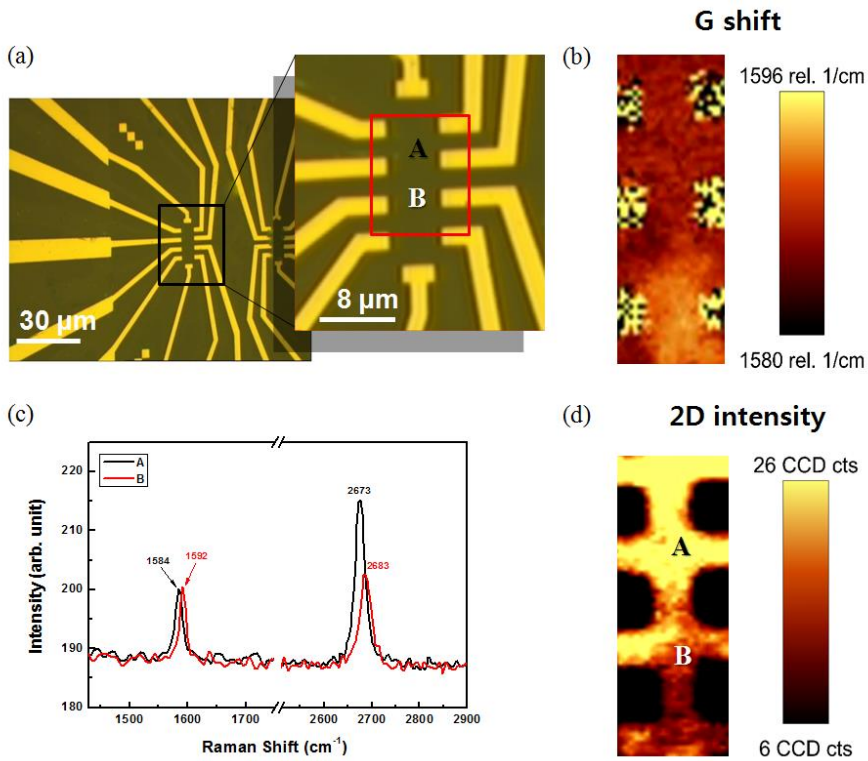


Figure. 6.8 Raman spectra of the graphene p-n junction device. (a) An optical microscope image of graphene p-n junction device for four probe measurement. Right is magnified image of a selected part of graphene device. (b) Raman maps of the G-bands shift and (d) 2D bands intensity of the marked red spot. A is graphene on SiO₂ and B is treated with NH₂-SAMs. (c) Raman spectra of A (black line) and B (red line) spots.

6.4 Summary

We have successfully demonstrated the doping effect with NH₂-SAMs and enhancement of mobility by using ODTS as repectively, moreover, by fabricating the selective doped graphene p-n junction devices. The SAMs doping process is simple and easily to use for the defined area, as well as the doping effect by the charged impurity from SAMs is strongly influenced by T on graphene FET and p-n junction devices. Graphene devices are characterized by optical microscopy for surface image and the doping type, carrier concentration, and Fermi energy level from the Dirac point are analyzed by Raman spectroscopy. From our study, this novel approach to produce a well patterned p-n junction without a complicated method opens a new process for controlling sample surface easily.

Chapter 7 Fast Synthesis of High-Performance Graphene Films by Hydrogen-Free Rapid Thermal Chemical Vapor Deposition

7.1. Introduction

Graphene and related materials have been intensively studied for the last few years due to their fascinating electrical,^[73] mechanical,^[149] and chemical^[150] properties. There have been many efforts to utilize these fascinating properties of graphene for macroscopic applications such as transparent conducting films useful for flexible electronics.^[74] The implementation of graphene requires a production worthy process, and it has been successfully demonstrated that a thermal chemical vapor deposition (T-CVD) process is capable of growing high-quality graphene on Cu substrates.^[22,151,152] This approach was found to be easily scalable up to meter sizes by employing roll-to-roll (R2R) methods.^[22] Even though the scalable production of graphene by R2R etching and transfer methods has been suggested previously,^[22] the typical T-CVD process that takes a few hours from heating and synthesis to cooling (Figure 7.1b) has practically limit the throughput of graphene production. In addition, the synthesis temperature as high as ~1,000 °C often results in the contamination by evaporated Cu, leading to the formation of defective graphene structures (Figure S7). The safety issue associated with the use of hydrogen gas also needs to be solved for massive production, and the hydrogen-free process was first reported in the growth of graphene on Ni by plasma-enhanced CVD (PE-CVD). On the other

hand, the rapid thermal annealing was suggested as an efficient heating method to synthesize high quality graphene at lower temperature.^[152] However, the hydrogen-free synthesis of large-area graphene on Cu foils with mass-production scale, quality, and uniformity has not been successfully demonstrated.

Recently, efforts have been devoted to perfect the CVD synthesis at lower temperature not only by adopting more efficient heating methods^[153,154] but by alloying,^[155] annealing^[22] or polishing catalytic substrates^[156] leading to larger single-crystalline domains and less structural defects such as grain boundaries^[118] and ripples.^[119] Nevertheless, the previously proposed high-throughput graphene synthesis methods based on Joule-heating^[152] and microwave plasma^[153] are found to yield either multilayered or defective graphene films whose sheet resistances are not suitable for resistive touch screen applications^[74]. In addition, the strong chemical doping to enhance conductivity is not desirable because it doesn't persist long enough for practical applications without proper encapsulation.^[157] The new equipment based on RT-CVD has been designed and manufactured for the following purposes: *i*) to maintain the high quality of graphene at lower synthesis temperature without using hydrogen gas; *ii*) to minimize growth time for high-throughput production; and *iii*) to achieve size, uniformity, reliability, durability and flexibility needed for industrial applications.

7.2 Experimental

7.2.1 Sample Preparation

We used H₂O₂ and H₂SO₄ (5:5) as Cu etchant and rinsed in DI water. The typical etching time for 35 μm thick Cu foil is ~20 min. Graphene samples were transferred by the TRT method on a SiO₂/Si substrate for Raman and electrical characterization after washing with DI water several times.^[151] The graphene samples for FET measurements were annealed in Ar/H₂ gas environment at 300°C. The full fabrication processes of the graphene FET device are illustrated in Figure 7.9.

7.2.2 Characterization

Micro Raman spectra were obtained using with 1 mW 514 nm Ar laser with a spot size of 2 μm (Renishaw inVia Raman Microscope). A home-made WF Raman microscope equipped with 532nm excitation laser was used to characterize RT-CVD graphene. The measurements of graphene field effect transistors were performed by using 3-terminal mode of Agilent 2602 systems with applying 10 mV source-drain voltage. The sheet resistance mapping of the large-area RT-CVD graphene (400x300 mm²) was carried out by a fully automatized measurement setup (Dasol ENG RS8-1G) based on van der Pauw method considering:

$$R_s = \frac{\pi V}{\ln 2 I}$$

where R_s is sheet resistance, V is applied voltage, and I is current.

7.3 Result and Discussion

Figure 7.1 shows a schematic representation of the RT-CVD synthesis setup. First, Cu foils (35 μm -thick, 99.85% purity) were vertically loaded to prevent deformation caused by thermal expansion and gravity, and then, the whole chamber was vacuumed below 2 mTorr for a few minutes. The heating unit is composed of 24 halogen lamps radiating the light ranging from visible to infrared (IR) wavelengths, which is advantageous in terms of growth area per time compared to conventional thermal heating methods utilizing open wire-coil sources (Figure 7.1a and Table. 7.1). However, the radiation close to visible wavelength is mostly reflected by Cu surface, and the temperature as high as 1,000 $^{\circ}\text{C}$ cannot be easily reached due to the energy loss. Thus, we adopted a graphite susceptor that efficiently transforms near infrared light to thermal radiation.^[152] It is also noteworthy that the high thermal conductivity of graphite additionally enhances the uniformity of heat distribution on the Cu surface. The reaction temperature was carefully monitored at five different positions using embedded thermocouples, which has been optimized to be ~ 970 $^{\circ}\text{C}$ for the highest-quality graphene synthesis. This temperature is slightly lower than the T-CVD temperature ($\sim 1,000$ $^{\circ}\text{C}$), but it is low enough to prevent the contamination by Cu evaporation. In the T-CVD system, the high energy needed for graphene growth is delivered by radiant heat from hot coils outside the quartz chamber to Cu substrates inside. In this case, the temperature on the Cu foil surface is always lower than the hot coils, so the chamber needs to be slightly overheated. However,

in the RT-CVD system, the halogen lamps inside the chamber deliver the shorter-wavelength radiation to a graphite susceptor that converts the radiation into thermal energy. Therefore, the highest temperature region is very close to the Cu surface, and the growth of graphene can be occurred more efficiently at lower heater temperature. In addition, the heating time of hot-coils is usually an hour long because whole chamber needs to be heated together, but the RT-CVD needs only a few minutes from room temperature to 970°C because only the susceptor and Cu surface are intensively heated. For the same reason, cooling is also faster for RT-CVD. This is very critical for the simple and cost-effective design of the R2R synthesis system. For example, cheaper and easily processible stainless steel chambers can be used for RT-CVD, but T-CVD usually requires more expensive and hardly shapable quartz or ceramic chambers.

Table 7.1. Comparisons of T-CVD grown graphene and RT-CVD grown graphene sample

	Graphene growth rate	Synthesis temperature	Use of H ₂ gas	Carrier gas	Mobility (cm ² /Vs) at 297K
T-CVD ^[123]	~ 200 cm ² /h	1,000 °C	Yes	Ar	~5,100
RT-CVD	~ 1,400 cm ² /h	970 °C	No	N ₂	~5,200

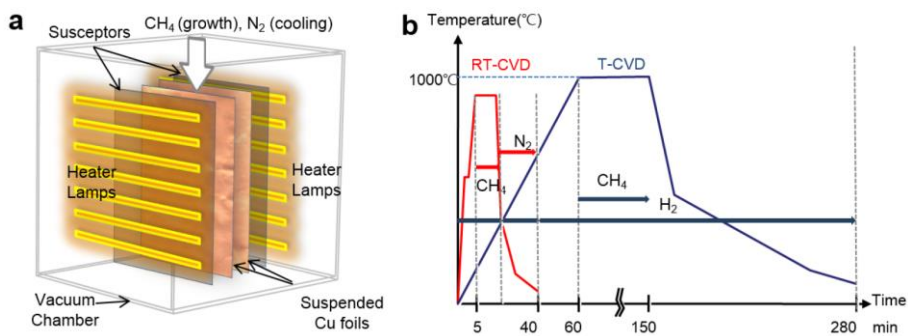


Figure 7.1. Schematic of RT-CVD synthesis and graphene Growth condition.

(a) Schematic illustration of RT-CVD synthesis setup. The graphite susceptors between heater lamps and Cu foils convert near-IR lights into thermal radiation. CH₄ and N₂ gases are used for growth and cooling processes, respectively. The Cu foils are suspended vertically during the growth. (b) Graphene growth conditions of RT-CVD compared with T-CVD.

After the temperature is stabilized, methane (CH₄, 99.999%) gas was flowed with a rate of 50 sccm at 550 mTorr. After 5 minutes, the chamber was cooled down to 600 °C with a rate of 1.5 °C /sec with flowing 50 sccm CH₄ at 550 mTorr. At 600 °C, nitrogen (N₂) gas (~5,000 sccm) was flushed into the chamber so that the foils are rapidly cooled down to room temperature. Thus, the whole RT-CVD synthesis process is ~40 minutes long and hydrogen gas free, which is advantageous for higher production throughput and for better safety, respectively (Figure 7.1b). After the growth, the graphene film on the Cu foil was attached to a thermal release tape (TRT, Jinsung Chemical Co.) using a laminator with accurately controlled pressure and temperature.^[150] Then, hydrogen peroxide and sulfuric acid based etching solution^[158] was sprayed to remove the Cu on the other side of

TRT as it passed through the R2R etching system,^[22] where the backside graphene was removed together with dissolved Cu. After fully etching the Cu foil, the graphene attached to TRT was rinsed with deionized (DI) water. Subsequently, the graphene film on TRT was inserted into the R2R laminator together with a target substrate. In this step, we used 100 μm -thick polyethylene terephthalate (PET) substrates whose glass transition temperature (T_g) is ~ 120 °C. As passing through the laminator at 110 °C with a speed of 0.5m/min and ~ 0.4 MPa pressure between rollers, the graphene films were successfully transferred onto the target substrate as TRT loses its adhesive force in the elevated temperature.^[150] The R2R-transferred graphene tends to follow the surface morphology of substrates, which maximizes the van der Waals contact area between graphene and PET. Therefore, no adhesive layer was needed between graphene and PET.^[123] The transferred graphene film was patterned by screen-masked and O₂ plasma etching for device fabrication.^[95] Therefore, no photoresist coating and lift-off processes were used, which is advantageous for cost-effective fabrication of graphene-based electronic devices. The whole graphene synthesis and film fabrication processes were automatized as shown in Figure 7.6.

The properties of graphene films produced by RT-CVD were carefully characterized by various spectroscopic methods including Raman and HR-TEM spectroscopy. Raman spectra (Figure 7.2a)^[39] and wide-field Raman (WF Raman)^[161] images (Figure 7.3b) show that the graphene films are dominantly monolayers with more than 95% coverage. In particular, the WF-Raman method is useful to monitor the

thickness and the quality of graphene films in real time^[161], which is an essential step to ensure the yield of production. The comparison between WF-Raman and micro-Raman mapping is shown in Figure S5. Scanning electron microscope (SEM) images, HR-TEM images^[155,160] (JEM-ARM200F and JEM-3010, JEOL) and diffraction patterns analysis show that the atomic structures of RT-CVD graphene are highly crystalline, and the sizes of graphene domains are 3~12 μm (Figs. 7.2c-f and Figure 7.6).

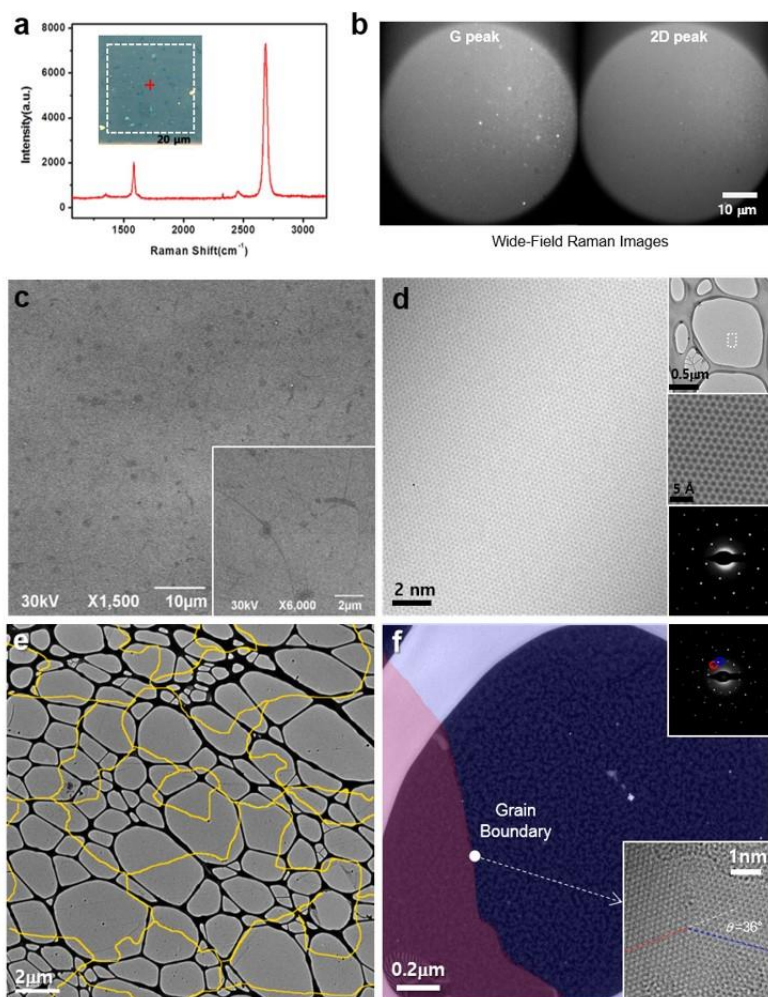


Figure 7.2. Spectroscopic analyses of RT-CVD graphene films. **(a)** Representative single-point Raman spectrum indicating the growth of high-quality graphene films. The inset shows an optical microscope image of RT-CVD graphene transferred by TRT methods on a SiO₂ substrate. **(b)** Wide-field (WF) Raman images filtered at G and 2D peak ranges, showing the uniformity of graphene films in real time. **(c)** SEM images of graphene on SiO₂ showing ripples and adlayers, but no cracks. **(d)** HR-TEM results showing the atomic lattice structures of RT-CVD graphene. The graphene samples were prepared with holey carbon grids (upper inset). The aberration-corrected scanning TEM image provides an atom-by-atom analysis of graphene (mid inset). The diffraction pattern indicates the corresponding graphene is a highly crystalline monolayer (lower inset). **(e)** Graphene domain distribution investigated by selected area diffraction patterns (SADP) and TEM imaging. **(f)** Graphene boundaries of RT-CVD graphene characterized by dark-field TEM and aberration corrected HT-TEM images. The left and right parts of the grain boundary are imaged with an aperture at red and blue circled spots of the diffraction pattern (upper inset). The atomic image shows that two graphene domains are smoothly connected with an angle of 36° (lower inset). See also Figure 2.7 for more dark-field TEM analyses.

Representative sheet resistance distribution measured over $400 \times 300 \text{ mm}^2$ graphene/PET film is $249 \pm 17 \text{ } \Omega/\text{sq}$, which qualifies for an industrial standard for transparent electrodes requiring 10 % deviation or less (Figure 7.3a. See also Figure S6a for full area mapping). To check the reproducibility of the RT-CVD method, we measured 10 different graphene samples sequentially grown at the same growth condition. The sheet resistance variation is measured to be only $232 \pm 36 \text{ } \Omega/\text{sq}$ (Figure 7.11), which indicates that the RT-CVD method is reliable enough for the repetitive growth of large-area graphene. It should be noted that such uniformity and reproducibility was hardly achievable by T-CVD methods³. Moreover, the sheet resistance persists for more than 12 weeks at ambient conditions (Figure 7.3b). We supposed that the remnants of the strongly p-doping etchants are captured between graphene and the substrate after TRT transfer, which considerably enhances the conductivity of graphene films with extraordinary stability. Indeed, the field-effect transistor (FET) characteristic (Figure 7.3b, inset) indicates that as-grown RT-CVD graphene is unusually *p*-doped and the mobility is as high as $5,290 \text{ cm}^2\text{V}^{-1}\text{s}^{-1}$ at room temperature (Figure 7.3d). UV-Vis spectroscopic analysis shows that the graphene/PET films are transparent for all visible wavelengths, while indium tin oxides (ITO), most popular transparent conducting materials, are less transparent in short visible wavelength ranges, which appears to be slightly yellowish (Figure 7.3c).^[28]

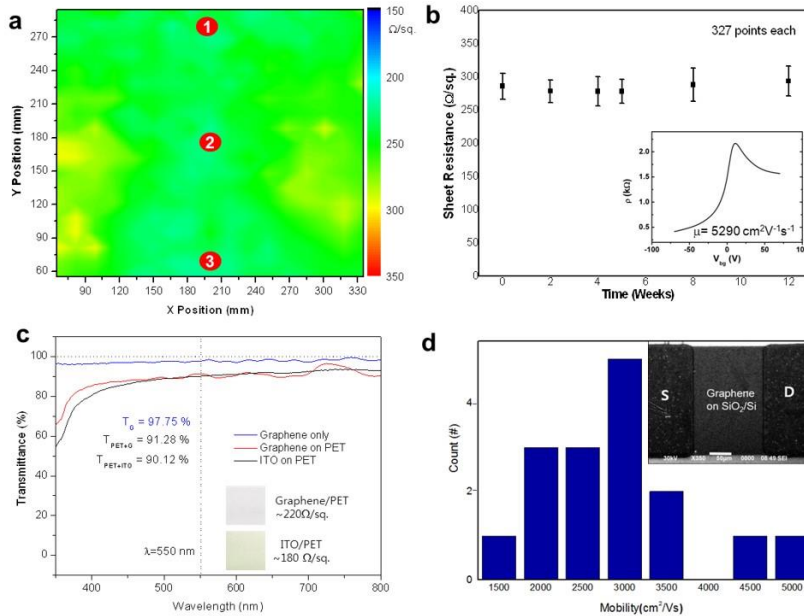


Figure 7.3. Electrical and optical analyses of RT-CVD graphene films. **(a)** Sheet resistance mapping of graphene film on PET showing sheet resistance distribution of $249 \pm 17 \Omega/\text{sq.}$ **(b)** Durability analysis of RT-CVD graphene films for 12 weeks, showing less than 10 % deviation from the initial value. The inset shows that the charge carrier mobility measured in a graphene FET is as high as $5,290 \text{ cm}^2\text{V}^{-1}\text{s}^{-1}$. **(c)** UV-Vis transmittance spectra of the graphene film on PET. The 2.25 % absorption at $\lambda = 550 \text{ nm}$ indicates that the graphene films are mostly single layers. **(d)** Charge carrier mobility distribution measured in RT-CVD graphene FET devices. The inset shows the SEM image of the FET device.

It has been reported that the grain size of graphene is an important factor that determines its conductivity based on the theoretical modeling.^[161] Thus, we tried to check the correlation between the grain size and the sheet resistance of the RC-CVD graphene. The graphene samples with different grain sizes were obtained from the three different regions corresponding to spot 1, 2, and 3 in Figure 7.3a. The grain size distribution of graphene on Cu foils can be optically characterized after H₂O₂ treatment as shown in Figure 7.4d-e,^[162] which matches well with the grain boundary mapping by TEM diffraction (Figure 7.4a-c). The grain sizes at the center region (spot 1) are found to be a few times larger than the edge region (spot 1 and 3), which is probably due to the inhomogeneous temperature gradient. However, the sheet resistances measured from the three spots are not significantly different although their grain sizes are clearly different, implying that the grain size factor becomes less dominant as the scale increases from nanoscale to micrometer scale, and other factors such as doping strength, defect density, and phonon scattering by nanoripples^[119] are more important for conductivity.

Finally, we demonstrated the actual application of the RT-CVD graphene for resistive multi-touch screens that are fully functional in the most sophisticated mobile phone (Figure 7.5g). The whole fabrication was processed with 400 x 300 mm² RT-CVD graphene films from roll-to-roll etching, O₂ plasma patterning, Ag electrode printing, to final assembly (Figure 7.5a-f, see Figure 7.8 for fabrication details). The resulting multi-touch device is working perfectly with the most sophisticated mobile phone, which is believed to be the first

demonstration of graphene application to actual consumer electronics devices.

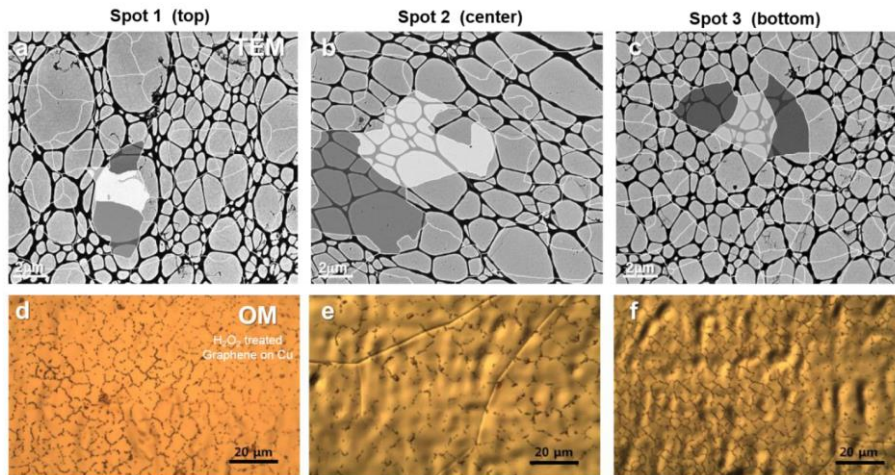


Figure 7.4. Grain boundary analyses by TEM and OM. (a-c) Grain boundary mapping of RT-CVD graphene films by TEM corresponding to the sheet resistance spot 1, 2, and 3 in Figure 3a, respectively. (d-f) Grain boundary mapping of H₂O₂-treated RT-CVD graphene on Cu foils by optical microscopes, corresponding to the red spots 1, 2, and 3 in Figure 3a, respectively. The grain size of graphene in the center region is a few times larger than the edge region, but actually, there is no significant difference in sheet resistance (226, 227, and 230 Ω/sq for the spots 1, 2, and 3, respectively)



Figure 7.5. Photographs of the fabrication processes of graphene-based resistive touch-screen devices. (a) Graphene on a Cu foil after RT-CVD growth. (b) TRT layer laminated on top of the graphene/Cu film at room temperature. (c) Graphene on a PET film after etching Cu and detaching TRT by hot laminating. (d) Patterned graphene/PET film by photolithography and O_2 plasma etching. (e) Screen-printed Ag electrodes on top of the patterned graphene electrodes. (f) Complete set of assembled layers including upper and lower graphene electrodes with a OCA layer in between. (g) Photograph of the graphene touch screen installed in a mobile phone (left) in comparison with an ITO-based touch screen phone (right).

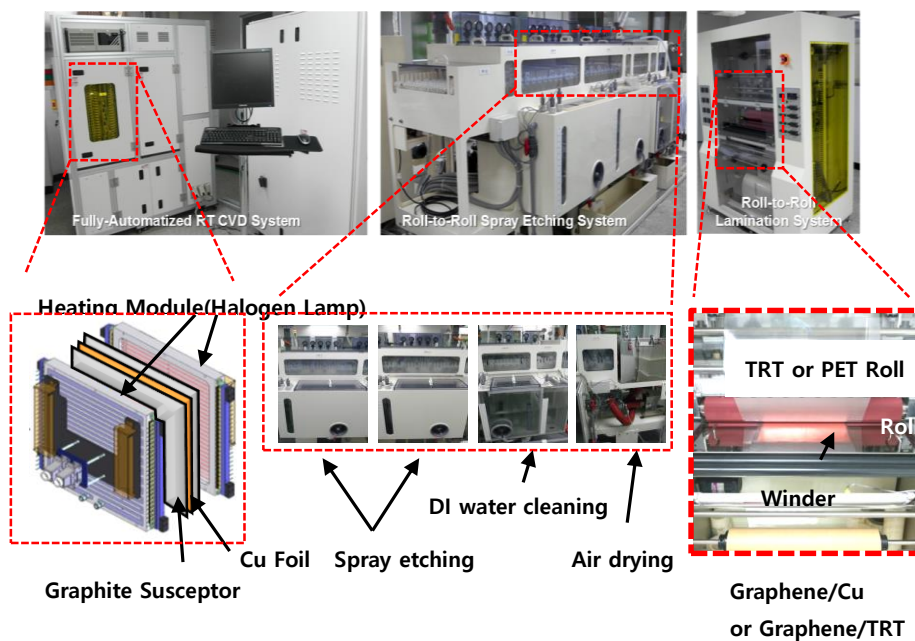


Figure 7.6. Photographs of production-compatible RT-CVD, roll-to-roll etching, and lamination systems.

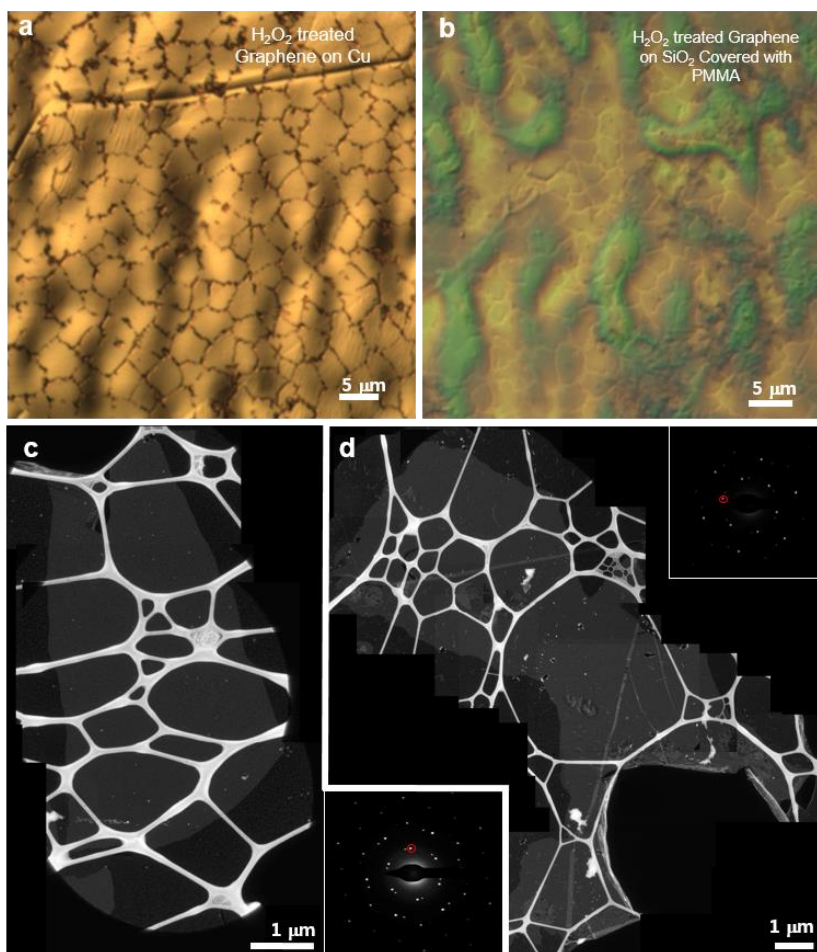


Figure 7.7. Grain size analyses of RT-CVD graphene films by H_2O_2 -assisted oxidation and HR-TEM methods. **(a)** 3D optical microscope image of graphene film on Cu after oxidation with 15% aqueous H_2O_2 solution for 30s (Ref. 23). **(b)** H_2O_2 -treated graphene film spin-coated with PMMA and transferred onto a SiO_2 ($t=300\text{nm}$)/Si substrate. The green colour originates from different PMMA thicknesses. **(c)** Graphene domain distribution investigated by selected area diffraction patterns (SADP) and TEM imaging. **(d)** Graphene boundaries of RT-CVD graphene characterized by dark-field TEM and aberration corrected HT-TEM images (Ref. 14 and 22). The left and right parts of the grain boundary are imaged with an aperture at red and blue circled spots of the diffraction pattern (upper inset). The atomic image shows that two graphene domains are smoothly connected with an angle of 30° .

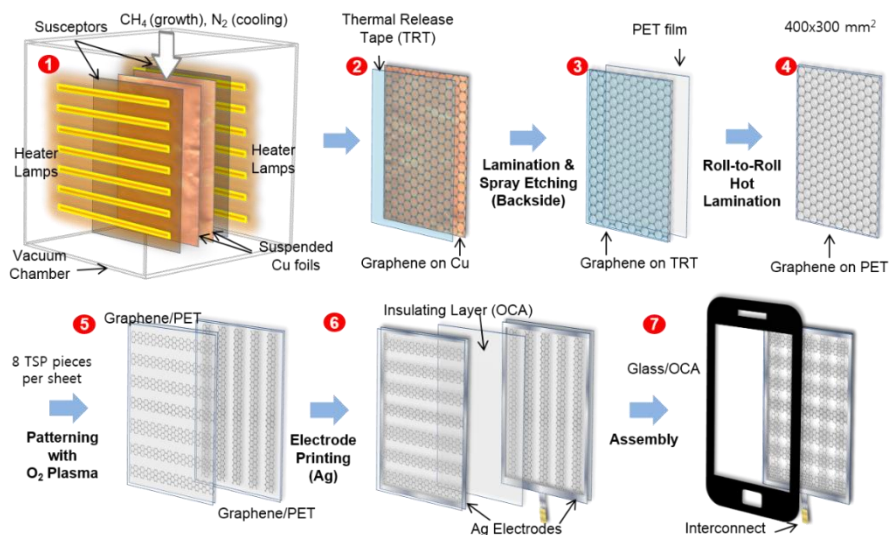


Figure 7.8. Schematic illustration of RT-CVD synthesis and subsequent production processes of graphene films and graphene-based capacitive touch screens. The graphite susceptors between heater lamps and Cu foils convert near-IR lights into thermal radiation. CH_4 and N_2 gases are used for growth and cooling processes, respectively. The Cu foils are suspended during the growth (1). After cooling, the Cu foils are laminated at room temperature with TRT tapes to protect graphene layers during Cu etching (2). The resulting graphene films on TRT are transferred to PET films by hot lamination at $\sim 110^\circ\text{C}$ with applying $\sim 0.4\text{Mpa}$ pressure between two rollers (3). Each $400 \times 300 \text{ mm}^2$ graphene sheet yields 8 touch screen panel (TSP) electrodes after patterning with O_2 plasma (5). Then, optically clear adhesive films are inserted between the upper and lower electrodes (6). Finally, glass covers, interconnecting electrodes, and driver circuits are attached to complete the assembly of the graphene-based capacitive touch screen modules (7).

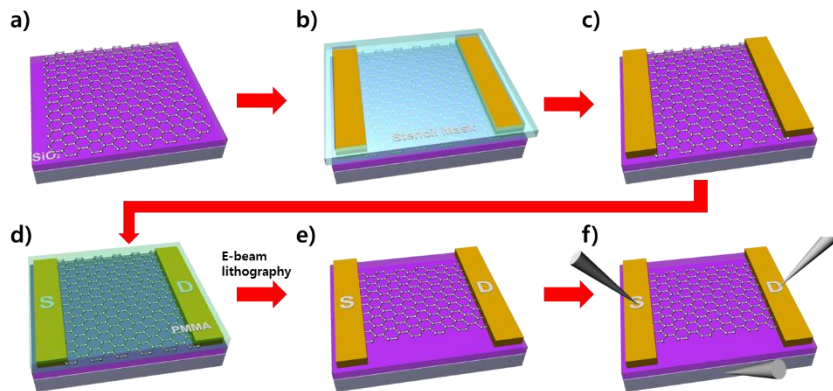


Figure 7.9. Schematic illustration for the fabrication processes of graphene FETs. (a) As-prepared graphene sample on a SiO₂ substrate after transfer. (b) Thermal deposition of metal electrodes (Cr/Au) through stencil masks. (c) Patterned metal contact electrodes after thermal deposition. (d) PMMA-coated graphene on a SiO₂ substrate. (e) A patterned graphene channel between two electrodes after e-beam lithography, O₂-plasma etching, and lift-off processes. (f) 3-Terminal measurement configuration of graphene FETs.

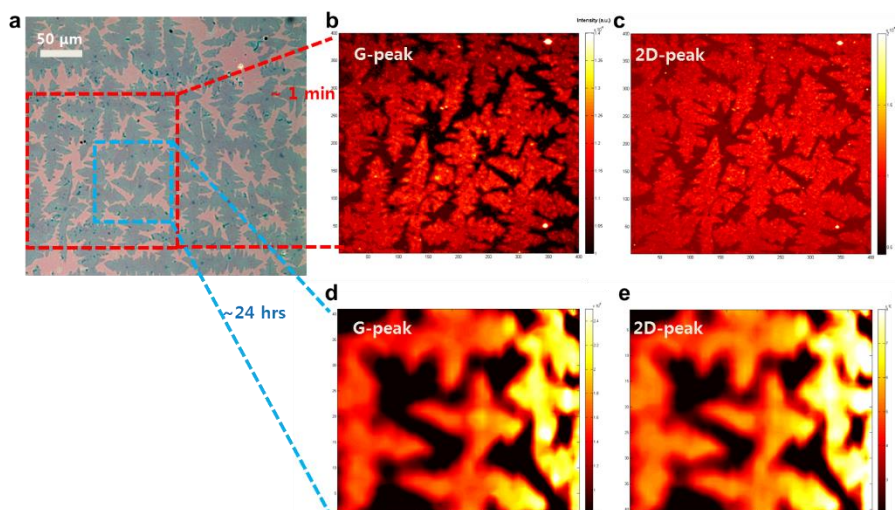


Figure 7.10. Optical image of partially grown graphene and comparing WF Raman and micro Raman mapping images. (a) Optical image of partially grown graphene flakes transferred on a SiO₂ substrate for Raman characterization. The red dot box indicates the scanning area for WF Raman (200 μm × 200 μm), and the blue dot box is for micro Raman (80 μm × 80 μm). The WF Raman images were obtained with the fixed Raman shift at 1585 cm⁻¹ for the G peak and (b) and at 2693 cm⁻¹ for the 2D peak (c). The micro Raman mapping (d, e) for the same area takes more than 20 hrs, while WF-Raman needs only a few minutes to obtained the full G and 2D mapping images.

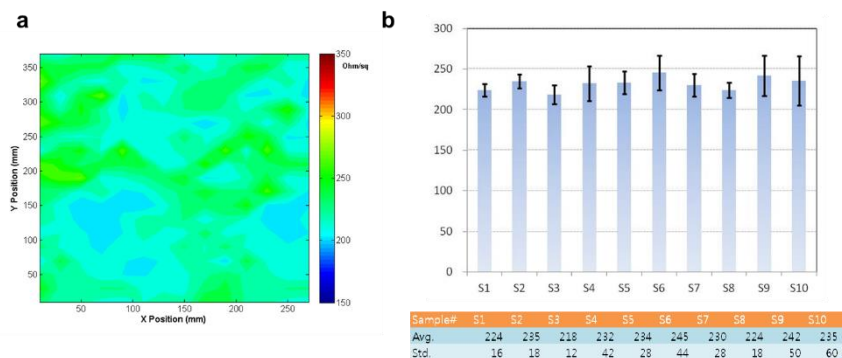


Figure 7.11. Sheet resistance of RT-CVD graphene. (a) Sheet resistance of 400x300mm² graphene film on PET. (b) Sheet resistance variation of 10 different graphene films sequentially grown by the RT-CVD method. (Unit, Ohm/sq.)

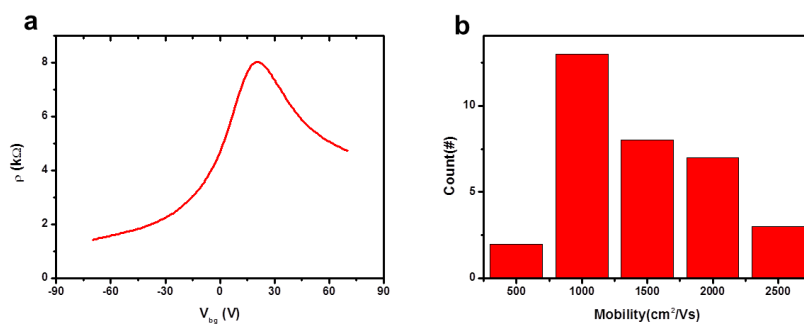


Figure 7.12. Electrical properties of graphene field effect transistors (a) Representative FET curve of graphene grown at 1,000 °C by RT-CVD. (b) Mobility distribution of the graphene FETs corresponding to a.

7.4 Summary

In conclusion, we have demonstrated RT-CVD growth, etching, and transfer systems that are mass-production compatible. The RT-CVD is advantageous not only because of the fast heating and cooling processes but because of hydrogen-free and lower temperature growth conditions. The outstanding properties of the RT-CVD graphene were confirmed by Raman spectroscopy, HR-TEM, and various electrical characterizations. Especially, the correlation between graphene grain size and the conductivity is found to be no more effective in case that the grain is larger than a few micrometer scale. We believe the RT-CVD method would be one of the best ways to mass-produce the high-quality graphene films satisfying the industrial standards needed for transparent conductors, which will facilitate various graphene-based applications^[31,120-122,163] as well as bring the advent of graphene-based consumer electronic devices forward.

Chapter 8 Giant Orbital Diamagnetism in Graphene at Room Temperature

8.1 Introduction

Magnetism of graphene has attracted much attention because of its combined charge and spin manipulation useful for futuristic spintronic devices^[164,165]. In addition, the magnetism of carbon-based materials is particularly important for lightweight actuator/sensor devices^[164,166] and electromagnetic wave shielding in flexible electronics^[167]. The previous studies on graphene's magnetism were mainly focused on paramagnetism^[168] and ferromagnetism^[169] that are related to electron spins, but the diamagnetism induced by the orbital motion of two-dimensional electron gas^[170] has been studied only by theoretical approaches^[171-175] due to the lack of measurable amount of samples. Recent advances in large-scale synthesis of graphene enabled a facile preparation of massive graphene samples by multiple stacking and transfer^[21,22]. Here we report a giant orbital diamagnetism in ultra-thin, lightweight, flexible, and transparent graphene films grown by chemical vapor deposition (CVD), where the diamagnetic susceptibility in perpendicular direction is measured to be ~100 times greater than the strongest diamagnetic materials such as bismuth.

8.2 Experimental

Characterization of CVD graphene.

A TEM (JEOL, JEM 2100) operated at 200 kV was used to investigate the crystalline quality of the CVD graphene film and their stack number. Confocal Raman spectroscopy with a 100× lens (WITec, 532 nm) was used to obtain both optical and Raman mapping images of graphene films. The area of all Raman mapping images is $20 \times 20 \mu\text{m}^2$ with 100 was used to obtain both optical and Raman mapping with Ar⁺ ion laser) was used to characterize the quality of the undoped graphene film. The laser powers were set to 10 mW to prevent the sample from heating. Magnetization measurements were carried out by a SQUID magnetometer.

Preparation of the samples for magnetic levitation

For free-standing CVD graphene sheet, we carried out the graphene growth on 25 μm -thick-Nickel (Ni) foil by H₂/CH₄ CVD method at 1000 °C for 5 min. The Ni foil was etched with hydrochloric acid (HCl) solution in the glass container. The floating multilayer graphene film was rinsed with DI water three times and dried in vacuum dry chamber at 100 °C. The four neodymium magnets are arranged with the north poles of adjoining magnets alternately pointing up and down. The alternating pole configuration gives rise to a strong field gradient and thus a strong levitating force. Therefore, we can levitate a piece of Highly Ordered Pyrolytic Graphite (HOPG), Kish graphite sheet, and multilayer graphene sheet grown by CVD above the magnets configuration.

The principle of diamagnetic levitation is estimated by the equilibrium between the gravitational force (mg) and the magnetic force (F_{mag}) acting on the levitating diamagnetic materials as follows^[187]:

$$mg = F_{\text{mag}} = (\chi V / \mu_0) BdB/dz \quad (1)$$

$$\rho g \mu_0 / \chi = BdB/dz \quad (2)$$

where m is the mass, g is the acceleration of gravity, μ_0 is the permeability of vacuum, χ is the volume magnetic susceptibility, V is the volume, B is the field intensity, z is the vertical position, ρ is the density. This equation means that the levitation height could be determined by the volume magnetic susceptibility among the graphitic materials.

A single layer of graphene can be easily broken by mechanical force. It is difficult to fabricate single layer and free-standing graphene film with nano-scale thickness. We prepared the graphene fiber using layer-by-layer (LBL) assembly method^[188] and directly drawing self-assembly method⁹. The graphene film was grown on 25 μm -thick-copper (Cu) foil by CVD method. After the removal of the top PMMA layer in acetone, the 4 layer LBL stacked graphene on Cu was cut into 20 mm \times 2 mm and placed in the Cu etchant solution. Etching the Cu foil can be done in a solution of ammonia persulfate (16 M). Then we should slowly replace the etching solution with DI water to clean the etchant contamination inside and outside of the graphene fiber. After three times washing, the graphene film was drawn out by tweezers and could be self-assembled into a fiber-like structure due to strong surface tension of liquid/air interface. Finally, the graphene fiber was naturally dried to obtain a free-standing fiber structure. Figure 8.1 shows schematic

drawings of a setup for the magnetic levitation of graphene fiber. The experimental setup was in acrylic plastic chamber in order to prevent outside air blowing into the system. The graphene fiber is picked up and placed at the end of the tweezers. The tweezers can be grounded by conducting pathway between the tweezers and the ground, resulting in that the excess charges are removed from the tweezers and the graphene fiber.

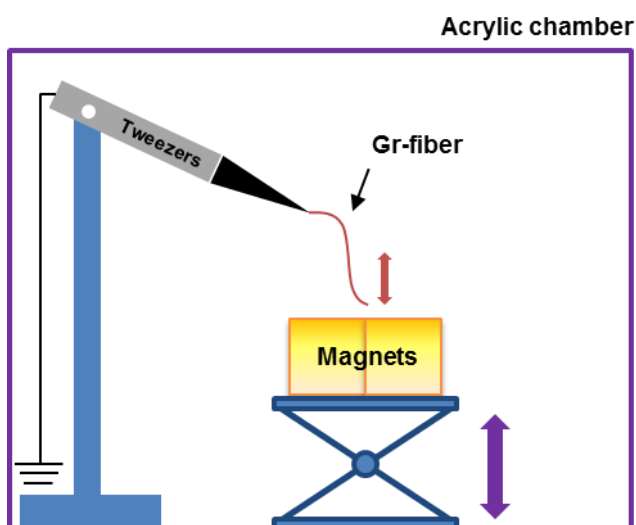


Figure 8.1. Schematic illustration of the experimental setup for the levitating CVD graphene fiber at room temperature.

Preparation of the samples for SQUID measurement

The 'reference' PMMA layer was prepared as same manner of PMMA/graphene layer. But the one difference is that the Cu foil was annealed without methane gas to prevent the growth of graphene on Cu foil. The PMMA (average Mw ~996000 by GPC, Sigma-Aldrich) was dissolved in chlorobenzene with a concentration of 46 mg/mL. The PMMA was spin-coated on both graphene on Cu foil at 4,200 rpm for 60s. Then, the PMMA was cured at 180 °C for 60 s. Since graphene grows on both sides of the Cu foil, we carried out the O₂ plasma etching to remove the back side of the graphene. The Cu foils were completely etched by ammonia persulfate (0.1 M) for 4 hours, and then, the PMMA/graphene and PMMA were rinsed with deionized water three times. After etching and rinsing, the PMMA/graphene and PMMA were transferred onto PET substrates or top of the diamagnetic plastic straw (Figure S6). It is well-known that PMMA can absorb substantial amounts of water, which is recognized as a strong diamagnetic material. To completely remove the water molecule in the PMMA and between PMMA layer and PET substrate, the samples were placed into a vacuum drying chamber at 100 °C (Figs. 8.3a-d). Finally, the PMMA/graphene and PMMA layers were consequently transferred and dried to complete multi-layered samples. Atomic force microscopy (AFM) images of 10 layers of PMMA/graphene and PMMA on the SiO₂/Si wafer revealed thickness of PMMA/graphene and PMMA layers after multi-stacking process (Figs. 8.2e-h). The thickness of 10 layers of PMMA and PMMA/graphene were 2 μm in the line scan AFM result, indicating uniform thickness PMMA coating on both graphene on Cu foil and

annealed Cu foil. We also confirmed no interlayer water absorption between PMMA layers after multilayer transfer. The PMMA/graphene/PET and PMMA/PET samples were cut into round shape in order to put in a diamagnetic plastic straw (sample holder). To avoid contamination, the samples were handled by a ceramic scissors and Teflon tweezers. For preparation of suspended samples, Floating PMMA/graphene film on DI water was consequently hung on the top of the diamagnetic plastic straw.

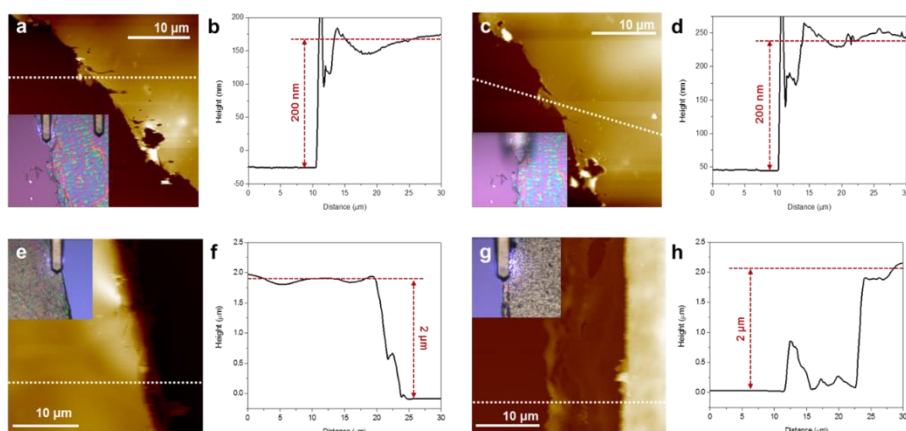


Figure 8.2. AFM images and line scans of an as-transfer PMMA/graphene (**a** and **b**) before and (**c** and **d**) after annealing at 100 °C, (**e** and **f**) 10 layers of PMMA/graphene, and (**g** and **h**) 10 layers of PMMA samples on SiO₂/Si substrates. The inserts show optical images of the samples. The thickness of one layer of PMMA/graphene and PMMA are about 200 nm. The white line in AFM images shows the AFM line scan of the samples.

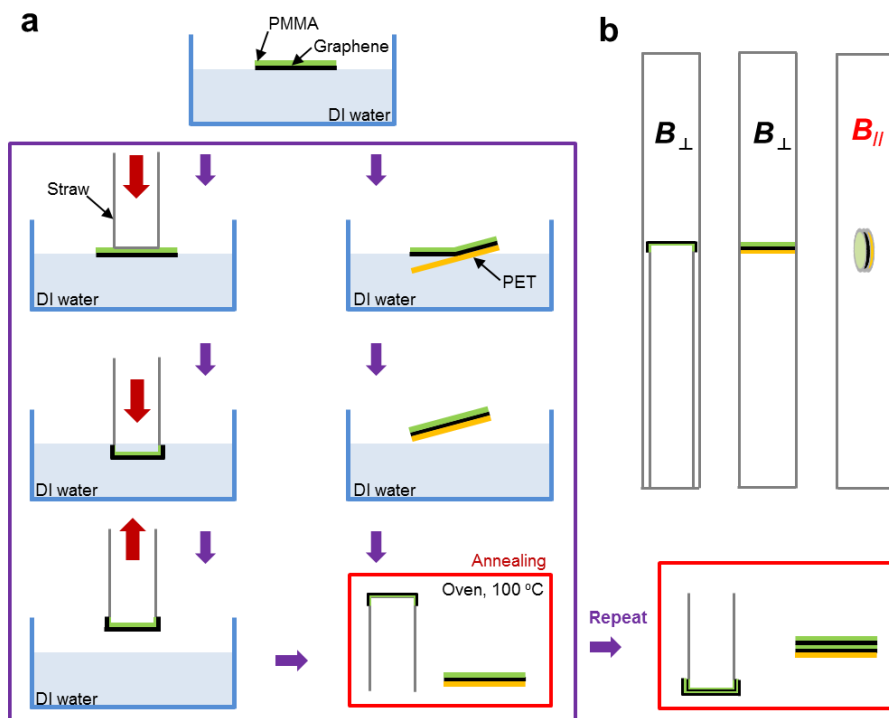


Figure 8.3. Preparation of PMMA/graphene and PMMA samples for MPMS. **a**, Schematic illustration of suspended on MPMS holder and transferred onto PET. **b**, Schematic illustration of samples loaded into MPMS holder along to the perpendicular and parallel directions.

8.3 Results and Discussion

Usually, the magnetic properties of heavy elements are governed by the arrangement and correlation of unpaired *d*- or *f*-electron spins with respect to applied magnetic field. However, the light elements such as carbon showing only *s*- or *p*-electrons are known to hardly show strong magnetism because of the weak correlation between electron spins. There have been reports on room-temperature magnetic ordering in graphene-based materials, where the defect-induced electron spins are coupled by long-range interactions, resulting in strong ferromagnetism^[169,175,176] On the other hand, it has been recently reported that non-defective multilayer graphene flakes show diamagnetism at room temperature and paramagnetism at low temperature^[177].

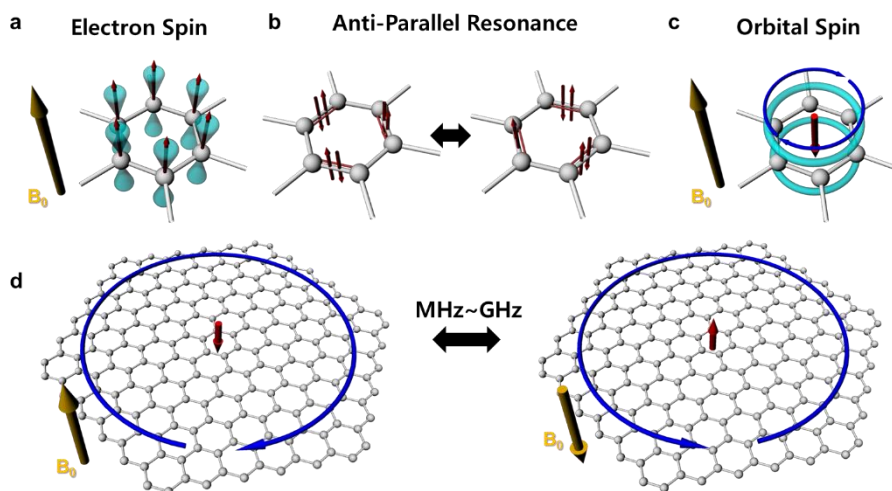


Figure 8.4. Schematic illustrations of a diamagnetic response in graphene with applied magnetic field. **a**, Paramagnetic electron spins on virtually non-bonded p -orbitals. **b**, Anti-parallel spin arrangement in virtually localized π -bonds in benzene without external magnetic field. **c**, Diamagnetic spin induced by cyclotron motion of delocalized π -electrons, induced by external magnetic field. **d**, Diamagnetic orbital spins in graphene and their response to oscillating magnetic fields. The red arrow denotes the induced diamagnetic moments. The cyclotron radius becomes smaller with increasing magnetic field.

The room-temperature diamagnetism of graphitic materials can be easily understood by a model of benzene as shown in Figure 8.4. Each carbon atom has one non-bonded p -electron with a virtual spin parallel to external field (Figure 8.4a), but actual spins are aligned in anti-parallel direction as the electrons fill the p -orbitals according to Pauli Exclusion Principle (Figure 8.4b). The resonance between two benzene structures gives rise to delocalization of π -electrons around the

six carbon atoms. Thus, the ring current can be induced by applying perpendicular magnetic field (B_0), leading to the generation of diamagnetic moment opposite to B_0 (Figure 8.4c). This phenomenon is commonly applied to the determination of molecular structures by nuclear magnetic resonance (NMR) spectroscopy, where the chemical shift of ^1H or ^{13}C atoms change as the induced magnetic field shields or deshields the magnetic fields around the nuclei ^[178]. The similar orbital magnetism has also been reported in fullerene ^[179]. The orbital diamagnetism of aromatic compounds greatly depends on doping (or oxidation number) because an additional charge breaks the resonance condition, leading to decrease in induced magnetic moment ^[172]. Likewise, the field-induced cyclotron motion of delocalized π -electrons in graphene results in anti-parallel diamagnetic moment that are oscillating with magnetic waves (Figure 8.4d) ^[173]. The electron mass in graphene is extremely small, which makes it easier to create fast ring current on graphene, leading to strong orbital diamagnetism ^[174]. This Dirac Fermion-like property of the electrons in graphene is easily lost when charged by doping as the cyclotron motion of heavier π -electron costs more energy ^[172].

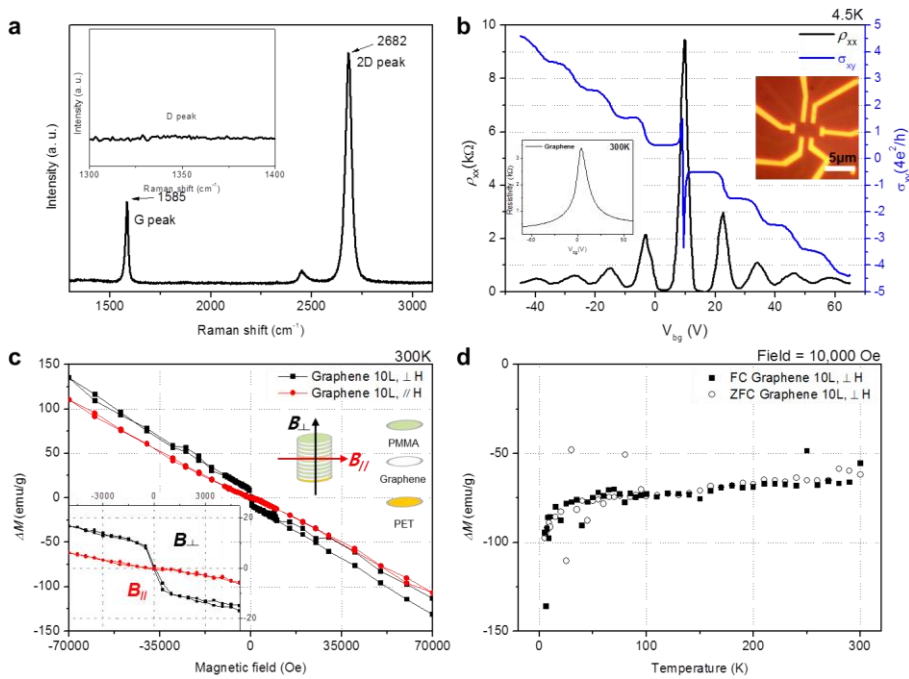


Figure 8.5. Optical, electrical and magnetic properties of CVD graphene. **a**, Raman spectrum of defect-free monolayer graphene. **b**, Electrical properties of a monolayer graphene Hall bar device in vacuum. Four-probe resistivity (left inset) is measured as a function of gate voltage in the monolayer graphene. The graphene Hall bar device is shown in the right inset at room temperature. The field effect mobility is $\sim 5,000 \text{ cm}^2 \text{ V}^{-1}\text{s}^{-1}$. The QHE effect at $T=4.5\text{K}$ and $B=8.9\text{T}$ is measured in the same device. The longitudinal resistivity ρ_{xx} and Hall conductivity ρ_{xy} are plotted as a function of gate voltage. The Hall effect mobility of this device is $\rho_{\text{Hall}} = \sim 7,100 \text{ cm}^2 \text{ V}^{-1}\text{s}^{-1}$ at 4.5K . **c**, Magnetization of 10 layers graphene at room temperature obtained by subtracting the background signal of polymer supports (PMMA and PET). The black and red plots correspond to the applied magnetic field along perpendicular (B_{\perp}) and parallel (B_{\parallel}) directions, respectively. Diamagnetic hysteresis loop is observed in the field range of $-70 \text{ kOe} < H < 70 \text{ kOe}$ at room temperature. The inset shows clear anisotropy in magnetic moment with respect to the sample orientation. **d**, Magnetization of 10 layers of graphene direction as function of temperature obtained by subtracting the background signal of PMMA suspended on MPMS holder. The filled symbols (opened symbols) correspond to the field cooling (zero field cooling) to the applied field perpendicular direction.

The low D peaks in Raman spectra (Figure 8.5a and 8.8), highly crystalline transmission electron microscope (TEM) images (Figure 8.9), and the carrier mobility as high as $5,000 \text{ cm}^2 \text{ V}^{-1} \text{ s}^{-1}$ (Figure 8.10) indicate that the quality of graphene is very high as well as the amount of defects is negligible ^[39]. Thus, it shows unique quantum Hall effect (QHE) (Figure 8.5b), where the non-conducting states are related to the cyclotron motion of electrons in graphene. This also supports the existence of massless Dirac Fermion-like electrons in orbital motion that gives rise to diamagnetic moments. Before we measure the magnetic property of graphene, we carefully checked any possible magnetic contamination^[180] such as Co, Ni and Fe through X-ray photoelectron spectroscopy (XPS) and angle-resolved (AR) XPS (Figure 8.10c). We only observed C 1s, O 1s, Si 2p and Si 2s in the XPS spectra, indicating that there is no detectable amount of magnetic impurities in the graphene sample, and thus, we can exclude the possibility of extrinsic magnetic impurity signals.

Magnetization measurements were performed using a superconducting quantum interference device (SQUID) measurement (MPMS XL). Single-layer graphene (SLG) on PET substrate exhibited a diamagnetic response at room temperature (Figs. 8.11a and 8.11d). In order to characterize the signal intensity depending on the number of graphene layers, the graphene films were coated with poly(methyl methacrylate) (PMMA) and consequently transferred to a 188 μm -thick PET substrate to complete multi-layer graphene/PMMA. The ‘reference’ PMMA layers are used to subtract the background signal of polymer

support (Figs. 8.10 and 8.11b-d). The PMMA layer on the graphene is used to decouple the interaction between upper and lower graphene layers, which is helpful to maintain the monolayer-like pristine properties of each graphene layer. The annealing process is performed and results in mobility enhancement and reducing doping concentration of graphene samples (details in Figure 8.10). We observed a noticeable decrease in the magnetization as graphene layers increase. This indicates that the decreased diamagnetism is related to the graphene morphology (ripple or structure) than the graphene mass. In order to substrate the effect of a PET substrate, we further prepared 1, 5, 10 layers of graphene/PMMA transferred to a top of diamagnetic plastic straw. Despite the absence of PET substrate, our samples exhibited noticeable diamagnetism and similar magnetization as function of number of graphene layers (Figure 8.11d-f). Especially, our observed value of the magnetic moment for the SLG after subtracting a PMMA layer background is $\Delta M \sim -300$ emu/g at 10 kOe, which is correspond with the measured magnetic moment for SLG after subtracting the PET substrate background. Therefore, a diamagnetic respond can come only from graphene at room temperature. Figure 8.7c plots the magnetizations for the 10 layers of graphene after subtracting the background signals from identical PMMA interlayers on a PET substrate. The perpendicular magnetic susceptibility for the graphene ($\chi = 3.502 \times 10^{-2}$, dimensionless SI volume susceptibility, $\text{emu cm}^{-3} \text{Oe}^{-1}$) is about thirty times larger than the parallel magnetic susceptibility ($\chi_{\parallel} = 1.26 \times 10^{-3}$). The unusual susceptibility anisotropy is originated from diamagnetic ring currents induced by external magnetic fields perpendicular to the π -surface of

graphene²¹. The absolute value of magnetization slightly increased as temperature decreased from 300 K to 10 K and dramatically increased as temperature decreases below 10 K (Figure 8.7d). Its shape and intensity did not differ significantly between field cooling (FC) and zero field cooling (ZFC). Interestingly, the magnetic susceptibility of graphene at low temperature (5K) is ~6 times larger than the room temperature value (Figs. 8.11c-d), which is almost the same order of magnitude of perfect diamagnetism ($\chi = -1$) that has been observed only in superconductors.

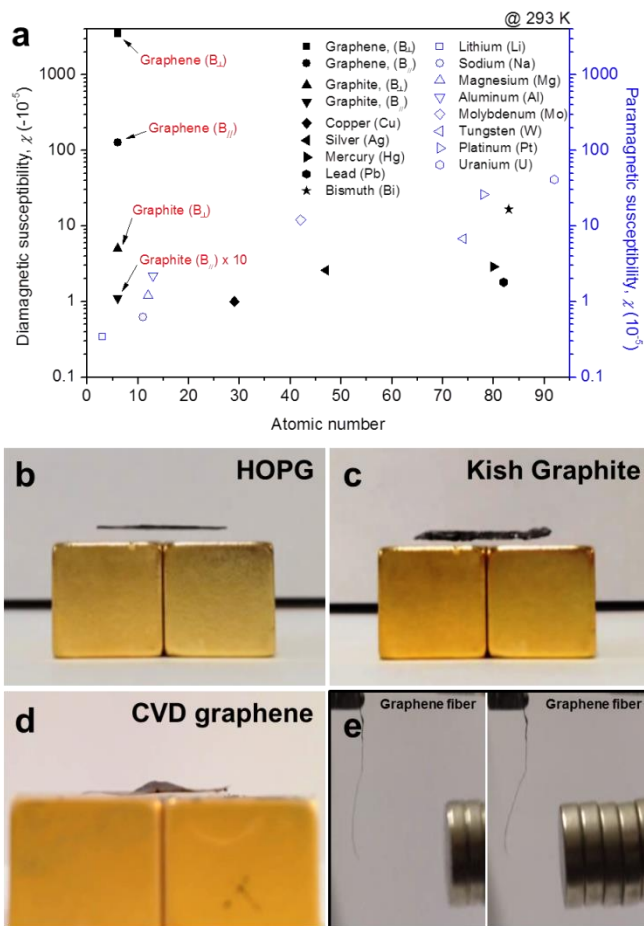


Figure 8.6. Magnetic susceptibility of CVD graphene. **a**, Magnetic susceptibility values of CVD graphene compared with conventional

diamagnetic and paramagnetic materials at room temperature. The values for graphene were measured in this work, and the other values are referred from various literature ^[182,183]. **b-e**, Photographs of the levitating diamagnetic materials (HOPG, Kish graphite, multilayer graphene sheet grown by CVD, and CVD graphene fiber) above magnets.

The magnetic susceptibility values ^[182,183] for the diamagnetic and paramagnetic materials at 293 K are compared in Table 8.1 and Figure 6a. Generally, the magnetic susceptibility of the elements with atomic number below 50 was as low as 5×10^{-5} . Usually, heavy metals with many core electrons exhibit isotropic diamagnetism with magnetic susceptibility within the range from -1×10^{-5} to -16.6×10^{-5} . On the other hand, the layered carbon materials such as graphite and graphene are expected to exhibit a strong diamagnetic anisotropy. Indeed, we confirmed that the magnetic susceptibility anisotropy ratio of graphene is as large as 27.8. It should be noted that the graphene exhibit ~210 times larger magnetic susceptibility at room temperature compared to bismuth (Bi) known as the strongest diamagnetic materials so far. As a graphene diamagnetism demonstration, we investigated the magnetic levitation behavior of the graphene-based diamagnetic materials such as Highly Ordered Pyrolytic Graphite (HOPG), Kish graphite, multilayer graphene sheet grown by CVD, and CVD graphene fiber (Figure 8.1 and Figure 8.6b-e). These diamagnetic materials can be levitated above neodymium permanent magnets at room temperature. Especially, the CVD graphene fiber can be levitated by approaching magnets configuration and demonstrates its massive diamagnetic

behaviour. This behaviour clearly suggests that the levitating CVD graphene sheet is caused by the strongest magnetic susceptibility of the CVD graphene at room temperature.

Table 8.1. Room temperature magnetic susceptibility values for graphene, graphite, and other magnetic materials.

Diamagnetic materials	$\chi (\times 10^{-5})$	Paramagnetic materials	$\chi (\times 10^{-5})$
Graphene, Perpendicular	3,502	Lithium (Li)	0.34
Graphene, Parallel	126	Sodium (Na)	0.62
Graphite, Perpendicular	5	Magnesium (Mg)	1.2
Graphite, Parallel	0.11	Aluminum (Al)	2.2
Copper (Cu)	1	Molybdenum (Mo)	12
Silver (Ag)	2.6	Tungsten (W)	7.5
Mercury (Hg)	2.9	Platinum (Pt)	26
Lead (Pb)	1.8	Uranium (U)	41
Bismuth (Bi)	16.6		

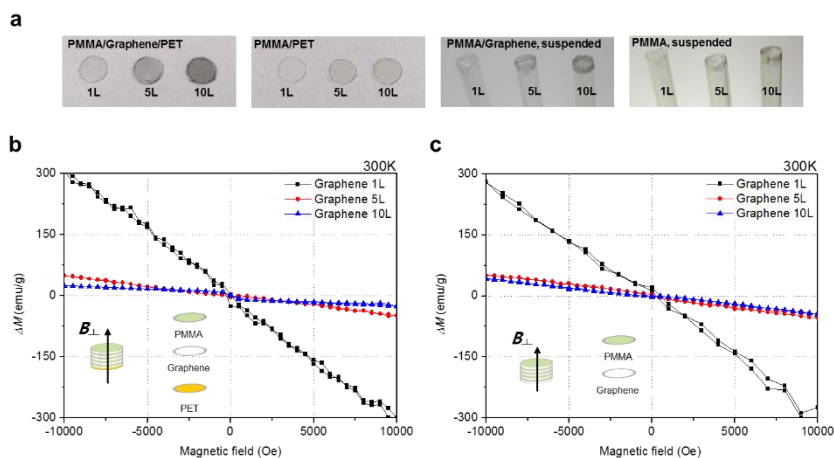


Figure 8.7. Layer Dependence of Magnetic susceptibility of CVD graphene. **a**, Optical images of the 1, 5, and 10 layers of PMMA and PMMA/graphene suspended on MPMS holder and transferred onto PET samples. **b**, Comparison of the diamagnetic magnetization in 1, 5, and 10 layers of CVD graphene at room temperature obtained by subtracting the background signal of polymer supports (PMMA and PET). **c**, Comparison of the diamagnetic magnetization in 1, 5, and 10 layers of CVD graphene at room temperature obtained by subtracting the background signal of PMMA support.

8.4 Summary

In summary, we have demonstrated that the large-scale multi-stacked graphene films show giant diamagnetism induced by the cyclotron motion of Dirac Fermion-like electrons. The measured perpendicular magnetic susceptibility was as high as -3.5×10^{-2} emu $\text{cm}^{-1} \text{Oe}^{-1}$, which is two orders of magnitude greater than conventional diamagnetic materials. Thus, we concluded that the graphene-based materials can be used as a strong diamagnet at room temperature, which would be very useful for magnet-based sensor devices, and various spintronic applications.

Table 8.2. Comparison of the mass of samples for MPMS measurements.

	Bare PET	5L of PMMA/ graphene on PET	5L of PMMA/ on PET	10L of PMMA/ graphene on PET	10L of PMMA/ on PET
Mass (g)	0.006495	0.006556	0.006223	0.00647	0.00637

Raman analyses of the CVD graphene sample

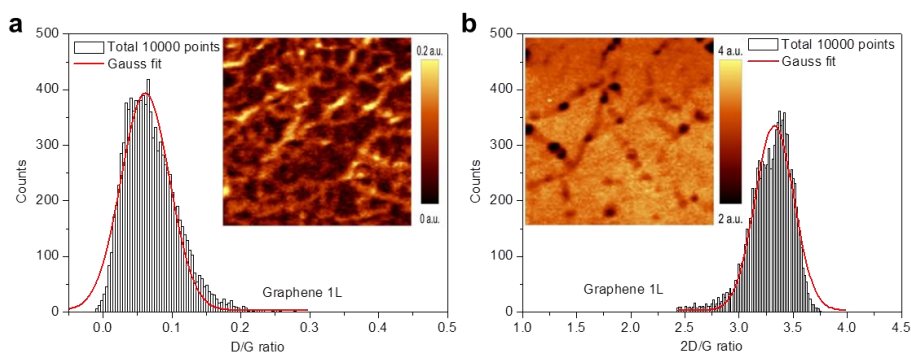


Figure 8.8. Raman analyses of graphene. **a** and **b**, Raman I_D/I_G ratio and I_{2D}/I_G ratio distributions of graphene on SiO_2 . Excitation wavelength $\lambda=532$ nm. The red curves are fitted with Gaussian distribution function. The inset images are corresponding Raman mapping images. Scan areas, $20 \times 20 \mu\text{m}^2$. A confocal Raman spectroscope with a $100\times$ lens (WITec, 532 nm) was used. The I_D/I_G values of graphene films are $\sim 0.061 \pm 0.070$, indicating that the defect density is negligibly small. The I_{2D}/I_G ratio distribution of both graphene films indicates that the graphene is dominantly a single layer.

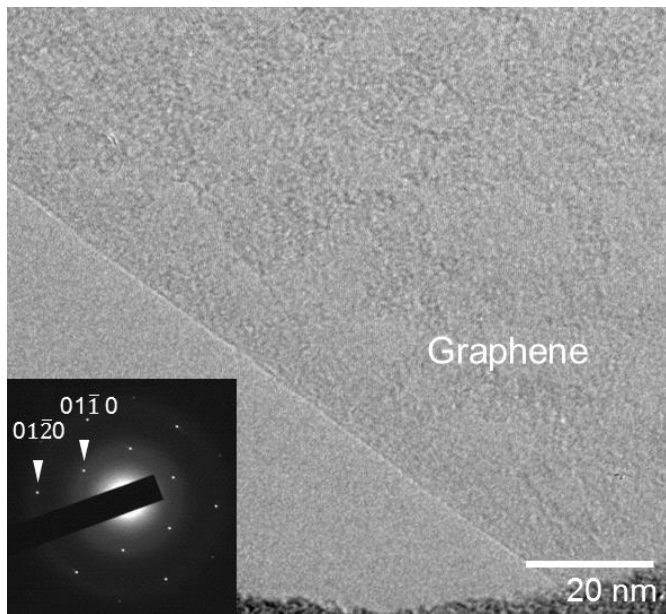


Figure 8.9. TEM analyses of the high quality CVD graphene. The clear selected area electron diffraction pattern showing the equivalent intensities between inner and outer diffraction spots indicates that the graphene is a highly single crystalline monolayer^[39,184].

XPS spectra of graphene film on SiO₂ substrate

X-ray photoelectron spectroscopy (XPS) was performed to determine the existence of magnetic impurities on the graphene film and the binding energy of the carbon bonding (VG Microtech ESCA2000). Figure S4a presents the XPS spectra of CVD graphene on a SiO₂/Si wafer. We only observed C 1s, O 1s, Si 2p, and Si 2s in the XPS spectra [79,185]. The C 1s and O 1s of the CVD graphene were observed at 284.6 and 532.8 eV, respectively. Further analysis of the graphene film was also performed by angle-resolved (AR) XPS, as shown in Figs. 8.10b-d. The AR XPS measurements were performed in an AR XPS spectrometer (Thermo VG, U. K.) using focused monochromated Al K α sources (1486.6 eV) with a spot size of 400 μ m. The high-resolution AR XPS data were acquired with pass energy of 50 eV and a step size of 0.1 eV. The AR XPS data were collected from the graphene film on the SiO₂ wafer at two angles (0° and 60°) to obtain detailed information on the bulk properties and surface properties of the material, respectively. The oxide peak (O 1s) is dominant at the normal angle (0°) whereas the intensity of carbon peak (C 1s) is relatively increased at near surface angle (60°). The difference in the C 1s peak intensity between the bulk structure and surface structure of single-layer graphene is due to the change of the analysis area and depth as a function of angle. Nevertheless, there is generally no difference between XPS and AR XPS data on graphene film. The high-resolution Ni 2p and Fe 2p peaks indicated that there were no magnetic impurities (Ni and Fe) at the two emission angles for all XPS spectra (Figs. 8.10c-d). Therefore, there is no detectable amount of magnetic impurities present on our CVD graphene.

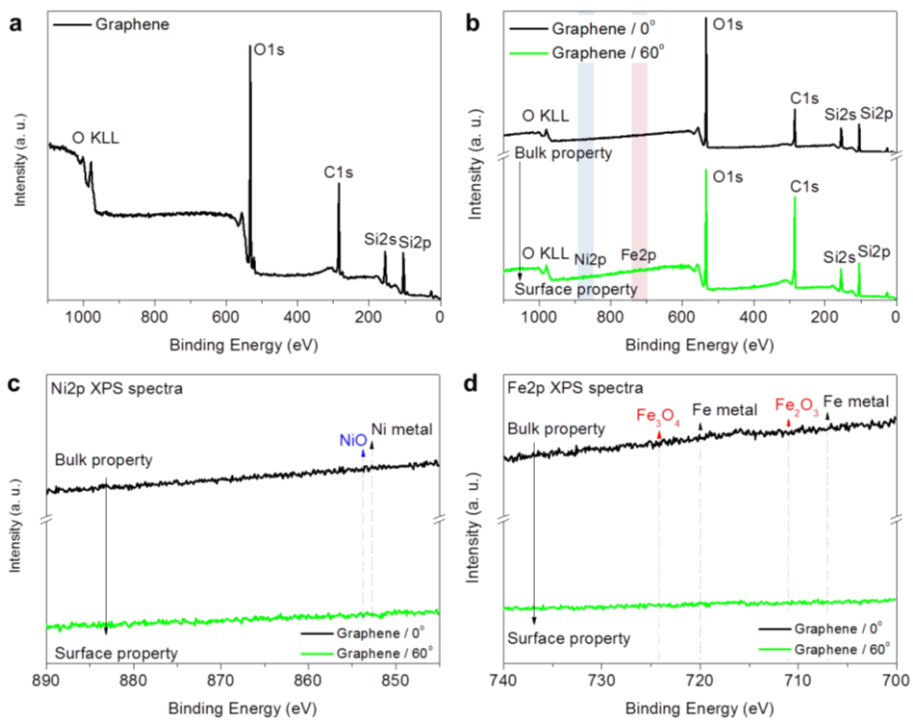


Figure 8.10. XPS and Angle-Resolved XPS spectra of CVD graphene. **a**, XPS wide scan spectrum of the graphene film. **b-d**, Angle-Resolved XPS spectra of the graphene film. No magnetic impurities are identified.

Detail calculations of graphene mass and graphene magnetization after background subtraction

A single-layer graphene's mass is simply $m_{\text{graphene}} = m_c \times [A / A_{\text{gr}}] / N_A$ where m_c is the mass of a carbon atom, A and A_{gr} are the area of graphene and graphene's unit cell^[186], and N_A is the Avogadro's number. For the single-layer graphene on MPMS measurement ($A = 2.3758 \times 10^5 \text{ m}^2$), $m_{\text{graphene}} = 9.2867 \times 10^{-9} \text{ g}$. We now explain a detailed calculation on how to subtract the background signal from the PMMA/graphene magnetization. For the PMMA and PET supports measurement, we first measured the mass of samples using ultra microbalances (XP2U, Mettler Toledo) as shown in Table 8.2. We could calculate the graphene magnetization as follow:

$$M_{\text{PMMA/PET}} (\text{emu/g}) = M_{\text{PMMA/PET}} (\text{emu}) / m_{\text{PMMA/PET}} (\text{g}) \quad (3)$$

$$M_{\text{graphene}} (\text{emu}) = [M_{\text{PMMA/PET}} (\text{emu/g}) \times m_{\text{PMMA+PET in PMMA/graphene/PET}} (\text{g}) - M_{\text{PMMA+PET in PMMA/graphene/PET}} (\text{emu})] \quad (4)$$

$$M_{\text{graphene}} (\text{emu/g}) = M_{\text{graphene}} (\text{emu}) / m_{\text{graphene}} (\text{g}) \quad (5)$$

For the PMMA support measurement, we also could calculate the graphene magnetization as follow:

$$M_{\text{graphene}} (\text{emu}) = M_{\text{PMMA/graphene}} (\text{emu}) - M_{\text{PMMA}} (\text{emu}) \quad (6)$$

$$M_{\text{graphene}} (\text{emu/g}) = M_{\text{graphene}} (\text{emu}) / m_{\text{graphene}} (\text{g}) \quad (7)$$

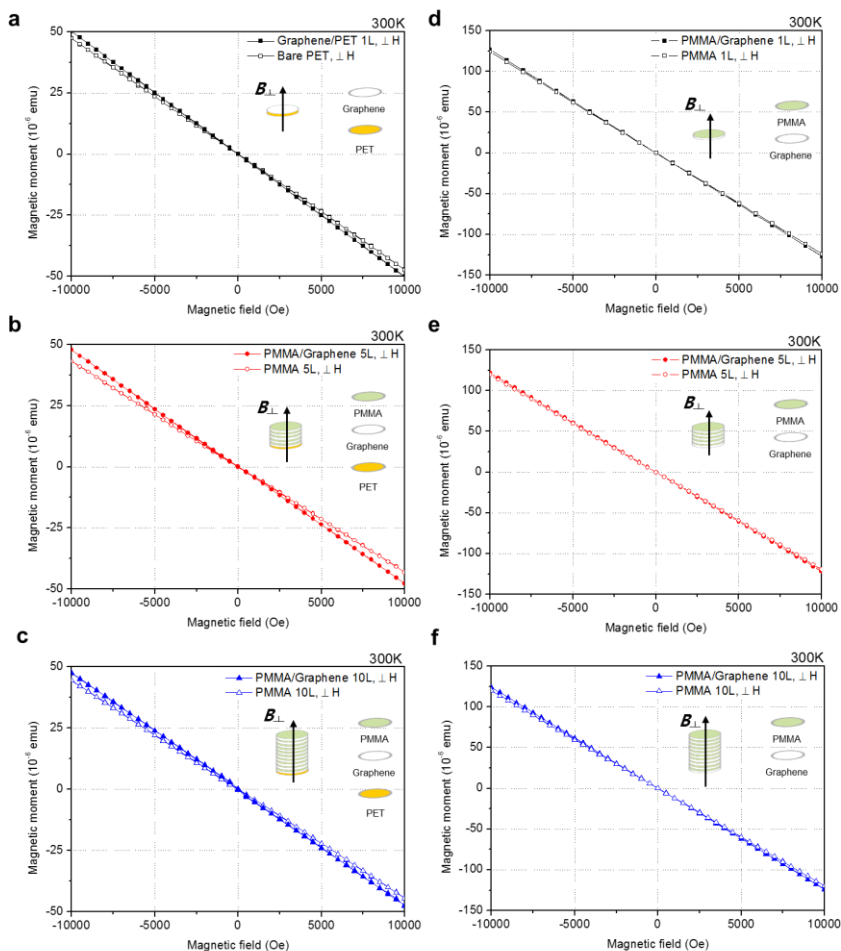


Figure 8.11. Raw magnetization of **a**, a bare PET and 1 layer of graphene on the bare PET, **b**, 5 layers of PMMA/graphene and PMMA on PET, **c**, 10 layers of PMMA/graphene and PMMA on PET. **d**, 1 layer of PMMA/graphene and PMMA, **e**, 5 layers of PMMA/graphene and PMMA, **f**, 10 layers of PMMA/graphene and PMMA samples suspended on sample holder.

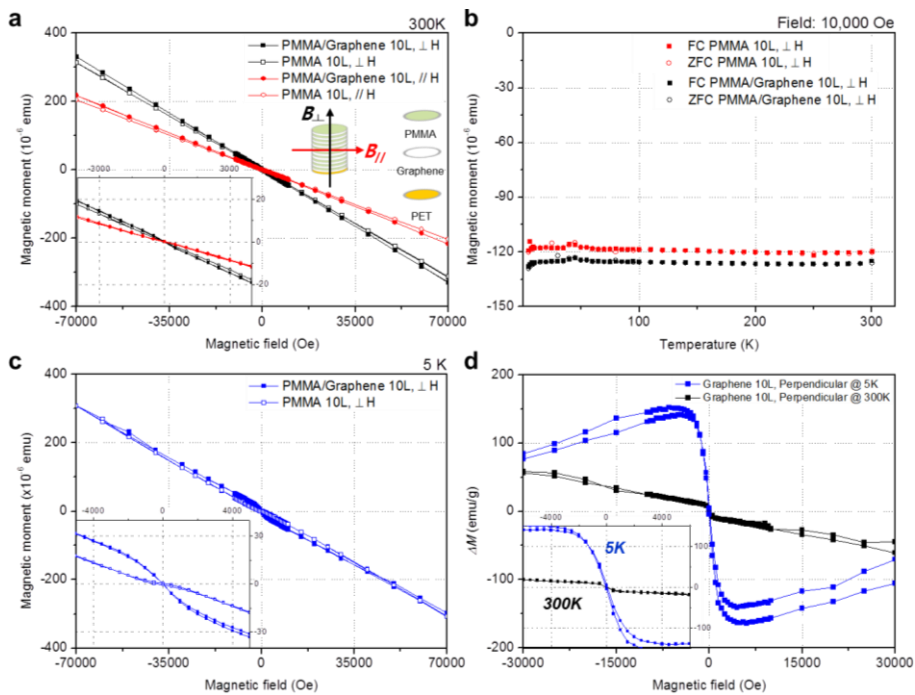


Figure 8.12. Raw magnetization of 10 layers of PMMA/graphene and PMMA on PET at **a**, 300K and **c**, 5K. Diamagnetic behavior is observed in the field range of $-70 \text{ kOe} < H < 70 \text{ kOe}$ at room temperature. The inset shows clear anisotropy in magnetic moment with respect to the sample orientation. **b**, Raw magnetization data for 10 layers of PMMA/graphene sample as function of temperature. $M(T)$ in perpendicular (B_{\perp}) at field $H = 10,000 \text{ Oe}$. **d**, Magnetization of CVD graphene in perpendicular orientation (B_{\perp}) at $T=5\text{K}$ (blue plot) and 300K (black plot).

Bibliography

- [1] K. S. Novoselov, A. K. Geim, S. V. Morozov, D. Jiang, Y. Zhang, S. V. Dubonos, I. V. Grigorieva, and A. A. Firsov, *Science* **306**, 666 (2004).
- [2] P. R. Wallace, *Phys. Rev.* **71**, 622 (1947).
- [3] A. H. Castro Neto, F. Guinea, N. M. R. Peres, K. S. Novoselov, and A. K. Geim, *Rev. Mod. Phys.* **81**, 109 (2009).
- [4] M. Y. Han, B. Özyilmaz, Y. Zhang, and P. Kim, *Phys. Rev. Lett.* **98**, 206805 (2007).
- [5] E. V. Castro, K. S. Novoselov, S. V. Morozov, N. M. R. Peres, J. M. B. L. dos Santos, J. Nilsson, F. Guinea, A. K. Geim, and A. H. C. Neto, *Phys. Rev. Lett.* **99**, 216802 (2007).
- [6] V. M. Pereira, A. H. Castro Neto, and N. M. R. Peres, *Phys. Rev. B* **80**, 045401 (2009).
- [7] J. Kong, N. R. Franklin, C. Zhou, M. G. Chapline, S. Peng, K. Cho, and H. Dai, *Science* **287**, 622 (2000).
- [8] K. Bradley, J.-C. P. Gabriel, M. Briman, A. Star, and G. Grüner, *Phys. Rev. Lett.* **91**, 218301 (2003).
- [9] F. Schedin, A. K. Geim, S. V. Morozov, E. W. Hill, P. Blake, M. I. Katsnelson, and K. S. Novoselov, *Nat. Mater.* **6**, 652 (2007).
- [10] T. O. Wehling, K. S. Novoselov, S. V. Morozov, E. E. Vdovin, M. I. Katsnelson, A. K. Geim, and A. I. Lichtenstein, *Nano Lett.* **8**, 173 (2008).

- [11] W. Chen, S. Chen, D. C. Qi, X. Y. Gao, and A. T. S. Wee, *J. Am. Chem. Soc.* **129**, 10418 (2007).
- [12] N. Jung, N. Kim, S. Jockusch, N. J. Turro, P. Kim, and L. Brus, *Nano Lett.* **9**, 4133 (2009).
- [13] X. Dong, D. Fu, W. Fang, Y. Shi, P. Chen, and L.-J. Li, *Small* **5**, 1422 (2009).
- [14] Y. H. Lu, W. Chen, Y. P. Feng, and P. M. He, *J. Phys. Chem. B* **113**, 2 (2009).
- [15] E. R. Hugo, J. Prasoon, K. G. Awnish, R. G. Humberto, W. C. Milton, A. T. Srinivas, and C. E. Peter, *Nanotechnology* **20**, 245501 (2009).
- [16] A. Bostwick, T. Ohta, T. Seyller, K. Horn, and E. Rotenberg, *Nature Phys.* **3**, 36 (2007).
- [17] L. S. Panchakarla, K. S. Subrahmanyam, S. K. Saha, A. Govindaraj, H. R. Krishnamurthy, U. V. Waghmare, and C. N. R. Rao, *Adv. Mater.* **21**, 4726 (2009).
- [18] L. Ci *et al.*, *Nat. Mater.* **9**, 430 (2010).
- [19] D. Wei, Y. Liu, Y. Wang, H. Zhang, L. Huang, and G. Yu, *Nano Lett.* **9**, 1752 (2009).
- [20] A. Reina, X. Jia, J. Ho, D. Nezich, H. Son, V. Bulovic, M. S. Dresselhaus, and J. Kong, *Nano Lett.* **9**, 30 (2009).
- [21] K. S. Kim *et al.*, *Nature* **457**, 706 (2009).
- [22] S. Bae *et al.*, *Nat. Nanotechnol.* **5**, 574 (2010).
- [23] Z. Li *et al.*, *ACS Nano* **5**, 3385 (2011).
- [24] K.-J. Peng, C.-L. Wu, Y.-H. Lin, Y.-J. Liu, D.-P. Tsai, Y.-H. Pai, and G.-R. Lin, *J. Phys. Chem. C* **1**, 3862 (2013).

- [25] J. Ryu *et al.*, *ACS Nano* **8**, 950 (2014).
- [26] Y. H. Yoon, J. W. Song, D. Kim, J. Kim, J. K. Park, S. K. Oh, and C. S. Han, *Adv. Mater.* **19**, 4284 (2007).
- [27] H.-Z. Geng, K. K. Kim, K. P. So, Y. S. Lee, Y. Chang, and Y. H. Lee, *J. Am. Chem. Soc.* **129**, 7758 (2007).
- [28] F. Bonaccorso, Z. Sun, T. Hasan, and A. C. Ferrari, *Nature Photon.* **4**, 611 (2010).
- [29] S. De and J. N. Coleman, *ACS Nano* **4**, 2713 (2010).
- [30] J.-H. Ahn and B. H. Hong, *Nat. Nanotechnol.* **9**, 737 (2014).
- [31] J. Kang, H. Kim, K. S. Kim, S.-K. Lee, S. Bae, J.-H. Ahn, Y.-J. Kim, J.-B. Choi, and B. H. Hong, *Nano Lett.* **11**, 5154 (2011).
- [32] H. Liu, Y. Liu, and D. Zhu, *J. Mater. Chem.* **21**, 3335 (2011).
- [33] J. A. Pickering, *International Journal of Man-Machine Studies* **25**, 249 (1986).
- [34] I. Hamberg and C. G. Granqvist, *J. Appl. Phys.* **60**, R123 (1986).
- [35] C. G. Granqvist, *Sol. Energ. Mat. Sol.* **91**, 1529 (2007).
- [36] M. S. Dresselhaus, G. Dresselhaus, R. Saito, and A. Jorio, *Physics Reports* **409**, 47 (2005).
- [37] L. G. Cançado *et al.*, *Phys. Rev. Lett.* **93**, 047403 (2004).
- [38] M. A. Pimenta, G. Dresselhaus, M. S. Dresselhaus, L. G. Cancado, A. Jorio, and R. Saito, *Phys. Chem. Chem. Phys.* **9**, 1276 (2007).
- [39] A. C. Ferrari *et al.*, *Phys. Rev. Lett.* **97**, 187401 (2006).
- [40] Z. Ni, Y. Wang, T. Yu, and Z. Shen, *Nano Res.* **1**, 273 (2008).

- [41] A. Gupta, G. Chen, P. Joshi, S. Tadigadapa, and Eklund, *Nano Lett.* **6**, 2667 (2006).
- [42] D. Graf, F. Molitor, K. Ensslin, C. Stampfer, A. Jungen, C. Hierold, and L. Wirtz, *Nano Lett.* **7**, 238 (2007).
- [43] M. Lazzeri, C. Attaccalite, L. Wirtz, and F. Mauri, *Phys. Rev. B* **78**, 081406 (2008).
- [44] J. Jiang, R. Saito, G. G. Samsonidze, S. G. Chou, A. Jorio, G. Dresselhaus, and M. S. Dresselhaus, *Phys. Rev. B* **72**, 235408 (2005).
- [45] J. Maultzsch, S. Reich, C. Thomsen, H. Requardt, and P. Ordejón, *Phys. Rev. Lett.* **92**, 075501 (2004).
- [46] G. G. Samsonidze, E. B. Barros, R. Saito, J. Jiang, G. Dresselhaus, and M. S. Dresselhaus, *Phys. Rev. B* **75**, 155420 (2007).
- [47] W. Kohn, *Phys. Rev. Lett.* **2**, 393 (1959).
- [48] S. Piscanec, M. Lazzeri, F. Mauri, A. C. Ferrari, and J. Robertson, *Phys. Rev. Lett.* **93**, 185503 (2004).
- [49] M. Lazzeri, S. Piscanec, F. Mauri, A. C. Ferrari, and J. Robertson, *Phys. Rev. B* **73**, 155426 (2006).
- [50] T. Ando, *J. Phys. Soc. Jpn.* **75**, 024707 (2006).
- [51] M. Lazzeri and F. Mauri, *Phys. Rev. Lett.* **97**, 266407 (2006).
- [52] DasA *et al.*, *Nat. Nanotechnol.* **3**, 210 (2008).
- [53] S. Pisana, M. Lazzeri, C. Casiraghi, K. S. Novoselov, A. K. Geim, A. C. Ferrari, and F. Mauri, *Nat. Mater.* **6**, 198 (2007).
- [54] J. Yan, Y. Zhang, P. Kim, and A. Pinczuk, *Phys. Rev. Lett.* **98**, 166802 (2007).

- [55] A. S. Charles, M. C. David, and M. Sumit, *Nanotechnology* **18**, 424014 (2007).
- [56] D. M. Cardamone, C. A. Stafford, and S. Mazumdar, *Nano Lett.* **6**, 2422 (2006).
- [57] A. H. MacDonald, *Kluwer Academic, Dordrecht, The Netherlands* (1990).
- [58] R. E. Prange, and S. M. Girvin, *Springer, New York* (1990).
- [59] S. Das Sarma, and A. Pinczuk, *Wiley, New York* (1996).
- [60] R. B. Laughlin, *Phys. Rev. B* **23**, 5632 (1981).
- [61] B. I. Halperin, *Phys. Rev. B* **25**, 2185 (1982).
- [62] R. Jackiw, *Physical Review D* **29**, 2375 (1984).
- [63] F. D. M. Haldane, *Phys. Rev. Lett.* **61**, 2015 (1988).
- [64] V. P. Gusynin and S. G. Sharapov, *Phys. Rev. Lett.* **95**, 146801 (2005).
- [65] N. M. R. Peres, F. Guinea, and A. H. Castro Neto, *Phys. Rev. B* **73**, 125411 (2006).
- [66] Y. Zheng and T. Ando, *Phys. Rev. B* **65**, 245420 (2002).
- [67] G. P. Mikitik and Y. V. Sharlai, *Phys. Rev. Lett.* **82**, 2147 (1999).
- [68] I. A. Luk'yanchuk and Y. Kopelevich, *Phys. Rev. Lett.* **93**, 166402 (2004).
- [69] A. K. Geim, and A. H. MacDonald, *Phys. Today* **60** (2007).
- [70] K. S. Novoselov, A. K. Geim, S. V. Morozov, D. Jiang, M. I. Katsnelson, I. V. Grigorieva, S. V. Dubonos, and A. A. Firsov, *Nature* **438**, 197 (2005).

- [71] Y. Zhang, Y.-W. Tan, H. L. Stormer, and P. Kim, *Nature* **438**, 201 (2005).
- [72] K. S. Novoselov *et al.*, *Science* **315**, 1379 (2007).
- [73] A. K. Geim and K. S. Novoselov, *Nat. Mater.* **6**, 183 (2007).
- [74] B. Sukang, K. Sang Jin, S. Dolly, A. Jong-Hyun, and H. Byung Hee, *Phys. Scripta* **2012**, 014024 (2012).
- [75] R. Ruoff, *Nat. Nanotechnol.* **3**, 10 (2008).
- [76] Z. Sun, S.-i. Kohama, Z. Zhang, J. Lomeda, and J. Tour, *Nano Res.* **3**, 117 (2010).
- [77] W. Chen, D. Qi, X. Gao, and A. T. S. Wee, *Progress in Surface Science* **84**, 279 (2009).
- [78] T. Agag and T. Takeichi, *Macromolecules* **34**, 7257 (2001).
- [79] S. Huh, J. Park, K. S. Kim, B. H. Hong, and S. B. Kim, *ACS Nano* **5**, 3639 (2011).
- [80] J. Park, W. H. Lee, S. Huh, S. H. Sim, S. B. Kim, K. Cho, B. H. Hong, and K. S. Kim, *The Journal of Physical Chemistry Letters* **2**, 841 (2011).
- [81] H. C. Kolb, M. G. Finn, and K. B. Sharpless, *Angew. Chem. Int. Ed.* **40**, 2004 (2001).
- [82] B. Guo, Q. Liu, E. Chen, H. Zhu, L. Fang, and J. R. Gong, *Nano Lett.* **10**, 4975 (2010).
- [83] Y.-C. Lin, C.-Y. Lin, and P.-W. Chiu, *Appl. Phys. Lett.* **96**, 133110 (2010).
- [84] B. Guo, L. Fang, B. Zhang, and J. R. Gong, in *Electron. Lett.* (Institution of Engineering and Technology, 2011), pp. 663.

- [85] D. B. Farmer, R. Golizadeh-Mojarad, V. Perebeinos, Y.-M. Lin, G. S. Tulevski, J. C. Tsang, and P. Avouris, *Nano Lett.* **9**, 388 (2009).
- [86] C. Hansch, A. Leo, and R. W. Taft, *Chem. Rev.* **91**, 165 (1991).
- [87] M. S. Dresselhaus and P. C. Eklund, *Adv. Phys.* **49**, 705 (2000).
- [88] H. Li, F. Cheng, A. M. Duft, and A. Adronov, *J. Am. Chem. Soc.* **127**, 14518 (2005).
- [89] N. Mohanty and V. Berry, *Nano Lett.* **8**, 4469 (2008).
- [90] Y. Wang, Y. Shao, D. W. Matson, J. Li, and Y. Lin, *ACS Nano* **4**, 1790 (2010).
- [91] P. K. Ang, W. Chen, A. T. S. Wee, and K. P. Loh, *J. Am. Chem. Soc.* **130**, 14392 (2008).
- [92] Y. Ohno, K. Maehashi, Y. Yamashiro, and K. Matsumoto, *Nano Lett.* **9**, 3318 (2009).
- [93] C.-H. Lu, H.-H. Yang, C.-L. Zhu, X. Chen, and G.-N. Chen, *Angew. Chem. Int. Ed.* **48**, 4785 (2009).
- [94] T. Ando, *J. Phys. Soc. Jpn.* **75**, 074716 (2006).
- [95] Y. Lee, S. Bae, H. Jang, S. Jang, S.-E. Zhu, S. H. Sim, Y. I. Song, B. H. Hong, and J.-H. Ahn, *Nano Lett.* **10**, 490 (2010).
- [96] K. I. Bolotin, K. J. Sikes, Z. Jiang, M. Klima, G. Fudenberg, J. Hone, P. Kim, and H. L. Stormer, *Solid State Commun.* **146**, 351 (2008).

- [97] R. R. Nair, P. Blake, A. N. Grigorenko, K. S. Novoselov, T. J. Booth, T. Stauber, N. M. R. Peres, and A. K. Geim, *Science* **320**, 1308 (2008).
- [98] A. A. Balandin, S. Ghosh, W. Bao, I. Calizo, D. Teweldebrhan, F. Miao, and C. N. Lau, *Nano Lett.* **8**, 902 (2008).
- [99] Q. Bao and K. P. Loh, *ACS Nano* **6**, 3677 (2012).
- [100] D. Wei, Y. Liu, Y. Wang, H. Zhang, L. Huang, and G. Yu, *Nano Lett.* **9**, 1752 (2009).
- [101] F. Schedin, A. K. Geim, S. V. Morozov, E. W. Hill, P. Blake, M. I. Katsnelson, and K. S. Novoselov, *Nat. Mater.* **6**, 652 (2007).
- [102] S. Ryu, L. Liu, S. Berciaud, Y.-J. Yu, H. Liu, P. Kim, G. W. Flynn, and L. E. Brus, *Nano Lett.* **10**, 4944 (2010).
- [103] J. B. Bult, R. Crisp, C. L. Perkins, and J. L. Blackburn, *ACS Nano* **7**, 7251 (2013).
- [104] S. Niyogi *et al.*, *Nano Lett.* **10**, 4061 (2010).
- [105] J. M. Englert *et al.*, *Nat Chem* **3**, 279 (2011).
- [106] D. Usachov *et al.*, *Nano Lett.* **11**, 5401 (2011).
- [107] R. Wang, S. Wang, D. Zhang, Z. Li, Y. Fang, and X. Qiu, *ACS Nano* **5**, 408 (2011).
- [108] P. Wei *et al.*, *Nano Lett.* **13**, 1890 (2013).
- [109] A. Deshpande, C.-H. Sham, J. M. P. Alaboson, J. M. Mullin, G. C. Schatz, and M. C. Hersam, *J. Am. Chem. Soc.* **134**, 16759 (2012).

- [110] K. Pi, K. M. McCreary, W. Bao, W. Han, Y. F. Chiang, Y. Li, S. W. Tsai, C. N. Lau, and R. K. Kawakami, *Phys. Rev. B* **80**, 075406 (2009).
- [111] J. H. Chen, C. Jang, S. Adam, M. S. Fuhrer, E. D. Williams, and M. Ishigami, *Nature Phys.* **4**, 377 (2008).
- [112] P.-H. Ho, Y.-C. Yeh, D.-Y. Wang, S.-S. Li, H.-A. Chen, Y.-H. Chung, C.-C. Lin, W.-H. Wang, and C.-W. Chen, *ACS Nano* **6**, 6215 (2012).
- [113] H. Corporation, (2007).
- [114] A. A. Efimova, V. N. Emel'yanenko, S. P. Verevkin, and Y. Chernyak, *J. Chem. Thermodyn.* **42**, 330 (2010).
- [115] J. E. Lee, G. Ahn, J. Shim, Y. S. Lee, and S. Ryu, *Nat Commun* **3**, 1024 (2012).
- [116] C. Casiraghi, S. Pisana, K. S. Novoselov, A. K. Geim, and A. C. Ferrari, *Appl. Phys. Lett.* **91**, 233108 (2007).
- [117] Q. Yu *et al.*, *Nat. Mater.* **10**, 443 (2011).
- [118] P. Y. Huang *et al.*, *Nature* **469**, 389 (2011).
- [119] G.-X. Ni *et al.*, *ACS Nano* **6**, 1158 (2012).
- [120] J. Ha, S. Park, D. Kim, J. Ryu, C. Lee, B. H. Hong, and Y. Hong, *Organic Electronics* **14**, 2324 (2013).
- [121] T.-H. Han, Y. Lee, M.-R. Choi, S.-H. Woo, S.-H. Bae, B. H. Hong, J.-H. Ahn, and T.-W. Lee, *Nature Photon.* **6**, 105 (2012).
- [122] S. B. Jo, J. Park, W. H. Lee, K. Cho, and B. H. Hong, *Solid State Commun.* **152**, 1350 (2012).

- [123] J. Kang, D. Shin, S. Bae, and B. H. Hong, *Nanoscale* **4**, 5527 (2012).
- [124] Y. Kim, J. Ryu, M. Park, E. S. Kim, J. M. Yoo, J. Park, J. H. Kang, and B. H. Hong, *ACS Nano* **8**, 868 (2014).
- [125] Y. Kim, J. M. Yoo, H. R. Jeon, and B. H. Hong, *Phys. Chem. Chem. Phys.* **15**, 18353 (2013).
- [126] M. Lafkioti, B. Krauss, T. Lohmann, U. Zschieschang, H. Klauk, K. v. Klitzing, and J. H. Smet, *Nano Lett.* **10**, 1149 (2010).
- [127] Y. y. Wang, Z. h. Ni, T. Yu, Z. X. Shen, H. m. Wang, Y. h. Wu, W. Chen, and A. T. Shen Wee, *J. Phys. Chem. C* **112**, 10637 (2008).
- [128] K. M. McCreary, K. Pi, and R. K. Kawakami, *Appl. Phys. Lett.* **98**, 192101 (2011).
- [129] S. A. DiBenedetto, A. Facchetti, M. A. Ratner, and T. J. Marks, *Adv. Mater.* **21**, 1407 (2009).
- [130] W. H. Lee, J. Park, Y. Kim, K. S. Kim, B. H. Hong, and K. Cho, *Adv. Mater.* **23**, 3460 (2011).
- [131] C. Stampfer, F. Molitor, D. Graf, K. Ensslin, A. Jungen, C. Hierold, and L. Wirtz, *Appl. Phys. Lett.* **91**, 241907 (2007).
- [132] S. Adam, E. H. Hwang, V. M. Galitski, and S. Das Sarma, *Proc. Natl. Acad. Sci. U.S.A.* **104**, 18392 (2007).
- [133] Z. Liu, J. Li, Z.-H. Sun, G. Tai, S.-P. Lau, and F. Yan, *ACS Nano* **6**, 810 (2012).
- [134] J. R. Williams, L. DiCarlo, and C. M. Marcus, *Science* **317**, 638 (2007).

- [135] D.-K. Ki, S.-G. Nam, H.-J. Lee, and B. Özyilmaz, *Phys. Rev. B* **81**, 033301 (2010).
- [136] J. B. Oostinga, H. B. Heersche, X. Liu, A. F. Morpurgo, and L. M. K. Vandersypen, *Nat. Mater.* **7**, 151 (2008).
- [137] T. Lohmann, K. von Klitzing, and J. H. Smet, *Nano Lett.* **9**, 1973 (2009).
- [138] I. Zanella, S. Guerini, S. B. Fagan, J. Mendes Filho, and A. G. Souza Filho, *Phys. Rev. B* **77**, 073404 (2008).
- [139] A. Grüneis and D. V. Vyalikh, *Phys. Rev. B* **77**, 193401 (2008).
- [140] F. Xia, D. B. Farmer, Y.-m. Lin, and P. Avouris, *Nano Lett.* **10**, 715 (2010).
- [141] A. Ulman, *Chem. Rev.* **96**, 1533 (1996).
- [142] C. Seung-Hwan, L. Yong-Uk, L. Jeong-Soo, J. Kang-Moon, K. Bo Sung, K. Hyang-Shik, K. Jang-Yeon, and H. Min-Koo, *Display Technology, Journal of* **8**, 35 (2012).
- [143] Y. Jang, J. H. Cho, D. H. Kim, Y. D. Park, M. Hwang, and K. Cho, *Appl. Phys. Lett.* **90**, 132104 (2007).
- [144] X. Du, I. Skachko, A. Barker, and E. Y. Andrei, *Nat. Nanotechnol.* **3**, 491 (2008).
- [145] S. Kobayashi *et al.*, *Nat. Mater.* **3**, 317 (2004).
- [146] S. V. Morozov, K. S. Novoselov, M. I. Katsnelson, F. Schedin, D. C. Elias, J. A. Jaszczak, and A. K. Geim, *Phys. Rev. Lett.* **100**, 016602 (2008).
- [147] J. Martin, N. Akerman, G. Ulbricht, T. Lohmann, J. H. Smet, K. von Klitzing, and A. Yacoby, *Nature Phys.* **4**, 144 (2008).

- [148] F. Guinea, M. I. Katsnelson, and M. A. H. Vozmediano, *Phys. Rev. B* **77**, 075422 (2008).
- [149] C. Lee, X. Wei, J. W. Kysar, and J. Hone, *Science* **321**, 385 (2008).
- [150] K. P. Loh, Q. Bao, G. Eda, and M. Chhowalla, *Nat Chem* **2**, 1015 (2010).
- [151] X. Li *et al.*, *Science* **324**, 1312 (2009).
- [152] W. R. Kim, J.; Arpiainen, S.; Svensk, O.; Li, C.; Lipsanen, H., *MRS Proceedings* **1451**, 27 (2012).
- [153] T. Yamada, M. Ishihara, J. Kim, M. Hasegawa, and S. Iijima, *Carbon* **50**, 2615 (2012).
- [154] T. Kobayashi *et al.*, *Appl. Phys. Lett.* **102**, 023112 (2013).
- [155] R. S. Edwards and K. S. Coleman, *Acc. Chem. Res.* **46**, 23 (2013).
- [156] Z. Luo, Y. Lu, D. W. Singer, M. E. Berck, L. A. Somers, B. R. Goldsmith, and A. T. C. Johnson, *Chemistry of Materials* **23**, 1441 (2011).
- [157] C. Yan, K.-S. Kim, S.-K. Lee, S.-H. Bae, B. H. Hong, J.-H. Kim, H.-J. Lee, and J.-H. Ahn, *ACS Nano* **6**, 2096 (2012).
- [158] J. R. Schellinger, *US Patent* (1983).
- [159] R. W. Havener, S.-Y. Ju, L. Brown, Z. Wang, M. Wojcik, C. S. Ruiz-Vargas, and J. Park, *ACS Nano* **6**, 373 (2012).
- [160] K. Kim, Z. Lee, W. Regan, C. Kisielowski, M. F. Crommie, and A. Zettl, *ACS Nano* **5**, 2142 (2011).
- [161] D. Van Tuan, J. Kotakoski, T. Louvet, F. Ortmann, J. C. Meyer, and S. Roche, *Nano Lett.* **13**, 1730 (2013).

- [162] C. Jia, J. Jiang, L. Gan, and X. Guo, *Scientific Reports* **2**, 707 (2012).
- [163] J. Jang, J. Park, S. Nam, J. E. Anthony, Y. Kim, K. S. Kim, K. S. Kim, B. H. Hong, and C. E. Park, *Nanoscale* **5**, 11094 (2013).
- [164] V. Y. Oleg, *Rep. Prog. Phys.* **73**, 056501 (2010).
- [165] Y.-W. Son, M. L. Cohen, and S. G. Louie, *Nature* **444**, 347 (2006).
- [166] W. Xue and T. Cui, *Sensors and Actuators A: Physical* **136**, 510 (2007).
- [167] Z. Chen, C. Xu, C. Ma, W. Ren, and H.-M. Cheng, *Adv. Mater.* **25**, 1296 (2013).
- [168] R. R. Nair, M. Sepioni, I. L. Tsai, O. Lehtinen, J. Keinonen, A. V. Krasheninnikov, T. Thomson, A. K. Geim, and I. V. Grigorieva, *Nature Phys.* **8**, 199 (2012).
- [169] J. Cervenka, M. I. Katsnelson, and C. F. J. Flipse, *Nature Phys.* **5**, 840 (2009).
- [170] A. S. Alexandrov and H. Capellmann, *Phys. Rev. Lett.* **66**, 365 (1991).
- [171] M. Koshino, Y. Arimura, and T. Ando, *Phys. Rev. Lett.* **102**, 177203 (2009).
- [172] M. Koshino, Y. Arimura, and T. Ando, *AIP Conf. Proc.* **1504**, 291 (2012).
- [173] Y. Ominato and M. Koshino, *Phys. Rev. B* **87**, 115433 (2013).
- [174] Y. Ominato and M. Koshino, *Phys. Rev. B* **85**, 165454 (2012).

- [175] Y. Wang, Y. Huang, Y. Song, X. Zhang, Y. Ma, J. Liang, and Y. Chen, *Nano Lett.* **9**, 220 (2009).
- [176] J. Hong, E. Bekyarova, P. Liang, W. A. de Heer, R. C. Haddon, and S. Khizroev, *Scientific Reports* **2**, 624 (2012).
- [177] M. Sepioni, R. R. Nair, S. Rablen, J. Narayanan, F. Tuna, R. Winpenny, A. K. Geim, and I. V. Grigorieva, *Phys. Rev. Lett.* **105**, 207205 (2010).
- [178] J. A. N. F. Gomes and R. B. Mallion, *Chem. Rev.* **101**, 1349 (2001).
- [179] M. P. Johansson, J. Jusélius, and D. Sundholm, *Angew. Chem. Int. Ed.* **44**, 1843 (2005).
- [180] F. M. Hu, T. Ma, H.-Q. Lin, and J. E. Gubernatis, *Phys. Rev. B* **84**, 075414 (2011).
- [181] G. Merino, T. Heine, and G. Seifert, *Chem. Eur. J.* **10**, 4367 (2004).
- [182] H. D. Young, Freedman, R. A. , *Addison-Wesley Publishing Company* (2013).
- [183] K. S. a. G. Krishnan, N. , *Nature* **139**, 667 (1937).
- [184] A. Dato, V. Radmilovic, Z. Lee, J. Phillips, and M. Frenklach, *Nano Lett.* **8**, 2012 (2008).
- [185] D. Choudhury, B. Das, D. D. Sarma, and C. N. R. Rao, *Chem. Phys. Lett.* **497**, 66 (2010).
- [186] JensenK, K. Kim, and ZettlA, *Nat. Nanotechnol.* **3**, 533 (2008).
- [187] M. Kobayashi and J. Abe, *J. Am. Chem. Soc.* **134**, 20593 (2012).

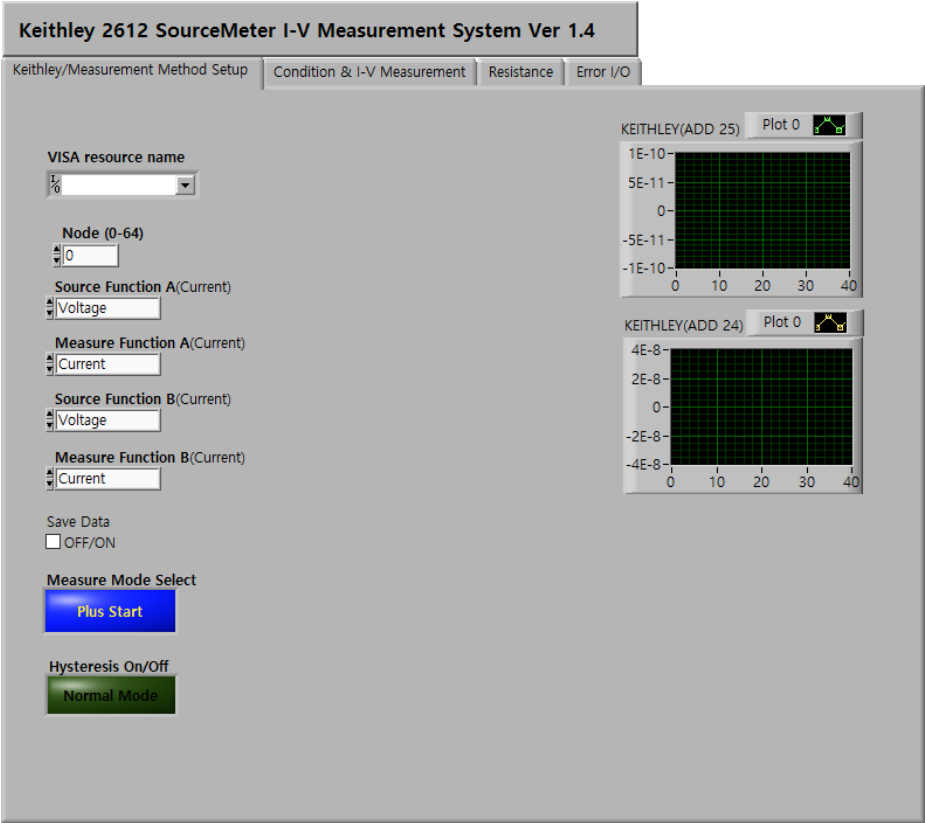
- [188] Y. Wang, S. W. Tong, X. F. Xu, B. Özyılmaz, and K. P. Loh, *Adv. Mater.* **23**, 1514 (2011).
- [189] X. Li, T. Zhao, K. Wang, Y. Yang, J. Wei, F. Kang, D. Wu, and H. Zhu, *Langmuir* **27**, 12164 (2011).
- [190] N. D. Mermin and H. Wagner, *Phys. Rev. Lett.* **17**, 1133 (1966).
- [191] H. Shpaisman *et al.*, *Chemical Science* **3**, 851 (2012).
- [192] S. Fratini and F. Guinea, *Phys. Rev. B* **77**, 195415 (2008)

Appendix A LabVIEW Programming for Electrical Measurement

- Keithley 2612 SourceMeter

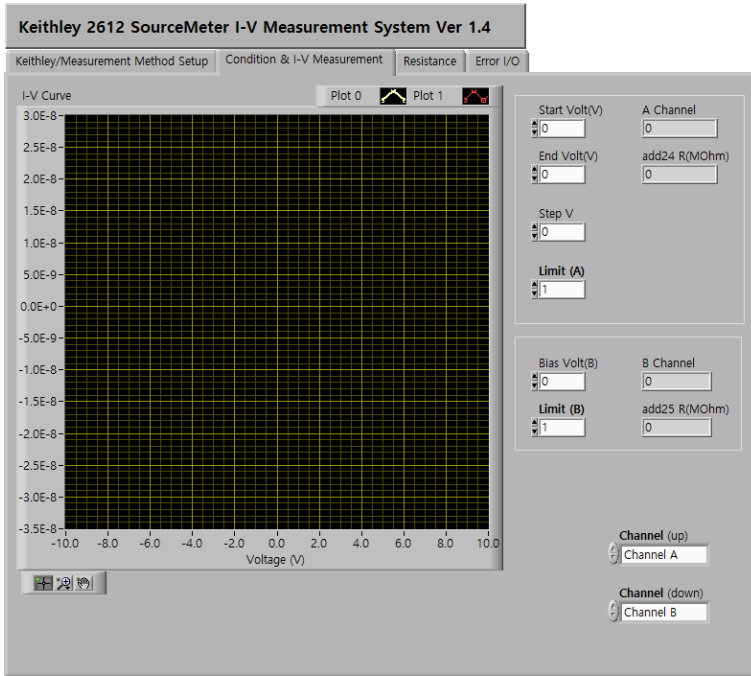
Front Panel

Input set up part



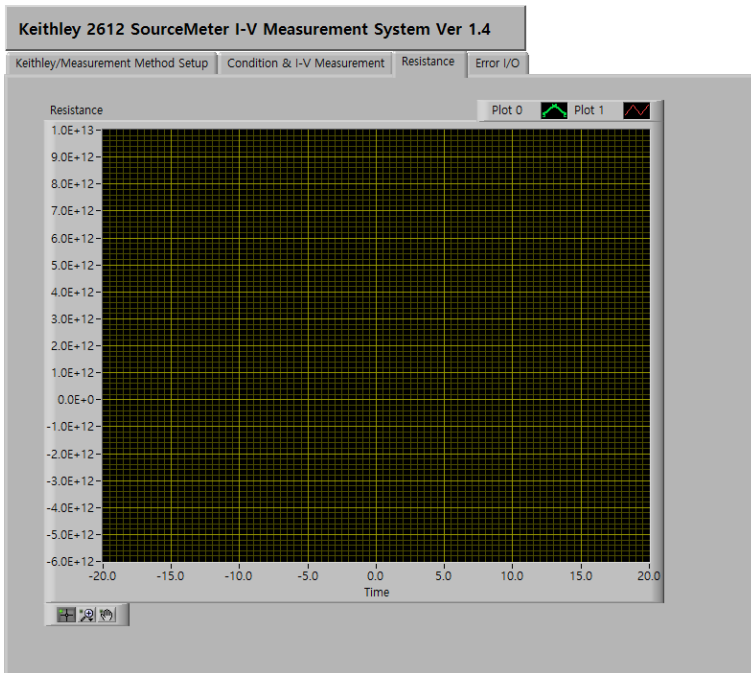
This Program is made by Youngsoo Kim.

I-V measurement display panel



This Program is made by Youngsoo Kim.

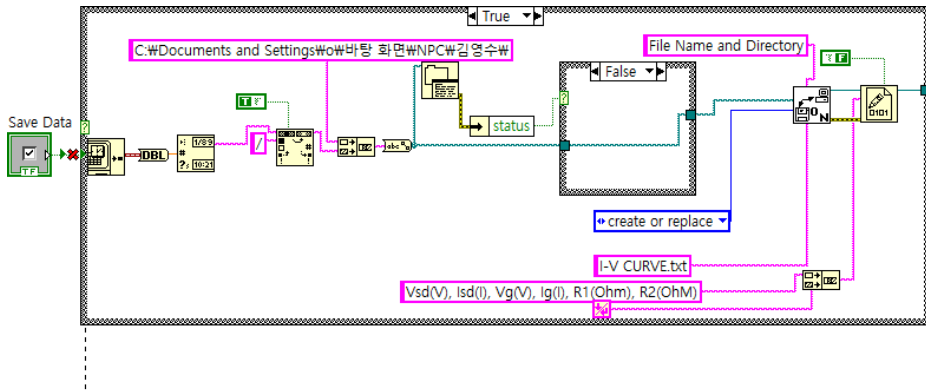
Resistance display panel



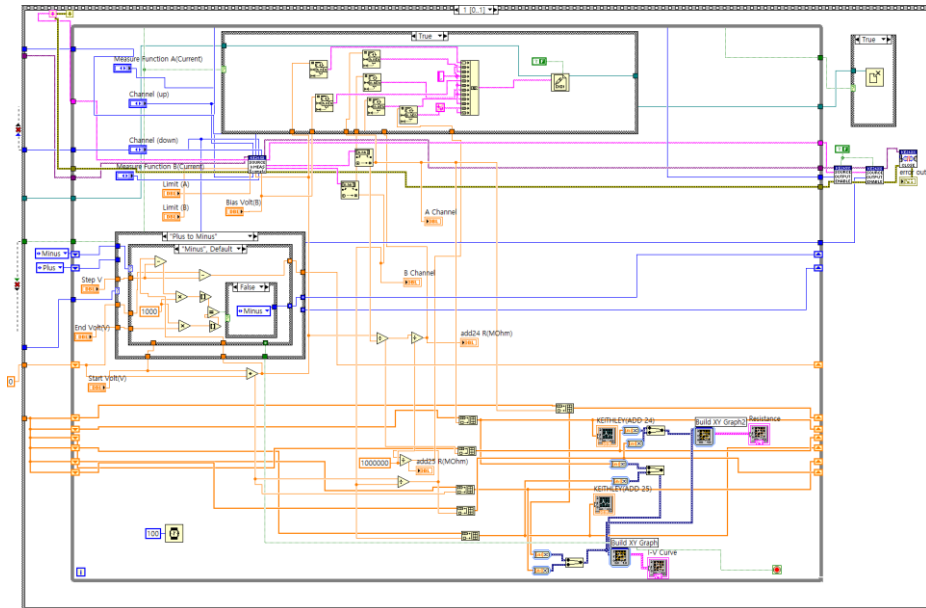
This Program is made by Youngsoo Kim.

Block Diagram

Data storage part

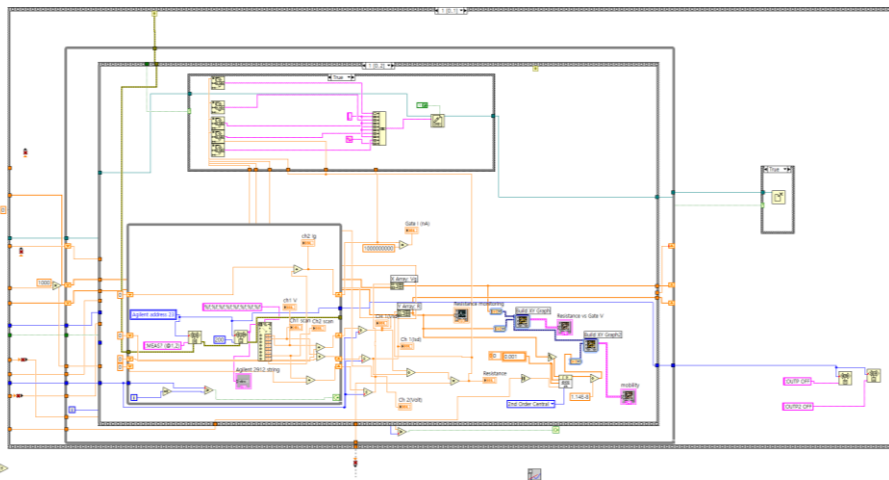
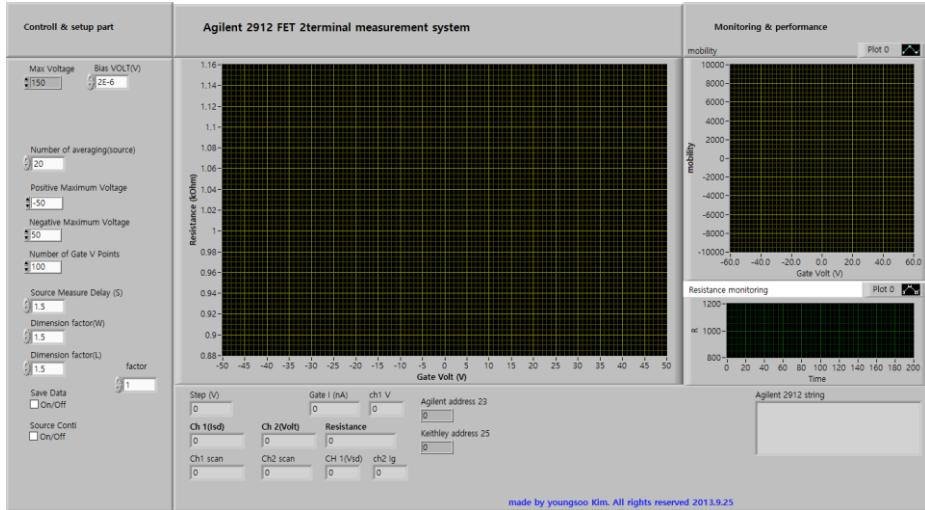


Measurement and analysis part



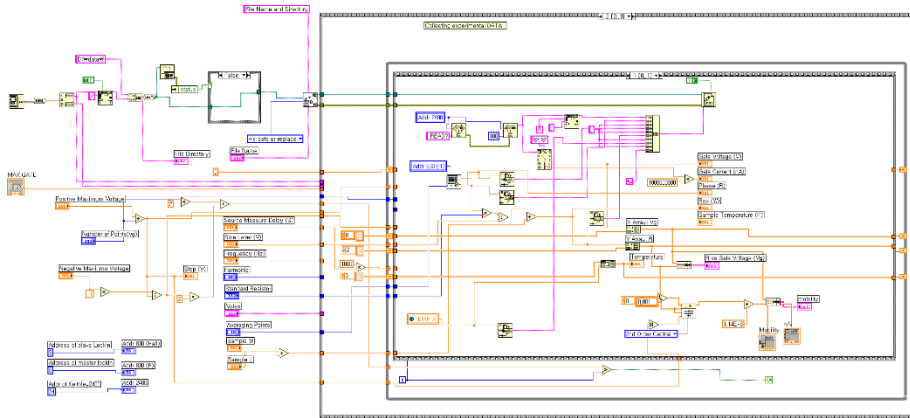
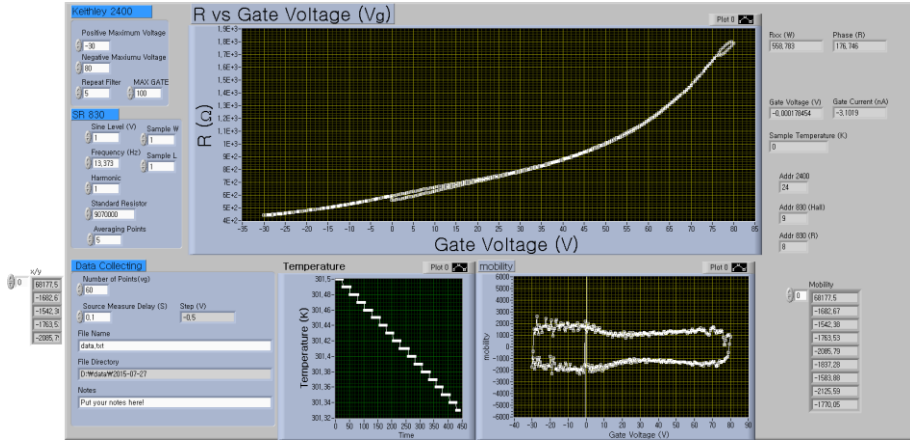
- Agilent 2912 FET 2terminal measurement system

Front Panel and block diagram



- **Lock-in Amplifier (SRS 830) with Keithley 2400 FET measurement system**

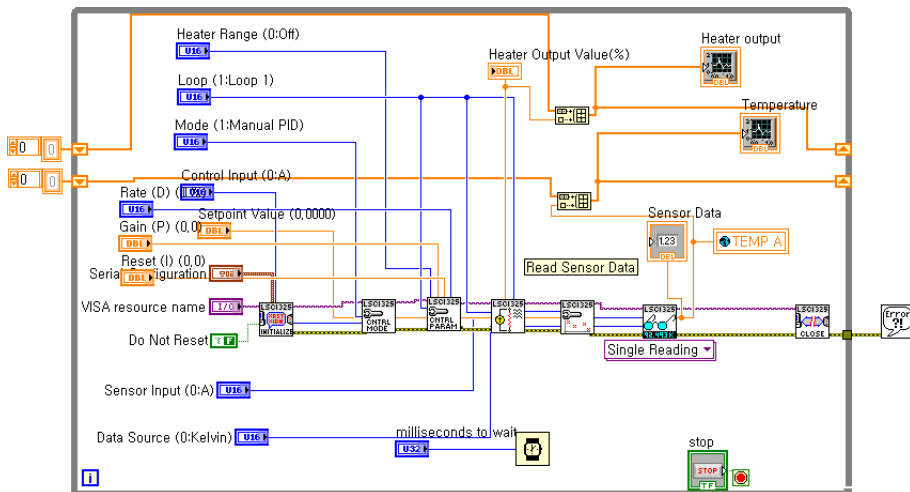
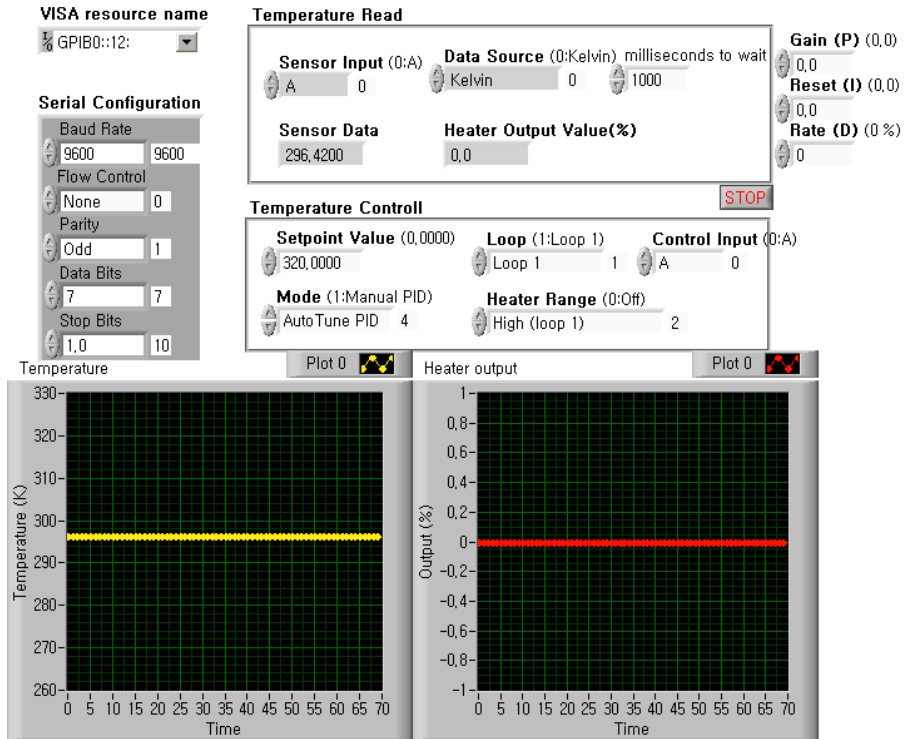
Front panel and block diagram



- Liquid Nitrogen Cryostat Temperature Control System

Front panel and block diagram

©2006 Lake Shore Cryotronics Inc. ALL RIGHTS RESERVED.



초 록

김영수

물리천문학부

서울대학교 대학원

도핑은 그래핀의 일함수와 전도도를 개질하여 그래핀의 광전소자로의 응용에 필요한 공정이며, 그 도핑 방법으로는 탄소 원자를 다른 원자로 치환하거나, 전계효과, 그리고 산이나 산화성 물질을 이용하는 화학적 도핑 방법이 있다. 이 중에서도 화학적 도핑방법은 널리 쓰이고 있으며, 방법이 간단할뿐 아니라 높은 도핑효과를 얻을 수 있다.

본 논문에서는 아미노페닐 프로파길 이터를 이용하여 그래핀을 n-도핑하는 연구를 수행하였으며, 라만분광법과 전기적 특성 측정을 통해 아민기가 그래핀에 전자를 기여하는 n-도핑 효과의 원인으로 확인하였다. 더 나아가 그래핀을 화학분자들을 기화하여 보다 효율적으로 도핑하는 방법을 고안하였고, 이를 통해 아민기의 개수에 따른 그래핀의 n 도핑효과를 확인하여 안정성을 확인하였다. 아민기의 개수가 많은 분자일수록 높은 도핑효과를 보였고, 상온에서의 안정성 또한 높았다. 또한 아민기를 가지는 자기조립단분자층과 다이에틸렌트리아민 분자를 이용하여 그래핀의 위, 아래인 양면은 n 도핑하여 매우높은 n 도핑효과를 확인하였고, 이를 이용하여 그래핀히터를 제작하여 성능향상이 향상됨을 보였다.

또한, 자기조립 단분자층을 이용하여 그래핀을 그래핀을 도핑과 동시에 품질을 높이는 효과를 관측할수 있었으며, 또한 도핑이 거의 되지 않는 메틸기를 말단으로가지는 자기조립단분자층을 이용하여 그래핀의 전하이동도를 크게 향상시킬수 있었다. 뿐만 아니라, 자기조립 단분자층 위에 있는 그래핀의 경우에는 실리콘옥사이드 위의 그래핀과 달리 특이한 저항 대 온도 경향성을 보임을 확인하였다. 또한, 전자빔 식각공정을 통하여 부분적인 그래핀의 도핑을 형성할 수 있었고, 이를 통해 그래핀 p-n 접합을 형성할 수 있었다.

그리고, 그래핀의 상업적인 접근을 위해, 수소가스 없이 빠른 그래핀 합성공정을 고안하였고, 롤투롤 식각과 전사를 통해 그래핀을 이용한 터치스크린을 제작하였고, 이 성능 또한 기존 ITO 박막을 이용한 터치스크린에 비해 우수한 특성을 가짐을 확인하였다.

마지막으로, 화학기상증착법으로 합성된 그래핀을 이용하여 그래핀의 자성을 측정하고자 했으며, 그 결과 비소에 비해 100 배가량 높은 반자성을 가짐을 확인하였고, 이것을 통해 그래핀의 전자기파 차폐효과가 기존 일반적으로 사용된 차폐막에 비해 우수한 것을 확인하였다.

주요어 : 그래핀, 화학적 도핑, 그래핀 전계효과 트랜지스터, 화학기상증착법, 그래핀 품질 개선, 그래핀 응용, 그래핀 자성
학 번: 2012-30101